A measurement of the Drell-Yan differential cross section using data from proton-proton collisions at 7 TeV with the ATLAS detector

by

Tony Kwan
B.Sc., University of Victoria, 2010

A Thesis Submitted in Partial Fulfillment of the
Requirements for the Degree of

MASTER OF SCIENCE

in the Department of Physics and Astronomy

A measurement of the Drell-Yan differential cross section using data from proton-proton collisions at 7 TeV with the ATLAS detector

by

Tony Kwan
B.Sc., University of Victoria, 2010

Supervisory Committee

Dr. Richard K. Keeler, Supervisor
(Department of Physics and Astronomy)

Dr. Robert V. Kowalewski, Departmental Member
(Department of Physics and Astronomy)

Dr. Robert A. McPherson, Departmental Member
(Department of Physics and Astronomy)

Supervisory Committee

Dr. Richard K. Keeler, Supervisor
(Department of Physics and Astronomy)

Dr. Robert V. Kowalewski, Departmental Member
(Department of Physics and Astronomy)

Dr. Robert A. McPherson, Departmental Member
(Department of Physics and Astronomy)

ABSTRACT

LHC proton-proton collisions at a centre of mass energy of $\sqrt{s} = 7$ TeV were observed in 2011. From a 1.68 fb^{-1} sample of the data collected using the ATLAS detector, electron-positron pairs originating from the Drell-Yan process were selected using a cut based analysis. After the selection process, an estimate of the background was determined followed by the selection efficiency, detector resolution, reconstruction efficiency, and kinematic acceptance. Using these, the Drell-Yan differential cross section was calculated as a function of invariant mass between 26 and 66 GeV/c^2. This measurement has a precision between 12.4% and 8.01% from the lower invariant mass bins to the higher ones. The Drell-Yan cross section in proton-proton collisions depends on empirical quantities known as parton distribution functions which parametrize the structure of the proton. The measurement outlined in this thesis observes a region in parton distribution function phase space previously untouched by experiments.

Contents

List of Tables

List of Figures

ACKNOWLEDGEMENTS

As I am writing the words you're reading now, I am less than half way done writing this thesis with about a month to go before its deadline and I need a bit of motivation. Thinking about the people who have helped me along the way and who continue to help me will provide this motivation.

I have to start by thanking Dr. Margret Fincke-Keeler for giving me my first shot in particle physics as a summer student many years ago. I would not be where I am today without her.

I did co-op as an undergrad and had the chance of being supervised by several great researchers. The one that stands out to me is Dr. Dale Ellis of the Defence Research and Development Canada. He more than anyone has inspired me to become a scientist.

I need to thank my friends in the department: Anthony Fradette, Brock Moir, Sam Dejong, and the rest of those who started with me and Alison Elliot, Stephanie LaForest, and the rest of the first year grads. If all things go according to plan, I'll have a master's degree by the end of this, but it's the baseball, the wing nights, the yoga, the curling, and our conversations over beer with you all that I will take with me. For you, I wish nothing but success, happiness, and love.

My outside-of-physics friends, brother, and parents have been greatly supportive and have tolerated my antics over the years.

Much of the work in this thesis could not have been possible without Dr. Tayfun Ince, who is one of the most passionate physicists I've met. He has guided me through just about every aspect of this analysis with logic, conciseness, and of course – passion. This analysis is his; I am merely performing a check. Tayfun will make a great supervisor one day.

Lastly, but most importantly, Dr. Richard Keeler. Richard has been wonderful to work for and with. He has provided me with the freedom to research whatever interested me, while pulling me back in when I got too far off track. Throughout my entire period of research, Richard has been understanding, patient, and nothing but supportive. The work before you would absolutely not have been possible without his guidance. Richard has this supervisor thing down to an art. Thank you, Richard.

To Mom

Chapter 1

Introduction

The forefront of particle physics research is currently at the Large Hadron Collider (LHC) [1] in Geneva, Switzerland. The LHC is a particle accelerator designed to collide protons at centre of mass energies never before reached. Protons are, however, not elementary particles and at high energies, the proton may be thought of as having a complex substructure comprised of elementary point particles called partons. The quantum field theory that describes elementary particles, such as partons, and the forces between them is called the Standard Model. To calculate interaction rates and other observables in LHC collisions using the Standard Model, one must know the distribution of partons as a function of the collision kinematics. Experimentally determined functions called parton distribution functions (PDFs) convey this information. The goal of this thesis is to calculate the differential cross section of the Drell-Yan process which can be used to constrain and ultimately improve PDFs.

1.1 The LHC and the ATLAS Experiment

Located near the French-Swiss border is the LHC, a circular particle accelerator designed to collide protons with other protons at energy levels higher than any accelerator before it. Housed at the European Organization for Nuclear Research (CERN), the LHC is approximately 26.7 km in circumference. At full capacity, the LHC will collide two proton beams at a centre of mass energy of 14 TeV at a luminosity, the number of particles per unit area per unit time crossing at the point of interaction, of 10^{34} $\text{cm}^{-2}\text{s}^{-1}$. Putting this into perspective, Fermilab's Tevatron, also a proton-antiproton collider, reached a centre of mass energy of approximately 2 TeV with a

luminosity of 10^{32} $cm^{-2}s^{-1}$. With higher energy collisions, there is greater opportunity to see new physical phenomena and gain more understanding.

Numerous experiments are being conducted using the LHC whose layout can be seen in Figure 1.1; one of which is the A Toroidal LHC ApparatuS (ATLAS) experiment [2]. The ATLAS collaboration has constructed a state of the art general-purpose detector called the ATLAS detector, located at one of the collision points of the LHC. The ATLAS detector is cylindrical in shape, with a diameter of 25 m and a length of 44 m. A diagram of the ATLAS detector can be seen in Figure 1.2.

The LHC and ATLAS detector were designed with several physics goals in mind. These goals include searching for the Higgs boson and potential new physics beyond the Standard Model, and making precision measurements of Standard Model parameters [3]. The ATLAS detector was designed to be sensitive over the possible mass range of the Higgs boson, maximizing the potential for its discovery[1]. The Standard Model is not a complete theory of particle physics. Theories that extend the Standard Model such as Supersymmetry have been proposed to explain phenomena that the Standard Model fails to, such as the existence of dark matter. With the LHC and ATLAS detector, it will be possible to discover supersymmetric particles or exclude them over a large portion of their theoretically possible masses. The LHC running at its full capability will have the highest centre of mass energy and luminosity of any particle accelerator. Because of this, the ATLAS experiment will be able to re-measure some Standard Model parameters to higher precision. Such measurements include the top quark mass, the coupling parameters between fermions and gauge bosons, and the substructure of protons.

1.2 A Measurement of the Drell-Yan Differential Cross Section

Protons are not fundamental particles, but are composed of partons, a name given to any one of the quarks, antiquarks, and gluons found in a hadron. At sufficiently high momentum transfer, the collision between two protons can be seen as the collision of two groups of partons. To perform precise calculations of measurements in ATLAS, functions that give the probability of finding a pair of partons carrying certain frac-

[1] On July 4th, 2012, ATLAS and CMS announced to the public that a Higgs boson candidate has been observed.

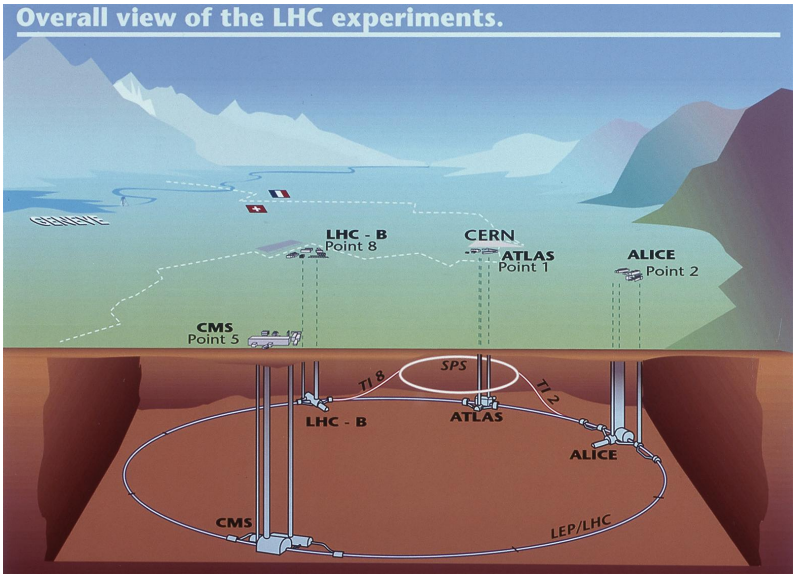

Figure 1.1: The layout of the LHC. This diagram shows the locations of the four main experiments (ALICE, ATLAS, CMS and LHCb) that are being conducted at the LHC. Located between 50 m and 150 m underground, huge caverns have been excavated to house giant detectors like the ATLAS detector.

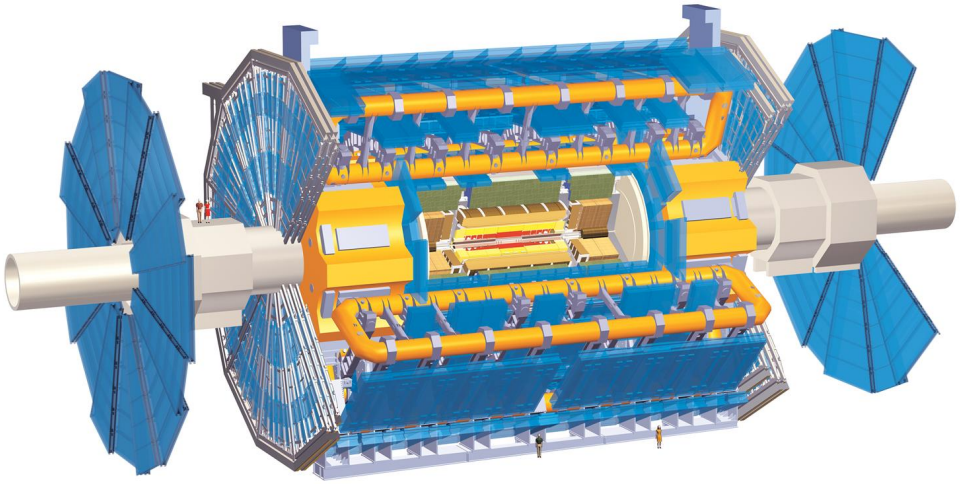

Figure 1.2: The ATLAS detector. The size of the ATLAS detector is put into perspective when noting the people in this diagram.

tions of the protons' momenta and interacting at a given momentum transfer must in practice be determined empirically using data from particle physics experiments. This information is contained in parton distribution functions. As the LHC will accelerate proton beams to energies never reached before, values of parton momentum fractions and momentum transfers will be reached for the first time. A plot showing the regions in PDF parameter space that the ATLAS, HERA, and LHCb experiments can probe; the black border represents the parameter space that this analysis can potentially examine. The measurement described in this thesis will allow the improvement of PDFs in this new phase space and ultimately improve all measurements made at the LHC.

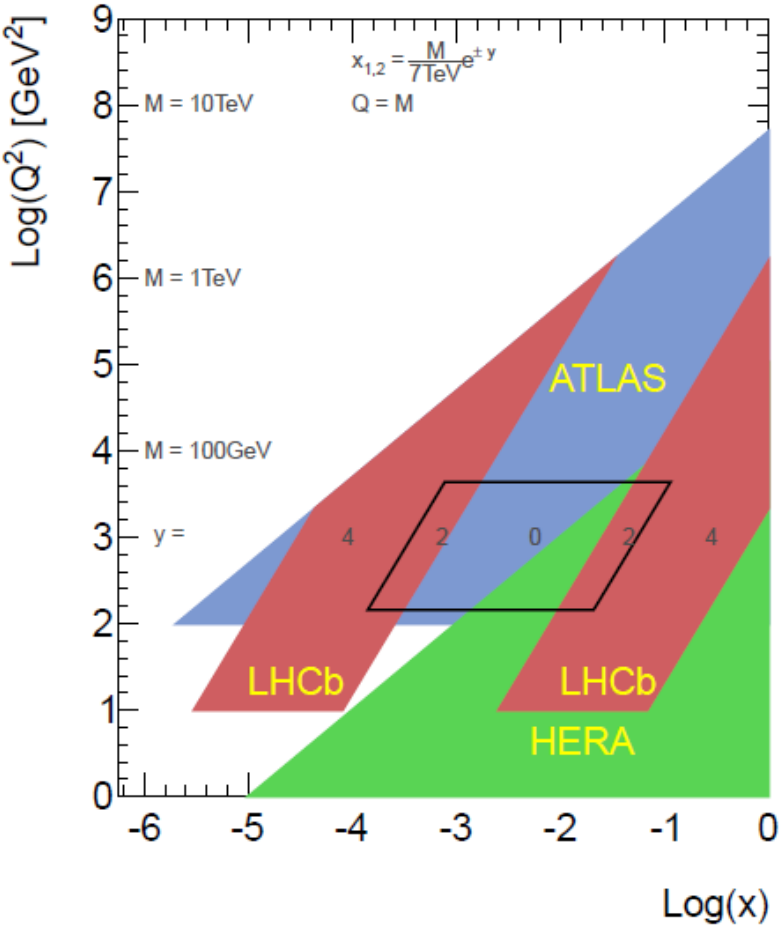

Figure 1.3: The region in parton distribution function parameter space the ATLAS experiment (along with several other experiments) will be able to probe. The black border represents the region the analysis outlined in this thesis probes.

The work outlined in this thesis is a measurement made using 2011 data from proton-proton collisions at a centre of mass energy of 7 TeV produced by the LHC and collected with the ATLAS detector. More specifically, a differential cross section, the likelihood of observing a particular physical process as a function of some physical quantity, of the Drell-Yan process will be measured. The Drell-Yan process, first predicted by Sidney D. Drell and Tung-Mow Yan in 1970 [4], involves a quark and an antiquark annihilating to produce a virtual photon or a Z boson which then proceeds to decay into a lepton-antilepton pair. This analysis focuses only on the case in which the lepton is an electron and the antilepton is a positron [5]. The Drell-Yan process has played an important role in particle physics over the last decade, including the discoveries of the J/ψ and Υ particles, and the Z boson.

The goal is to measure the Drell-Yan differential cross section as a function of invariant mass for the process $q\bar{q} \rightarrow Z/\gamma^* \rightarrow e^+e^-$ in the ATLAS detector. The advantage of this process is that the two-lepton final state is readily measurable in ATLAS. The signatures left behind by electrons or positrons in the ATLAS detector are well understood, even in the complex realm of proton-proton collisions.

1.2.1 Thesis Outline

This thesis is divided into chapters as follows. Chapter 1 introduces the LHC and the ATLAS experiment, briefly describes the physical process central to the analysis, and states the importance of this measurement. The cross section, the Standard Model of particle physics, parton distribution functions, and the Parton Model and QCD will be presented in Chapter 2. In Chapter 3, information on the LHC and the ATLAS detector will be presented. Chapter 4 describes the structure of ATLAS data, states the data set used in this analysis, describes Monte Carlo production, and states the Monte Carlo samples used in this analysis; it also develops the techniques of electron reconstruction and identification and concludes with event selection. Chapter 5 outlines the analysis approach; it describes the quantities required and mathematically develops the equation needed to calculate the Drell-Yan differential cross section.

The following chapters describe the experimental techniques used to find the quantities needed for the calculation of the Drell-Yan differential cross section. Chapter 6 presents the measured distribution and a Drell-Yan background estimation. The selection efficiency, detector resolution, reconstruction efficiency, and acceptance are determined in Chapter 7. In Chapter 8, systematic uncertainties associated with some

of the techniques used in this analysis are assessed. The Drell-Yan differential cross section is computed and discussed in Chapter 9. Chapter 10 concludes this thesis with a few statements on the results.

Chapter 2

Theory

This chapter begins with a conceptual description of a quantity known as the cross section. In order to calculate cross sections of processes resulting from hadron-hadron collisions, parton distribution functions and the QCD Parton Model must be used. This chapter develops the theory necessary for such calculations. Finally, the Drell-Yan process is presented in the context of electromagnetic and weak processes and the QCD Parton Model is then applied to it.

2.1 The Cross Section

Scattering experiments probe the behaviour of elementary particles by colliding two particles beams with well-defined momenta and then observing what comes out. The probability of observing a particular final state can be expressed in terms of a quantity known as the cross section [6]. Every physical process has a cross section associated to it.

Consider two bunches of particles, bunch A with particles per unit volume ρ_A and bunch B with density ρ_B. Suppose it is arranged such that the beams are directed towards each other. This could be head on or a beam on a fixed target. Let L_A and L_B be the lengths of the bunches. It is expected that the number N of scattering events (of the desired type) is proportional to ρ_A, ρ_B, L_A, L_B, and the cross-sectional area A common to the two bunches of particles. The cross section σ is simply the total number N of selected events divided by these quantities:

$$\sigma = \frac{N}{\rho_A L_A \rho_B L_B A}. \tag{2.1}$$

The cross section has units of area; it can be interpreted as the effective area of a portion taken out of one beam by each of the particles in the other beam that subsequently interact and become the final state of interest.

An accelerator produces particle collisions between two sets of particles, known as bunches, with a flux $\mathcal{L}$ known as the instantaneous luminosity. The instantaneous luminosity is defined using machine parameters as

$$\mathcal{L} = \frac{f_r n_b n_1 n_2}{2\pi\sqrt{(\sigma_{1x}^2 + \sigma_{2x}^2)(\sigma_{1y}^2 + \sigma_{2y}^2)}}, \tag{2.2}$$

where f_r is the frequency of revolution of the bunches and n_b is the number of bunch pairs colliding per revolution; n_1 and n_2 are the number of particles found in each of the bunches for beam 1 and beam 2, respectively. The quantities σ_x and σ_y are the beam dimensions. The instantaneous luminosity can be interpreted as the number of intersections of particles per unit area per unit time.

The integrated luminosity $\int dt\, \mathcal{L}(t)$ represents the number of intersections per unit area for some running time t of the accelerator. By multiplying the integrated luminosity by the cross section, the number of events of the desired type is obtained. The number of events, given some integrated luminosity $\int dt\, \mathcal{L}(t)$, is

$$N = \sigma \int dt\, \mathcal{L}(t). \tag{2.3}$$

This simple expression is fundamental to particle physics. It states that the number of occurrences of some process is linearly proportional to the integrated luminosity, a quantity that is readily accessible, and the proportionality constant is the cross section of that process.

2.2 The Standard Model

Developed over the last century, the Standard Model [7] is a theory that describes the dynamics of elementary particles as they undergo electromagnetic, weak, and strong interactions. The Standard Model includes twelve elementary particles of half-integer spin known as fermions, along with their corresponding antiparticles, and four types of force carrying particles of integer spin called gauge bosons. The interactions between fermions are mediated by the gauge bosons thus providing a nearly complete description of Nature. However, there remains a particle crucial to

the Standard Model that has yet to be discovered – the Higgs boson. A candidate narrow resonance has been recently observed, but it remains to be shown to be the Standard Model Higgs boson.

The twelve fermions are are broken into two categories, leptons and quarks. The leptons are electrons, muons, taus, electron neutrinos, muon neutrinos, and tau neutrinos. All leptons interact via the weak force and those that are electrically charged, namely electrons, muons, and taus, also interact via the electromagnetic force. The quarks are up, down, charm, strange, top, and bottom. Quarks may interact weakly and since they are electrically charged, they may also interact electromagnetically. Quarks also carry colour charge which permits them to interact via the strong force. The fermions are further categorized into three generations based on mass. A chart depicting this can be seen in Figure 2.1. The first generation of elementary particles constitutes ordinary matter. Atoms are made of electrons, protons (composed of two up and one down valence quarks) and neutrons (composed of one up and two down valence quarks).

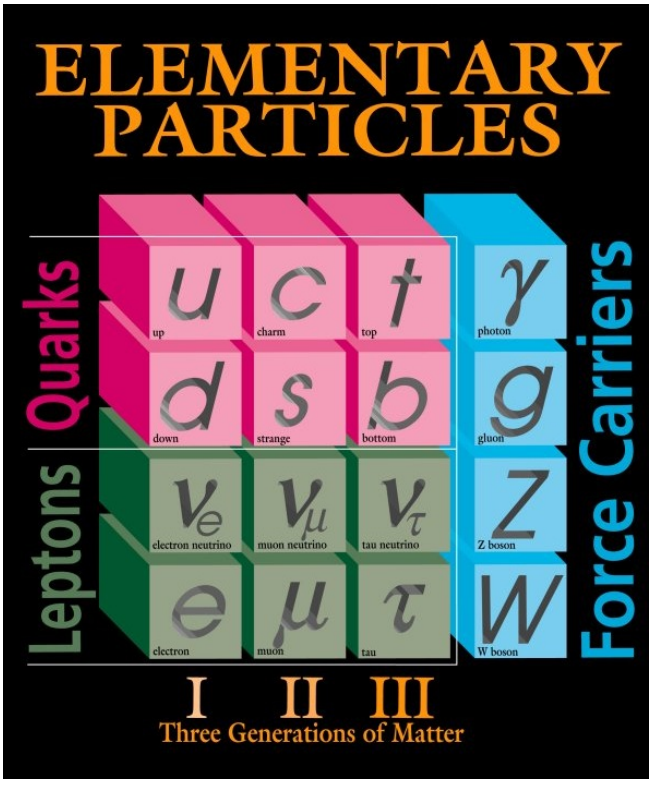

Figure 2.1: The fundamental particles of the Standard Model of particle physics (Fermilab Visual Media Services).

The photon is one of the Standard Model gauge bosons. It is a massless particle responsible for mediating the electromagnetic force between electrically charged fermions. A Feynman diagram showing the interaction of an electrically charged fermion (such as an electron) with a photon can be seen in Figure 2.2. All electromagnetic phenomena are ultimately reducible to this process. The strength of this interaction is characterized by the electromagnetic coupling constant[1] $\alpha = 1/137$. The relativistic quantum field theory that describes the interactions between fermions with electric charge and photons is known as quantum electrodynamics (QED).

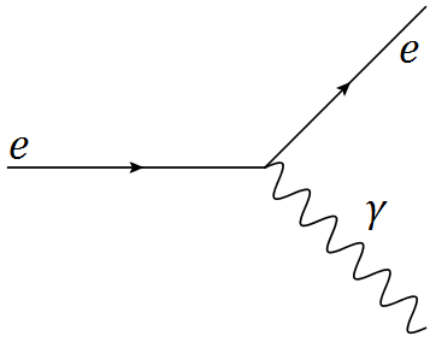

Figure 2.2: A vertex showing the interaction of a fermion with a photon. In this Feynman diagram, the arrow of time points from left to right.

The gluon is the massless gauge boson responsible for mediating the strong force between particles with colour charges. The strong force is aptly named because it is the strongest of the fundamental forces of nature. The relativistic quantum field theory that describes the interactions between these fermions and gluons is known as quantum chromodynamics (QCD). A Feynman diagram showing the fundamental vertex, the interaction of a fermion with colour charge (a quark) with a gluon, can be seen in Figure 2.3. In QED, a single number is required to characterize the electric charge of a particle; however, in QCD, there are three possible colour charges: red, green, and blue. Like electric charge, colour must always be conserved at each vertex, meaning the gluon must carry away any difference in colour between the incoming and outgoing quarks. As an example, suppose this diagram depicts the process $q \rightarrow q + g$, where the original quark has one unit of blueness and the resultant quark has a unit of redness. The gluon must then carry one unit of blueness and minus one unit of redness in order to satisfy conservation of colour.

[1]The electromagnetic coupling constant is in fact a function of the momentum transfer between the interacting particles. At low energies, $\alpha = 1/137$ is a good estimate.

The strong force coupling constant α_s depends on the separation distance between the interacting particles or equivalently momentum transfer Q^2 and because of this dependence, the strong force coupling constant is said to be running. At large distances or low momentum transfers, α_s is very large thus forcing these particles together. This phenomenon is known as confinement and it is the reason why free quarks do not exist. Conversely, at small distances or high momentum transfer, α_s is sufficiently small such that the particles can be treated as free. This feature is known as asymptotic freedom.

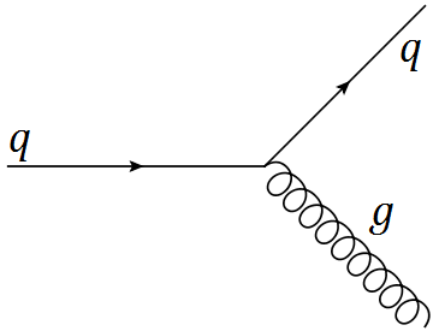

Figure 2.3: A vertex showing the interaction of a quark with a gluon.

Finally, the $W^{\pm}$ and Z bosons are responsible for mediating the weak force. Unlike the photon and the gluon, the $W^{\pm}$ and Z bosons are massive, thus making the weak force short in range and much weaker at large distances compared to the electromagnetic and strong forces. A Feynman diagram of the weak interaction vertex can be seen in Figure 2.4 which shows a lepton decaying into a W boson and a neutrino. A weak interaction mediated by a W does not conserve quark flavour. In other words, it is permissible for a quark interacting with a W boson to change its flavour. For example, suppose a top quark interacts with a W^+ boson. The outgoing quark could either be a bottom quark, strange, or down quark.

The Standard Model is a gauge invariant theory, meaning its Lagrangian must be invariant under a continuous group of local transformations. In order for the Standard Model to be indeed a gauge invariant theory, the gauge bosons must in principle be massless. This is true for the massless photon and gluon, but untrue for the massive $W^{\pm}$ and Z weak bosons. However, through a process called the Higgs Mechanism, the $W^{\pm}$ and Z bosons acquire masses and the Standard Model Lagrangian is left invariant under gauge transformations, but at the expense of the introduction of a new particle called the Higgs boson. Through interaction with the Higgs boson, the

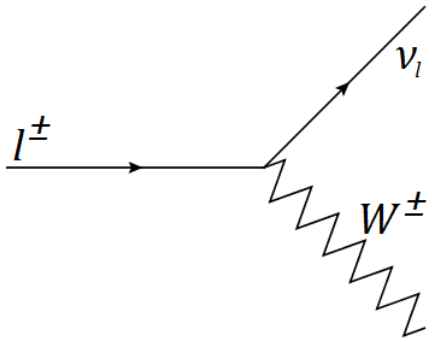

Figure 2.4: A vertex showing the interaction of a fermion with a W/Z.

particles of the Standard Model essentially gain mass.

The predictions of the Standard Model have been thoroughly tested to marvellous precision by numerous experiments over the past several decades. Despite its triumphs, the Standard Model does have its shortcomings. It does not incorporate the physics of dark matter and energy or the full theory of gravitation as described by general relativity. The Standard Model is by no means a complete theoretical framework. There remains much work to be done in verifying the remaining unobserved predictions of the Standard Model and models that predict physics beyond the scope of the Standard Model.

2.3 Parton Distribution Functions

Information about the structure of the proton and other hadrons is contained in empirical functions known as parton distribution functions (PDFs). A parton distribution function $f_a(x_a)$ gives the probability of finding in some hadron a parton of flavour a, carrying fraction x_a of the total momentum of the hadron at a fixed momentum transfer Q^2 for some hard interaction.

Shown in Figure 2.5 [8] are the PDFs for several partons including the up, down, antiup, antidown, and gluon of a proton. It can be seen that, as expected, the up and down quarks are most likely to carry a substantial fraction x of the momentum of the proton while the other flavours tend to carry a smaller fraction of the total momentum.

Parton distribution functions are the probability of finding particular constituents of the proton, so then they must be normalized in such a way that reflects the pro-

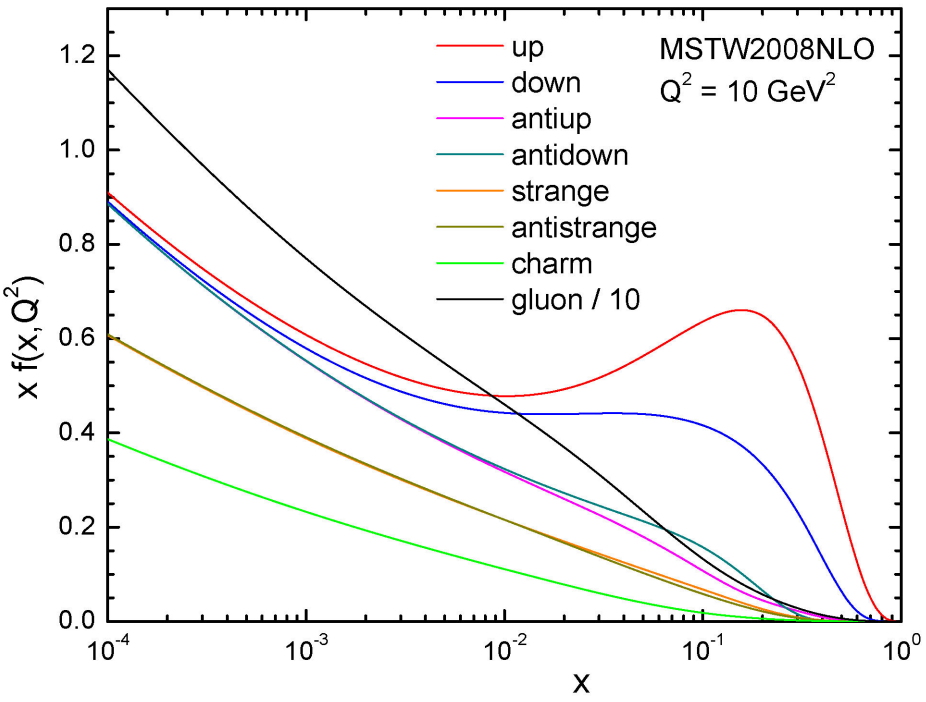

Figure 2.5: The parton distribution functions for several partons of the proton.

ton's quantum numbers. The proton is a bound state of uud (up-up-down) plus some admixture of quark-antiquark pairs. As a result, the PDFs should reflect an excess of two u and one d over their corresponding antiquarks. Mathematically, these constraints are

$$\int_0^1 dx[f_u(x) - f_{\bar{u}}(x)] = 2, \quad \int_0^1 dx[f_d(x) - f_{\bar{d}}(x)] = 1, \tag{2.4}$$

where f_q is the PDF for quark q of the proton. As mentioned, there exist PDFs for all other hadrons, each having similar constraints as those seen above in Equation (2.4). Parton distribution functions should also reflect the symmetries between different types of hadrons. For example, a proton is a bound state of uud and the neutron is a bound state of udd. By interchanging the role of the up and down quarks in a proton, a neutron is generated. Therefore, the neutron's PDFs must obey the following constraints:

$$f_u^n(x) = f_d(x), \quad f_d^n(x) = f_u(x), \quad f_{\bar{u}}^n(x) = f_{\bar{d}}(x), \quad f_{\bar{d}}^n(x) = f_{\bar{u}}(x), \quad \text{etc.}, \tag{2.5}$$

where $f^n(x)$ denotes the PDF of the neutron. Similar PDFs exist for antihadrons; take the antiproton for example:

$$f_u^{\bar{p}}(x) = f_{\bar{u}}(x), \quad f_{\bar{u}}^{\bar{p}} = f_u(x), \quad \text{etc.} \tag{2.6}$$

The total amount of momentum carried by the partons must equal the total momentum of the hadron:

$$\int_0^1 dx\, x[f_u(x) + f_d(x) + f_s(x) + f_{\bar{u}}(x) + f_{\bar{d}}(x) + f_{\bar{s}}(x) + f_g(x) + ...] = 1. \tag{2.7}$$

These are a few of the mathematical properties of parton distribution functions; there are of course others. The mathematical roles PDFs play in phenomenology will be illustrated in the following section.

2.4 The Parton Model

The Parton Model describes high energy collisions of sufficiently large momentum transfers Q^2 between a hadron with any type of particle by treating its partons as independent particles. A large momentum transfer Q^2 is equivalent to a short interaction time-scale and thus the partons appear to be a collection of free particles. This is the central assumption the Parton Model makes [9].

The Parton Model yields a mechanism for calculating cross sections for hadron-hadron collisions. As each parton is considered a quasi-free particle, the cross section is taken as a sum of the cross sections of subprocesses involving the partons in one hadron and those in the other hadron. In the Parton Model, the structure of the hadron is contained within the PDFs. To illustrate these points, consider the collision between a proton A with another proton B for some fixed Q^2 that is large enough such that the Parton Model applies. Denote the longitudinal momentum fraction of parton a in A by x_a and the PDF of a in A to be $f_{a/A}(x_a)$. Similarly, for proton B there is b, x_b, and $f_{b/B}(x_b)$. Suppose these protons collide and undergo the following reaction:

$$A + B \to c + X, \tag{2.8}$$

where c is a fermion and X represents any final state particle or particles. Suppose internally there is the subprocess

$$a + b \to c + X. \tag{2.9}$$

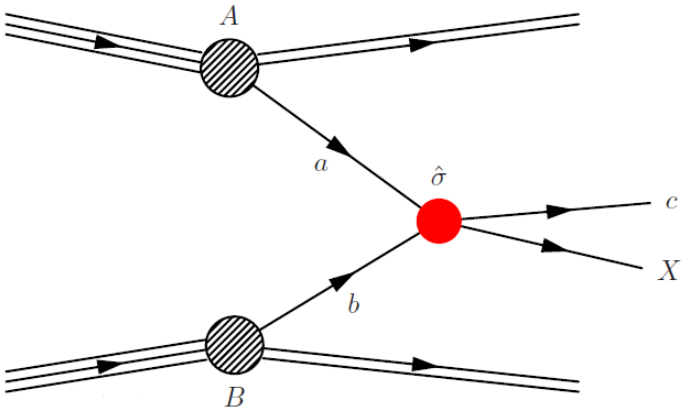

Figure 2.6: A parton-parton collision in which parton a of hadron A and b of B interact with cross section $\hat{\sigma}$ to produce fermion c and any final state particle or particles X.

This process is illustrated in Figure 2.6 [5]. The cross section $\sigma \equiv \sigma(AB \to cX)$ is calculated by multiplying the subprocess cross section $\hat{\sigma} \equiv \hat{\sigma}(ab \to cX)$ by $dx_a f_{a/A}(x_a)$ and $dx_b f_{b/B}(x_b)$, summing over all parton types of a and b, and integrating over x_a and x_b. Finally, taking the average over the possible colours of a and b, σ is obtained. Symbolically, this is [10]

$$\sigma = \sum_{a,b} C_{ab} \int dx_a dx_b [f_{a/A}(x_a) f_{b/B}(x_b) + (A \leftrightarrow B \text{ if } a \neq b)]\hat{\sigma}, \tag{2.10}$$

where the sum is taken over all possible initial and final colour states of a and b. The initial colour-average factor C_{ab} that appears in the equation above can take the following possible values:

$$C_{qq} = C_{q\bar{q}} = \frac{1}{9}, \quad C_{qg} = \frac{1}{24}, \quad C_{gg} = \frac{1}{64}, \tag{2.11}$$

given that a quark q has three possible colour charges and a gluon g has eight. The term

$$A \leftrightarrow B \equiv f_{a/B}(x_b) f_{b/A}(x_a), \tag{2.12}$$

is introduced to account for the possibility of parton a coming from proton B and parton b coming from parton A. In the case $a = b$, this term is zero.

In some Lorentz frame in which the masses of A and B can be neglected compared to their three-momenta, their four-momenta can be written as

$$p_a = x_a P_A, \quad p_b = x_b P_B, \tag{2.13}$$

where $p_{a,b}$ is the four-momentum of the parton and $P_{A,B}$ is the four momentum of the proton. This leads to

$$\hat{s} = (p_a + p_b)^2 = x_a x_b s, \tag{2.14}$$

where $\sqrt{\hat{s}}$ is the centre of mass energy of the parton pair and $\sqrt{s}$ is the centre of mass energy of the proton pair. Defining $\tau = x_a x_b$ (a number between 0 and 1), Equation (2.14) becomes

$$\hat{s} = x_a x_b s = \tau s. \tag{2.15}$$

Writing Equation (2.10) in terms of x_a and τ gives

$$\sigma = \sum_{a,b} C_{ab} \int_0^1 d\tau \int_\tau^1 \frac{dx_a}{x_a} \left[f_{a/A}(x_a) f_{b/B}\left(\frac{\tau}{x_a}\right) + (A \leftrightarrow B \text{ if } a \neq b) \right] \hat{\sigma}. \tag{2.16}$$

By taking the derivative of Equation (2.16) with respect to τ, the differential cross section with respect to τ for the process $A + B \to c + X$ is obtained:

$$\begin{aligned} \frac{d\sigma}{d\tau} &= \sum_{a,b} C_{ab} \int_\tau^1 \frac{dx_a}{x_a} \left[f_{a/A}(x_a) f_{b/B}\left(\frac{\tau}{x_a}\right) + (A \leftrightarrow B \text{ if } a \neq b) \right] \hat{\sigma}(\hat{s} = \tau s) \\ &= \sum_{a,b} \frac{d\mathcal{L}_{ab}}{d\tau} \hat{\sigma}(\hat{s} = \tau s), \end{aligned} \tag{2.17}$$

where the parton luminosity is defined as

$$\frac{d\mathcal{L}_{ab}}{d\tau} = C_{ab} \int_{\tau}^{1} \frac{dx_a}{x_a} \left[f_{a/A}(x_a) f_{b/B} \left(\frac{\tau}{x_a} \right) + (A \leftrightarrow B \text{ if } a \neq b) \right]. \tag{2.18}$$

It is convenient to express observables in terms of a quantity known as rapidity y, defined as

$$y = \frac{1}{2} \ln \left(\frac{E^{CM} + p_L^{CM}}{E^{CM} - p_L^{CM}} \right) = \frac{1}{2} \ln \left(\frac{x_a}{x_b} \right), \tag{2.19}$$

where $E^{CM} = \sqrt{\hat{s}}$ is the energy and p_L^{CM} is the magnitude of the longitudinal momentum of the ab system in the AB centre of mass frame. Rapidity is invariant under Lorentz boosts save for the addition of a constant term. This property leads to differences in rapidity being Lorentz invariant under boosts.

Having defined rapidity, it is useful to define a quantity known as pseudorapidity. Note that for massless particles, $E^{CM} = |\vec{p}|$ and so the rapidity for a massless particle is

$$y = \frac{1}{2} \ln \left(\frac{|\vec{p}| + p_L^{CM}}{|\vec{p}| - p_L^{CM}} \right), \tag{2.20}$$

and substituting $p_L^{CM} = |\vec{p} \cos\theta|$, where θ is the polar angle of this massless particle from the beam, yields

$$y = \frac{1}{2} \ln \left(\frac{1 + \cos\theta}{1 - \cos\theta} \right) = -\ln \left(\tan \frac{\theta}{2} \right) \equiv \eta. \tag{2.21}$$

Pseudorapidity η is defined for both massive and massless particles by Equation (2.21) and only for massless particles does $y = \eta$. Pseudorapidity is often used as a coordinate variable for particles instead of θ.

Using Equation (2.19) and the definition $\tau = x_a x_b$, a relation between x_a, x_b and y, τ is formed:

$$x_{a,b} = \sqrt{\tau} e^{\pm y}, \tag{2.22}$$

where x_a is related to the positive exponent and x_b the negative. Taking the derivative of Equation (2.17) with respect to y yields

$$\frac{d^2\sigma}{dyd\tau} = \frac{d^2\sigma}{dx_a dx_b} = \sum_{a,b} C_{ab} \left[f_{a/A}(x_a) f_{b/B} \left(\frac{\tau}{x_a} \right) + (A \leftrightarrow B \text{ if } a \neq b) \right] \hat{\sigma}. \qquad (2.23)$$

This double differential cross section $d^2\sigma/dx_a dx_b$ is important because it relates directly to momentum fractions x_a and x_b.

2.5 The QCD Parton Model

The Parton Model provides a mechanism for calculating cross sections of hard scattering hadrons at fixed momentum transfer Q^2. The requirement that Q^2 be fixed restricts the Parton Model to processes that do not include the possibility of gluons being emitted or exchanged by the interacting partons. The QCD Parton Model, however, does consider possible gluon interactions. Depending on the momentum transfer between the interacting parton and the gluon, different techniques are used to determine their contributions to the cross section. The contributions from low momentum transfers are absorbed into the description of the incoming hadrons, namely their PDFs. High momentum contributions are calculated perturbatively using QCD and such calculations are valid because of asymptotic freedom. The separation of these two contributions is known as factorization.

To include the possibility of gluon emission or exchange in hadron-hadron interactions, two changes must be made to the cross section given by Equation (2.10). The parton distribution functions must be modified such that they evolve with Q^2. This change accounts for the possibility of low momentum gluon emissions. Higher order terms corresponding to all possible Feynman diagrams must be added using perturbation theory thus accounting for high momentum gluon interactions.

Singularities are introduced to the Parton Model cross section equations when allowing the emission of low energy gluons from the interacting parton. A low momentum transfer has an α_s that is very large, rendering QCD calculations divergent. Instead, low momentum gluon emission is incorporated into the Parton Model by modifying the parton distribution functions using the Dokshitzer-Gribov-Lipatov-Parisi (DGLAP) equation [11]

$$t\frac{\partial}{\partial t}\begin{pmatrix} q_i(x,t) \\ g(x,t) \end{pmatrix} = \frac{\alpha_s(t)}{2\pi}\sum_{q_j,\bar{q}_j}\int_x^1 \frac{d\xi}{\xi} \times \begin{pmatrix} P_{q_iq_j}\left(\frac{x}{\xi},\alpha_s(t)\right) & P_{q_ig}\left(\frac{x}{\xi},\alpha_s(t)\right) \\ P_{gq_j}\left(\frac{x}{\xi},\alpha_s(t)\right) & P_{gg}\left(\frac{x}{\xi},\alpha_s(t)\right) \end{pmatrix} \begin{pmatrix} q_j(\xi,t) \\ g(\xi,t) \end{pmatrix}. \tag{2.24}$$

The DGLAP equation is a matrix equation in the space of quarks, antiquarks, and gluons. Here, $t = \mu^2$ where μ is known as the factorization scale. The factorization scale is an arbitrary parameter which can be thought of as a scale that separates low and high momentum transfer physics. The factorization scale is often chosen to be of the same order as the hard scattering scale Q, which characterizes the parton-parton interaction. The functions $q_i(x,t)$ and $g(x,t)$ are the parton distribution functions for the quark and gluon respectively. The splitting function or evolution kernel $P(z,\alpha_s)$ can be computed as a power series in α_s:

$$P_{q_iq_j}(z,\alpha_s) = \delta_{ij}P_{qq}^{(0)}(z) + \frac{\alpha_s(t)}{2\pi}P_{q_iq_j}^{(1)}(z) + ... \tag{2.25}$$

$$P_{qg}(z,\alpha_s) = P_{qg}^{(0)}(z) + \frac{\alpha_s(t)}{2\pi}P_{qg}^{(1)}(z) + ... \tag{2.26}$$

$$P_{gq}(z,\alpha_s) = P_{gq}^{(0)}(z) + \frac{\alpha_s(t)}{2\pi}P_{gq}^{(1)}(z) + ... \tag{2.27}$$

$$P_{gg}(z,\alpha_s) = P_{gg}^{(0)}(z) + \frac{\alpha_s(t)}{2\pi}P_{gg}^{(1)}(z) + ..., \tag{2.28}$$

where δ_{ij} is the Kronecker delta function. To lowest order, the splitting functions are

$$P_{qq}^{(0)} = C_F\left[\frac{1+x^2}{(1-x)_+ + \frac{3}{2}\delta(1-x)}\right] \tag{2.29}$$

$$P_{qg}^{(0)} = T_R[x^2 + (1-x)^2] \tag{2.30}$$

$$P_{gq}^{(0)} = C_F\left[\frac{1+(1-x)^2}{x}\right] \tag{2.31}$$

$$P_{gg}^{(0)} = 2C_A\left[\frac{x}{(1-x)_+} + \frac{1-x}{x} + x(1-x) + \delta(1-x)\frac{11C_A - 4N_cT_R}{6}\right], \tag{2.32}$$

where $\delta(1-x)$ is the Dirac delta function, $N_c = 3$ is the number of colour charges and $C_A = 3$, $T_R = 1/2$, $C_F = (N_c^2 - 1)/2N_c$. The plus sign subscripts seen in the

equations above denote

$$\frac{1}{(1-x)_+} \equiv \frac{1}{1-x}, \quad \text{for } 0 \leq x < 1 \tag{2.33}$$

$$\int_0^1 dx \frac{f(x)}{(1-x)_+} \equiv \int_0^1 dx \left(\frac{f(x) - f(1)}{1-x} \right). \tag{2.34}$$

Corrections to the Parton Model cross section accounting for high momentum gluon emissions are made using perturbative techniques from QCD. Equation (2.10) then becomes a power series in α_s:

$$\begin{aligned} \sigma = & \sum_{a,b} C_{ab} \int dx_a dx_b [f_{a/A}(x_a) f_{b/B}(x_b) + (A \leftrightarrow B \text{ if } a \neq b)] \\ & \times \left[\hat{\sigma}_0 + \frac{\alpha_s(Q^2)}{2\pi} \hat{\sigma}_1 + \left(\frac{\alpha_s(Q^2)}{2\pi} \right)^2 \hat{\sigma}_2 + ... \right], \end{aligned} \tag{2.35}$$

where the power of α_s is equal to the number of gluons being emitted in the Feynman diagram.

2.6 The Drell-Yan Process

To lowest order, the Drell-Yan process is the annihilation of a quark-antiquark pair $q\bar{q}$ producing either a virtual photon γ^* or Z boson which then decays into a lepton-antilepton $l\bar{l}$ pair. Figure 2.7 shows the Feynman diagram corresponding to this lowest order process. Consider for the moment that the quark and antiquark are free particles as opposed constituents of hadrons. The cross section for this process $q\bar{q} \to \gamma^* \to l\bar{l}$ is

$$\hat{\sigma} = N_c C_{q\bar{q}} \frac{4\pi e_q^2 \alpha^2}{3\hat{s}}. \tag{2.36}$$

The constant $N_C = 3$ is the number of colour states quarks can take and $C_{q\bar{q}} = 1/9$ is the initial colour averaging factor for a process involving $q\bar{q}$. The quantity $\alpha \equiv \alpha(Q^2 = m_{ll}^2)$ is the running electromagnetic coupling constant[2] given by

[2]The momentum transfer Q^2 is set to the invariant mass squared m_{ll}^2 of the lepton-antilepton pair.

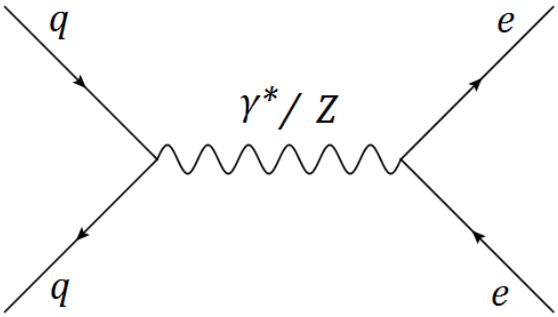

Figure 2.7: The Drell-Yan process to lowest order. A quark and an antiquark annihilate to produce a virtual photon or Z boson which then decays into a lepton (electron) and an antilepton (positron).

$$\alpha(m_{ll}^2) = \frac{\alpha_0}{1 - \frac{\alpha_0}{3\pi}\left[\sum_f e_f^2 N_c \left(\ln\left(\frac{m_{ll}^2}{m_f^2}\right) - \frac{5}{3}\right)\right]}, \tag{2.37}$$

where $\alpha_0 = 1/137$, the fine structure constant. The summation seen in Equation (2.37) is over all fermions f, both quarks and leptons, that have masses less than the invariant mass m_{ll} of the final state.

For the process $q\bar{q} \to \gamma^* \to l\bar{l}$, the quantity e_q in Equation (2.36) is simply the charge of quark q. However, in order to include the $\gamma - Z$ interference and $q\bar{q} \to Z \to l\bar{l}$ contributions, the following replacement must be made:

$$\begin{aligned} e_q^2 \to e_q^2 &+ \frac{m_{ll}^2(m_{ll}^2 - m_Z^2)(1 - 4\sin^2\theta_W)}{8\sin^2\theta_W \cos^2\theta_W[(m_{ll}^2 - m_Z^2)^2 + m_Z^2\Gamma_Z^2]} v_i e_q \\ &+ \frac{3m_{ll}^4 \Gamma_{Z\to l\bar{l}}}{16\alpha m_Z \sin^2\theta_W \cos^2\theta_W[(m_{ll}^2 - m_Z^2)^2 + m_Z^2\Gamma_Z^2]}(v_i^2 + 1), \end{aligned} \tag{2.38}$$

where m_Z, Γ_Z, and $\Gamma_{Z\to l\bar{l}}$ are the Z mass, full width, and partial width to the $l\bar{l}$ final state, respectively. Also, θ_W is the Weinberg angle and v_i is $1 - (8/3)\sin^2\theta_W$ for up, charm, and top quarks and $-1 + (4/3)\sin^2\theta_W$ for down, strange, and bottom quarks. The first term in the replacement above represents the initial equation, considering only the γ^* contribution. The second term represents the contribution from the $\gamma - Z$ interference and the third term represents the Z-contribution to the cross section. So having made this replacement, Equation (2.36) represents the cross section for the lowest order Drell-Yan process $q\bar{q} \to \gamma^*/Z \to l\bar{l}$.

2.7 The Drell-Yan Process and the QCD Parton Model

At the start of the discussion on the Drell-Yan process, the quark and antiquarks were considered free and the cross section given by Equation (2.36) was obtained. Here they are considered to be constituents of protons and Equation (2.36) is taken to be a subprocess cross section. The full cross section must now be calculated by applying the Parton Model and the QCD corrections discussed earlier.

Using Equation (2.10), the cross section σ for producing a Drell-Yan lepton-antilepton pair in a proton-proton collision (to lowest order) is

$$\sigma = \sum_q \int dx_a dx_b [f_{q/A}(x_a) f_{\bar{q}/B}(x_b) + (q \leftrightarrow \bar{q})] \hat{\sigma}, \tag{2.39}$$

where $\hat{\sigma}$ is the cross section for the subprocess $q\bar{q} \to \gamma^*/Z \to l^+l^-$ given by Equation (2.36). Choosing a Lorentz frame such that the masses of the quarks are negligible gives $\hat{s} = \tau s$. Now rewriting Equation (2.39) in terms of x_a and τ yields

$$\frac{d\sigma}{d\tau} = \sum_{a,b} \frac{d\mathcal{L}_{ab}}{d\tau} \hat{\sigma}(\hat{s} = \tau s) = \sum_{a,b} \frac{d\mathcal{L}_{ab}}{d\tau} \left(N_c C_{q\bar{q}} \frac{4\pi e_q^2 \alpha^2}{3\tau s} \right). \tag{2.40}$$

The goal is to write Equation (2.40) in terms of the invariant mass m_{ll} of the lepton-antilepton pair. Substituting $\tau = m_{ll}^2/s$ gives

$$\frac{d\sigma}{dm_{ll}^2} = N_c C_{q\bar{q}} \frac{4\pi e_q^2 \alpha^2}{3m_{ll}^4} \sum_{a,b} \tau \frac{d\mathcal{L}_{ab}}{d\tau}. \tag{2.41}$$

Finally, substituting $dm_{ll}^2 = 2m_{ll}dm_{ll}$, the Drell-Yan differential cross section with respect to the invariant mass is obtained:

$$\frac{d\sigma}{dm_{ll}} = N_c C_{q\bar{q}} \frac{8\pi e_q^2 \alpha^2}{3m_{ll}^2} \sum_{a,b} \tau \frac{d\mathcal{L}_{ab}}{d\tau}. \tag{2.42}$$

A mathematical formula for the Drell-Yan differential cross section has been derived, however, only to lowest order. To increase its precision at higher orders, QCD corrections must be considered.

To lowest order, the Drell-Yan process is simply the annihilation of a $q\bar{q}$ pair to either a virtual photon or Z boson, which then decays into a lepton-antilepton pair. There are three first order processes that must be considered: the quark (or

antiquark) may emit a virtual gluon, the quark may emit a real gluon leaving l^+l^-g in the final state, the quark may scatter with a gluon eventually leading to l^+l^-q in the final state. These possibilities must be incorporated into the cross section equations and to do so the DGLAP equation and the QCD formalism are used. Using QCD, the cross section for the Drell-Yan process is

$$\begin{aligned}\sigma =& \sum_q \int dx_a dx_b [f_{q/A}(x_a, m_{ll}^2) f_{\bar{q}/B}(x_b, m_{ll}^2) + (q \leftrightarrow \bar{q})] \\ & \times \left[\hat{\sigma}_0 + \frac{\alpha_s(m_{ll}^2)}{2\pi} \hat{\sigma}_1 + \left(\frac{\alpha_s(m_{ll}^2)}{2\pi} \right)^2 \hat{\sigma}_2 + ... \right],\end{aligned} \tag{2.43}$$

where α_s is the running coupling constant of the strong force. The power of α_s represents the number of gluons involved in the process and the corresponding cross section $\hat{\sigma}_n$, $n = 0, 1, 2...$ is the cross section for that subprocess. The parton distribution functions $f_{q/A}(x_a)$ and $f_{\bar{q}/B}(x_b)$ for some fixed Q^2 have been evolved using the DGLAP equation to $Q^2 = m_{ll}^2$. These evolved PDFs are denoted by $f_{q/A}(x_a, m_{ll}^2)$ and $f_{\bar{q}/B}(x_b, m_{ll}^2)$ as seen in Equation (2.43). The corresponding differential cross section to next-to-leading order (NLO) is[3] [11]

$$\begin{aligned}\frac{d\sigma}{dm_{ll}} =& N_C C_{q\bar{q}} \frac{8\pi\alpha^2}{3m_{ll}^3} \tau \int dx_a dx_b dz \delta(x_a x_b z - \tau) \\ & \times \left[\sum_q e_q^2 [f_{q/A}(x_a, m_{ll}^2) f_{\bar{q}/B}(x_b, m_{ll}^2) + (q \leftrightarrow \bar{q})] \right. \\ & \times \left(\delta(1-z) + \frac{\alpha_s(m_{ll}^2)}{2\pi} D_q(z) \right) \\ & + \sum_q e_q^2 [f_{q/A}(x_a, m_{ll}^2)(f_{q/B}(x_b, m_{ll}^2) + f_{\bar{q}/B}(x_b, m_{ll}^2) + (q, \bar{q} \leftrightarrow \bar{q})] \\ & \left. \times \frac{\alpha_s(m_{ll}^2)}{2\pi} D_g(z) \right],\end{aligned} \tag{2.44}$$

where the functions $D_q(z)$ and $D_g(z)$ are defined as

[3]The renormalization scheme used here is the Modified Minimal Subtraction Scheme $\bar{\text{MS}}$. Renormalization schemes are used to absorb infinities that arise through perturbative QCD calculations beyond leading order.

$$D_q(z) = C_F \left[4(1+z^2)\frac{\ln(1-z)}{1-z} - 2\frac{1+z^2}{1-z}\ln z + \delta(1-z)\frac{2\pi^2-24}{3} \right] \quad (2.45)$$

$$D_g(z) = T_R \left[(z^2+(1-z)^2)\ln\frac{(1-z)^2}{z} + \frac{1}{2} + 3z - \frac{7}{2}z^2 \right], \quad (2.46)$$

where $C_F = (N_c^2-1)/2N_c$, $T_R = 1/2$, and $N_c = 3$ the number of colour charges. Equation (2.44) is the NLO differential cross section; higher order expressions of this quantity become increasingly difficult to calculate.

Chapter 3

The ATLAS Experiment

This analysis uses collisions produced by the LHC [12] and measured with the ATLAS detector [13]. In this chapter, some technical aspects of the LHC are briefly introduced and following this, the components that comprise the ATLAS detector are described in detail. This chapter focuses on the hardware of the experiment rather than the physics of detection, which is described in the following chapter.

3.1 The Large Hadron Collider

Operating near Geneva, Switzerland at the European Organization for Nuclear Research (CERN) is the Large Hadron Collider (LHC), a synchrotron particle accelerator consisting of two beam pipes, each containing a counter circulating beam of protons. The LHC is 26.7 km in circumference and it is designed at full capacity to collide protons at 14 TeV in centre of mass energy, $\sqrt{s}$, with an instantaneous luminosity, $\mathcal{L}$, of 10^{34} cm^{-2}s^{-1}. Six experiments are being conducted using LHC collisions: ALICE, CMS, LHCb, TOTEM, LHCf, and ATLAS. After initial testing, the LHC began operating in 2010 running at 7 TeV. In early 2012, the LHC increased its centre of mass energy to 8 TeV and is currently running at this energy today. A schematic of the LHC can be seen in Figure 3.1.

The LHC accelerates and collides bunches which are discrete packets of protons equally spaced apart by some pre-determined distance or time. For each of the two beams, many bunches, collectively known as a bunch train, are accelerated to half the centre of mass energy, $1/2\sqrt{s}$, and subsequently collided at centre of mass energy of $\sqrt{s}$. The instantaneous luminosity varies with the number of protons filling each

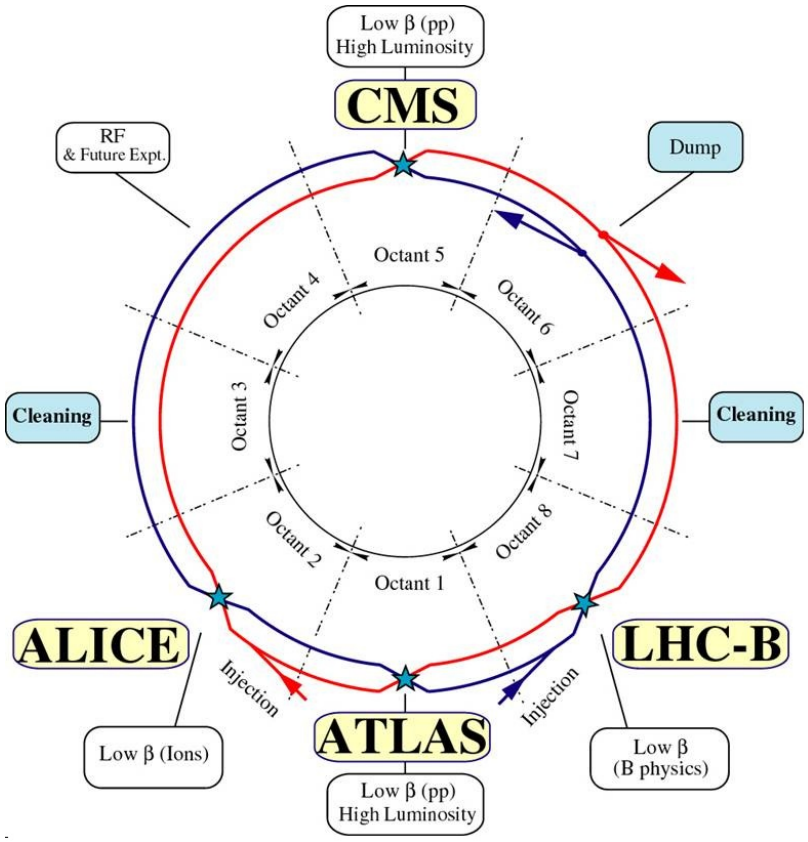

Figure 3.1: A schematic diagram of the LHC. This diagram shows the relative placement of the ATLAS experiment relative to the other major experiments being conducted around the LHC.

bunch and the number of bunch trains in each beam.

The rate R_{cross} of bunch crossing in the LHC is the product of the frequency f_r of revolution and the number n_b of proton bunches:

$$R_{cross} = f_r n_b. \tag{3.1}$$

Let R_{events} denote the number of events of interest per unit time. It is given by

$$R_{events} = \sigma \mathcal{L}, \tag{3.2}$$

where σ is the cross section corresponding to the particular process. Dividing Equation (3.2) by Equation (3.1) gives the number of events of interest per bunch crossing:

$$R_{events/cross} = \frac{R_{events}}{R_{cross}} = \frac{\sigma\mathcal{L}}{f_r n_b}. \tag{3.3}$$

This analysis uses LHC collision data recorded in 2011 at $\sqrt{s} = 7$ TeV with 50 ns bunch separation with 1331 bunches per train and a peak instantaneous luminosity of 3.6×10^{33} cm^{-2}s^{-1} [14]. At this energy, the inelastic proton-proton cross section is 60.3 ± 2.1 mb [15]. Substituting these quantities into Equation (3.3) gives approximately 14.5 ± 0.51 inelastic proton-proton collision events per bunch crossing. The phenomenon of multiple events occurring per bunch crossing is known as pileup.

3.2 The ATLAS Detector

The A Toroidal LHC ApparatuS (ATLAS) detector is one of the major experiments being conducted at CERN using LHC collisions. The ATLAS detector, depicted in Figure 3.2, is 44 m in length and 25 m in diameter, weighing about 7,000 t. The protons collide in a vacuum tube at the centre of the detector which is arranged in concentric layers or subdetectors, each measuring certain aspects of the particles created in the collisions. The subdetector closest to the vacuum tube is known as the inner detector, which is followed by the calorimetry system, and finally the muon detectors. Superconducting magnet systems are used to bend electrically charged particles so that momentum measurements can be made. A solenoid, located between the inner detector and the calorimetry system, produces an axial magnetic field inside the inner detector volume and a toroidal magnetic field in the muon systems is created by coils of superconducting material. There is a system called the trigger that determines whether a collision event is recorded or discarded.

3.2.1 Coordinate System

The experiment uses a mixture of Cartesian and spherical polar coordinate systems. For both coordinate systems, the origin is at the point of interaction of the two proton beams. The z axis lies along the beam axis, with the positive direction such that it forms a right handed coordinate system with the positive x direction toward the centre of the LHC ring and the positive y direction, which is upward. The polar angle θ is measured from the z-axis and the azimuthal angle ϕ is measured from the x-axis in the transverse (x, y) plane. In place of θ, pseudorapidity, defined earlier

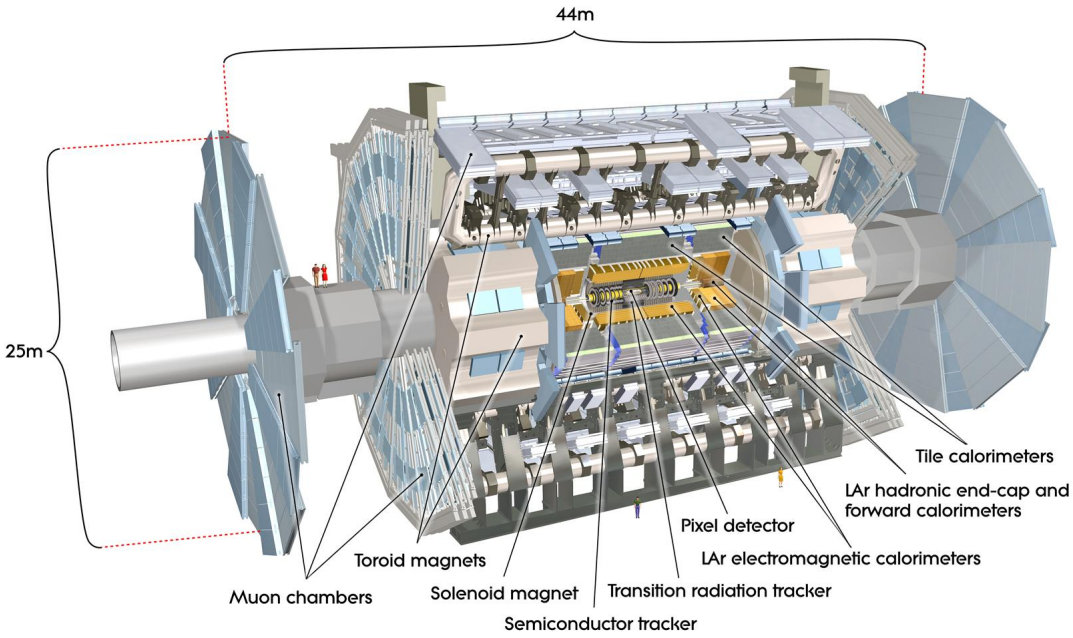

Figure 3.2: A cutaway view of the ATLAS detector. The major components that comprise the ATLAS detector are labelled in this diagram. The overall dimensions of the ATLAS detector is also given.

(Equation (2.21)) as $\eta = -\ln(\tan(\theta/2))$, is often used.

3.2.2 Inner Detector

The inner detector [16], seen in Figure 3.3, is the subdetector closest to the vacuum chamber. It measures the direction, momentum, and sign of electrically charged particles, and can provide some information on the identity of the particles. The inner detector is responsible for providing path and vertex information for the entire ATLAS system. The inner detector itself is also layered, comprising a high resolution pixel detector, a semiconductor tracker, and a lower resolution transition radiation tracker. The whole inner detector extends to pseudorapidity $|\eta| < 2.5$.

As a charged particle traverses through the inner detector, it produces a set of signals in each of the subcomponents. These signals are then reconstructed, giving the trajectory of the charged particle. Due to the magnetic field created by the solenoid magnet, the path (also known as the track) of the charged particle is curved. The curvature of the track reveals information about the momentum and sign of the

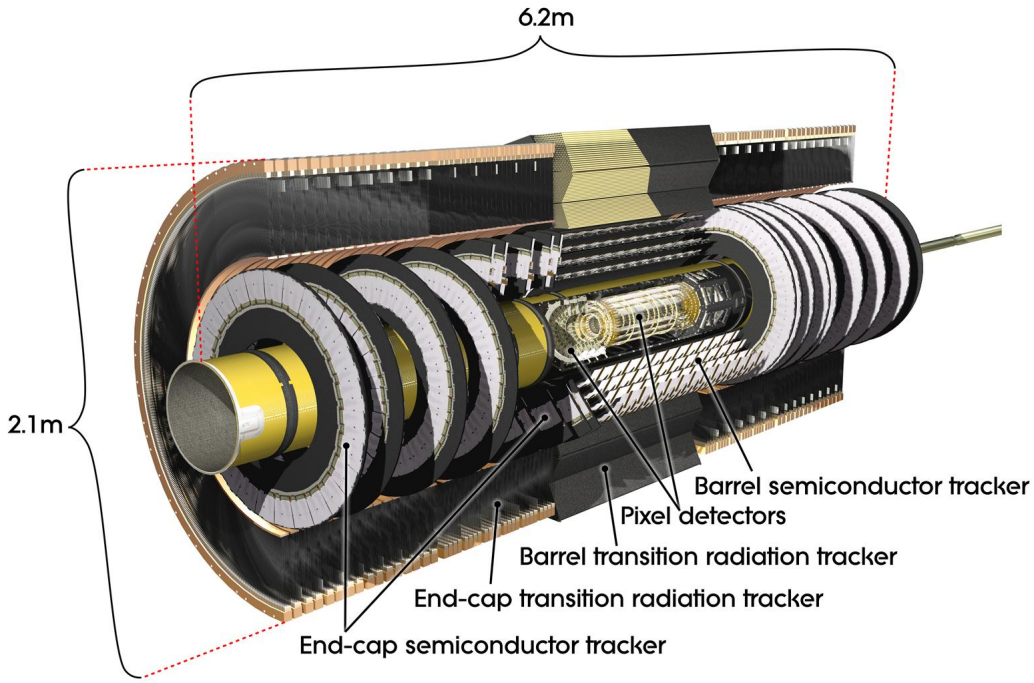

Figure 3.3: A cutaway view of the inner detector with its components labelled. The inner detector is comprised of a barrel region and two end-cap regions.

charged particle.

Each proton-proton collision produces a set of tracks measured by the inner detector and where these tracks intersect is known as the vertex. There are often several vertices in a proton-proton collision event because of pileup and the decay of longer lived particles. The number of vertices in an event is determined using information from the inner detector.

Pixel Detector

The innermost layer of the inner detector is the pixel detector [17]. The pixel detector consists of three concentric cylindrical layers of silicon wafers around the beam pipe at radii of 5, 9, and 12 cm each with a length of approximately 1.3 m. Also making up the pixel detector are three disks or end-cap modules perpendicular to the beam axis at both ends, ranging from 9 to 15 cm from the interaction point. Each thin layer is divided into approximately 80 million pixels with a minimum size of 50 μm in $r - \phi$ and 400 μm in z. The high granularity of the pixel detector makes it possible

to find tracks even when there are hundreds of particles going through the detector. The pixel detector has an intrinsic resolution of 10 μm in $r-\phi$ and 115 μm in z.

Semiconductor Tracker

Similar to the arrangement of the pixel detector, the semiconductor tracker (SCT) consists of four concentric cylinders [18] around the beam axis and nine disks [19] perpendicular to the beam at both ends of the detector. The cylindrical modules are approximately 1.5 m in length, located at radii of 30, 37, 44, and 51 cm from the beam axis and the end-cap modules range in radius from 26.7 to 56 cm and they are positioned from 0.85 to 2.7 m from the interaction point. The semiconductor tracker uses silicon microstrip technology for the tracking of charged particles and momentum measurements. There are approximately 6 million readout channels in total. The intrinsic resolution of the semiconductor tracker is 17 μm in $r-\phi$ and 580 μm in z.

Transition Radiation Tracker

The final component of the inner detector is the transition radiation tracker (TRT) [20] which, like the pixel detector and semiconductor tracker, has both barrel and end-cap modules. The TRT is made of gas-wire drift tubes, aptly called straw tubes, that are 4 mm in diameter. The straw tubes are filled with a xenon gas mixture used to detect transition radiation, and in each tube is a gold-plated tungsten wire used as the anode. The barrel module has an inner radius of 56 cm and an outer radius of 106 cm and is 6.8 m in length, covering a psuedorapidity region of $|\eta| < 2.0$. It is composed of 144 cm long straw tubes positioned parallel to the beam. The TRT end-cap module is split into 18 wheels per end, each with an inner radius and outer radius of 63 and 103 cm, respectively. They are positioned from 0.83 to 3.4 m from the interaction point. The end-cap region contains straw tubes of length 37 cm radially outwards, arranged in a wheel pattern.

Providing approximately 36 hits per track and long track lengths, the transition radiation tracker provides momentum measurements of charged particles. Photons (or transition radiation) are produced when a charged particle traverses through the polypropylene fibres (in the barrel) and foils (in the end-cap) interspaced between the straw tubes. These transition photons are then detected by the xenon gas in the tubes. The amount of transition radiation emitted is proportional to E/m, where E

is the energy and m is the mass of the charged particle. So then at a given energy, the TRT helps distinguish lighter particles, namely electrons, from heavier ones.

3.2.3 Calorimetry

Beyond the inner detector and the solenoidal magnet is the ATLAS calorimetry system, shown in Figure 3.4, which covers the pseudorapidity region $|\eta| < 4.9$. The calorimetry system provides measurements of both the energy and position of charged and neutral particles. To perform these measurements, the ATLAS calorimetry system uses sampling calorimetry. A sampling calorimeter consists of several layers, alternating between an absorber material and an active material. The absorber is used to create particle showers, a cascade of secondary particles produced as a result of the primary particle interacting with matter, within a certain depth and the active material measures the energy of the particles through ionization. The ATLAS calorimetry system uses two active materials, liquid argon (LAr) [21] and scintillating tiles [22].

The LAr calorimeters are divided into two types: electromagnetic (EM) and hadronic. The LAr EM calorimeter, which is closer to the interaction point, specializes in measuring electrons and photons while the hadronic calorimeter is optimized to measure hadronic particles. The LAr EM calorimeter has modules both in the barrel region and end-cap regions whereas the LAr hadronic calorimeter has modules only in the end-cap regions. The scintillating tile calorimeters are found only in the barrel region and are designed for hadronic calorimetry.

The Electromagnetic Calorimeter

The ATLAS electromagnetic calorimetry system uses LAr technology. It is divided into three sections, one positioned around the barrel and two located in the end-cap regions. Each of the three components are placed inside a cryostat filled with LAr, the active material. The energy resolution of the EM calorimeter is $\sigma_E(E)/E = 10\%/\sqrt{E} \oplus 0.7\%$.

In the barrel region, the EM calorimeter is split into two equal sections around $|\eta| = 0$ with a 4 mm crack existing between the two half barrels. Each half barrel has an inner diameter of 2.8 m and an outer one of 4 m, both spanning 3.2 m in length. In terms of pseudorapidity, the barrel region spans $|\eta| < 1.475$. The two end-caps span a range of $1.375 < |\eta| < 3.2$ with each being divided into an inner wheel

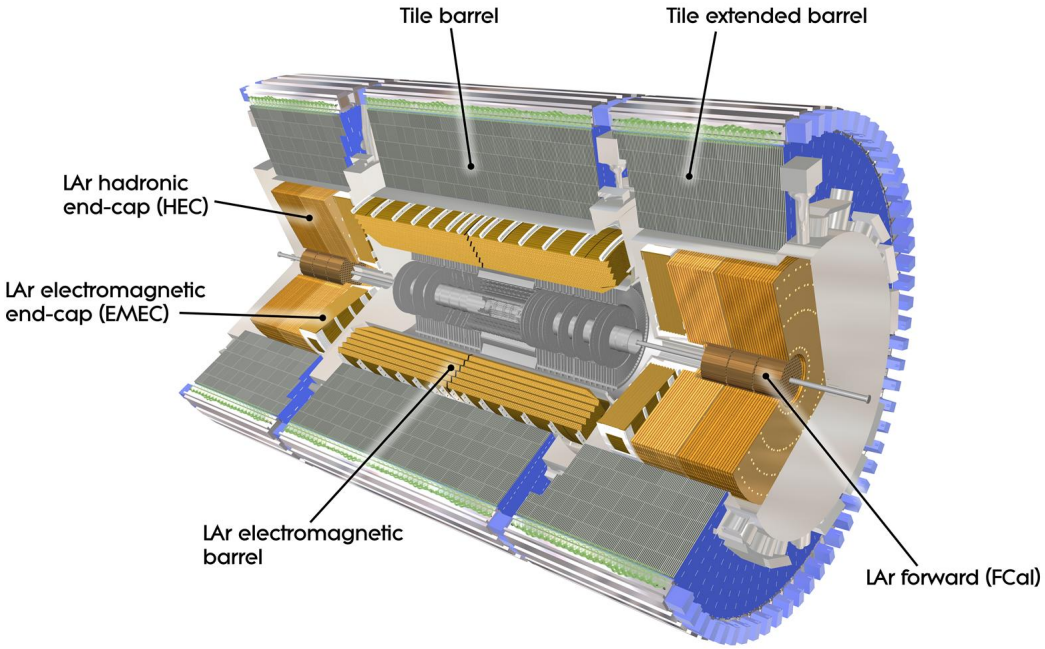

Figure 3.4: A cutaway view of the calorimetry system with its components labelled. The ATLAS calorimetry system is comprised of a barrel region and two end-cap regions.

($2.5 < |\eta| < 3.2$) and an outer wheel ($1.375 < |\eta| < 2.5$) with a 3 mm gap between the two. There is also a gap, known as the crack region, between the barrel and the end-cap at $|\eta| \approx 1.4$ used to route cables and services from the inner detector. There exist scintillators in the crack region; however, they are not yet well calibrated thus making this region problematic for physics analyses.

The EM calorimeters (both in the barrel and end-caps) use lead plates as the absorber material, which create the particle showers. The cascade of particles then ionize the liquid argon and the resultant negative charges and positive ions drift toward positive and negative readout plates, respectively. The drift speed of the negative charges is orders of magnitude greater than that of the ions, so it is the negative charges that are sampled. The readout electrodes are made of three layers of copper, separated by insulating layers of polymide. Both the lead absorbers and copper electrodes are arranged into accordion shapes. In the barrel, the accordion structure is arranged axially with waves in the radial direction. In the end-cap regions, the accordion wave structure is parallel to the radial axis. Diagrams showing the accordion structure

of both of these components can be seen in Figure 3.5. The accordion shape of the EM calorimeters provides excellent ϕ symmetry and hence hermetic containment of electromagnetic showers. The angle of folding and amplitude of the accordion structures are varied to keep the combined thickness of the lead absorbers and electrodes constant in the η direction hence maintaining uniform response. There are 101760 readout channels in the barrel and 62208 channels in each of the end-caps.

The electromagnetic calorimeters are approximately 22 radiation lengths thick in the barrel region and 24 radiation lengths in the end-cap regions. For the region $|\eta| < 2.5$, the EM calorimeters are segmented into three longitudinal layers. The layer closest to the beam pipe has the finest η segmentation, with a granularity of $\Delta\eta\times\Delta\phi = 0.0031\times0.1$. The middle layer has a granularity of $\Delta\eta\times\Delta\phi = 0.025\times0.025$. The outermost layer has a granularity of $\Delta\eta \times \Delta\phi = 0.050 \times 0.025$. These three layers have approximate thicknesses of 4, 16, and 4 radiation lengths, respectively. It is in the middle layer where electrons and photons deposit the majority of their energy.

Placed in front, $|\eta| < 1.8$, of each of the EM calorimeters is an active layer of LAr known as the presampler. The presampler is used to correct for the energy loss in the un-instrumented materials in front of the EM calorimeters. It has segmentation $\Delta\eta \times \Delta\phi = 0.025 \times 0.1$. In the barrel, it has a thickness of 1.1 cm and 7808 readout channels; in the end-caps, it has thickness 0.5 cm and 1536 readout channels.

The Hadronic Calorimeter

Located behind the electromagnetic calorimeter is the hadronic calorimeter. The ATLAS hadronic calorimetry system is comprised of several subdetectors, each using one of two technologies to measure hadronic particles. These two technologies are tile scintillating calorimetry and LAr calorimetry. The longitudinal depth of the hadronic calorimeters is approximately 10 interaction nuclear lengths, long enough to contain highly energetic hadrons.

In the barrel region, the hadronic calorimeter is split into a barrel and two extended barrels; these components use tile scintillation. Found in the end-cap regions are the LAr hadronic end-cap calorimeters and the LAr forward calorimeters. These components are optimized to measure the energy of hadronic particles in conjunction with the electromagnetic calorimeter[1].

[1]Electrons and photons that originate from the centre of the detector do not leave signals in the hadronic calorimeter. They deposit essentially all their energy before reaching the hadronic calorimeter.

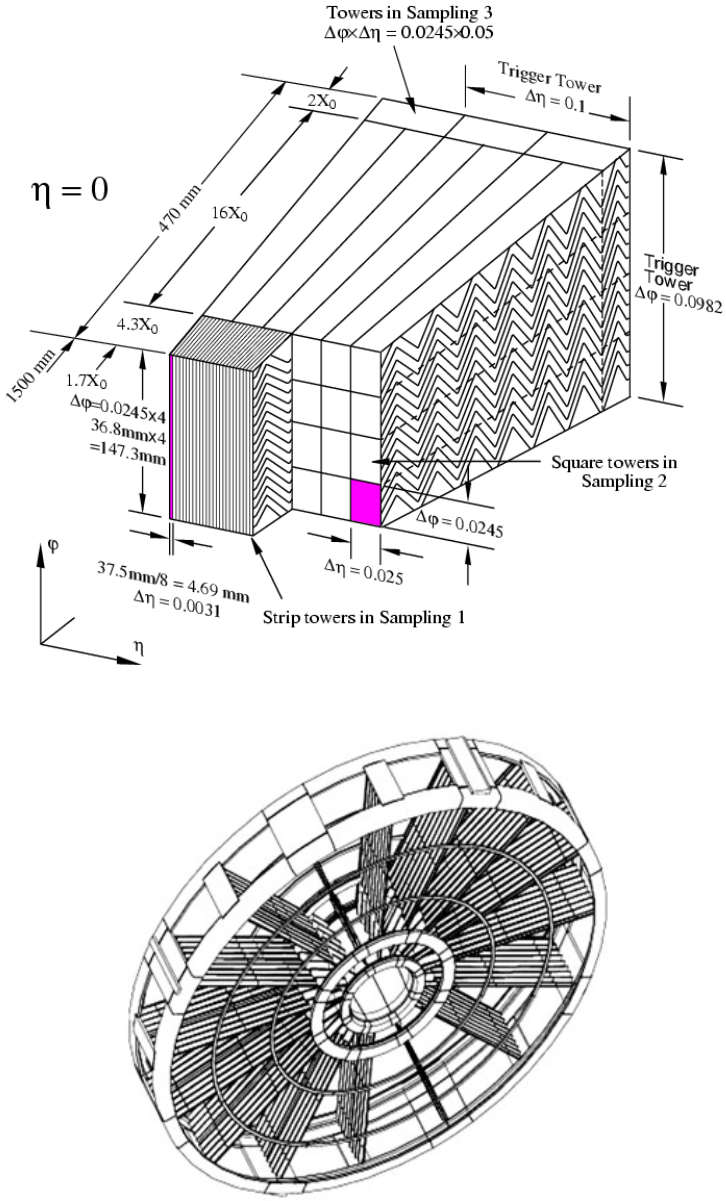

Figure 3.5: A cutaway view of the electromagnetic calorimeter barrel (top) and end-cap (bottom) modules. The accordion structure of these components can be seen.

The barrel region covers $|\eta| < 1.0$ and the extended barrel regions cover $0.8 < |\eta| < 1.7$. Spanning a radius of 2.28 m to 4.25 m, the tile calorimeters use steel as absorbers (14 mm thick) and scintillating plastic tiles (3 mm thick) as the active material. Layers of steel and plastic tiles are arranged such that they point towards the centre of the detector. The scintillating tiles are read out by photomultiplier

tubes connected by fibre cables.

In the end-cap regions, $1.5 < |\eta| < 3.2$, instead of scintillating plastic tiles, LAr is the active material and copper plates are the absorbers. The calorimeters in the very forward region $3.1 < |\eta| < 4.9$ have an EM component made of copper absorbers in addition to a hadronic component made of tungsten absorbers.

3.2.4 Muon Spectrometer

Surrounding all other subdetectors is the muon spectrometer [23], seen in Figure 3.6. The muon spectrometer measures the curvature of the tracks of highly energetic muons that cannot be stopped by the other components of the ATLAS detector. Muon tracking chambers are positioned around the detector and superconducting air-core toroidal magnets providing a magnetic field up to 4 T are positioned such that they bend the trajectory of the muons. In region $|\eta| < 1.4$, the large barrel toroid provides the magnetic field while in the region $1.6 < |\eta| < 2.7$, the bending is done by end-cap toroidal magnets.

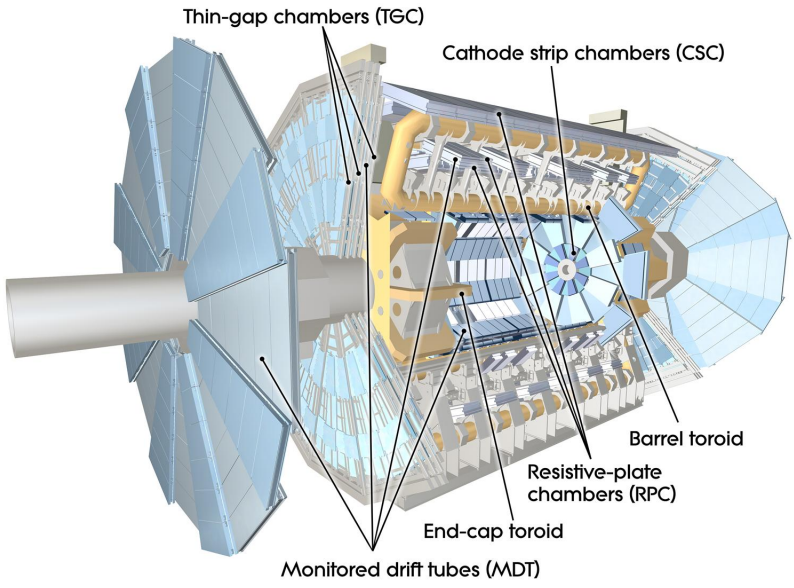

Figure 3.6: A cutaway view of the muon spectrometer. The muon detector is comprised of a barrel region and two end-cap regions.

The muon spectrometer employs several technologies: monitored drift tubes, cathode strip chambers, resistive plate chambers, and thin gap chambers [24]. These components are used to trigger and reconstruct muon tracks.

3.2.5 Trigger System

The LHC collides proton bunches at an overwhelmingly high rate; at design luminosity this rate is 40 MHz. Each event requires approximately one megabyte of storage space and given a rate of 40 MHz, 40 terabytes of collision data would be stored each second in order for ATLAS to record every event. This is impossible given the limitations of current technology. To circumvent this problem, each event is sent through the ATLAS trigger system which determines whether an event should be recorded or discarded. Those events that pass the trigger system are eventually saved onto computer tape to be analyzed later while those that do not are discarded.

The ATLAS trigger system is comprised of three levels of triggers, the first level (L1) [25] is hardware based while the second (L2) and third, known as the event filter (EF), are purely software based. The L2 and EF triggers combined are referred to as the high level trigger (HLT) [26]. The L1 trigger uses the simplest algorithm of the three requiring the least amount of time, known as decision time or latency, to determine whether a physical process of interest has occurred. Moving from L1 to L2 and finally to the EF trigger, the algorithms increase in complexity, sophistication, and latency. The actions performed by the L2 and the EF triggers depend on the decisions made in the prior levels, with the final decision resting on the EF. The series of triggers is known as the trigger chain.

The L1 trigger uses information from only the calorimetry system and the muon spectrometer passing only those events satisfying some momentum or energy criteria. It reduces the event rate from 40 MHz to 75 kHz with a decision time of about 2 μs. In addition to passing or rejecting an event, the L1 trigger also identifies regions in the calorimeter or muon spectrometer where an interesting physics object was found. These regions are known as regions of interest (ROI) and they allow the HLT to make decisions faster than they otherwise would going directly to the calorimeter or muon spectrometer for this information.

The L1 trigger feeds information to the L2 trigger which then uses this information and the ROI to make a decision on whether an event should be passed or rejected. It can also make use of other subdetectors (such as the inner detector) in making its decisions. The L2 trigger reduces the data rate from 75 kHz to a rate of 3.5 kHz with a decision time up to 40 ms.

The last level of the ATLAS trigger system is the EF which uses complex software algorithms in making its decisions. Seeded by the L2 trigger, the events that pass the

EF are those that will later be used in the offline analysis. The decision time of the EF is approximately 1 to 4 s. Using several processors, the data rate can be reduced down to about 200 Hz.

A data acquisition system is used in conjunction with the trigger system. Before the L1 trigger makes a decision, the data are stored in an independent buffer. Data that pass the L1 trigger are sent to readout drivers and are then stored in readout buffers. This information, which corresponds to the ROI, is accessed by the L2 trigger, running its algorithms over it. If the data are passed by the L2 trigger, they are then processed by the event builder which provides fully assembled events. Once the EF accesses and passes these events, they are then saved to permanent storage.

For the triggers that have too many events passing at each stage, only a predetermined fraction of events are allowed to pass, reducing the burden on the data acquisition system. This fraction is known as the prescale. Prescaling can occur at any level of trigger, but is typically done at L1. For example, a prescale factor of 10 for some trigger implies that only 1 event for every 10 is recorded for this particular trigger. Another method of reducing the number of events that pass some trigger uses a trigger threshold. For example, a trigger threshold could be the lowest transverse momentum a physics object may have in order to be considered by this trigger. An event containing an electron with transverse momentum 5 GeV would not be considered by some trigger with threshold 12 GeV, but an event containing a 15 GeV electron would. Prescales and trigger thresholds reduce the burden on the ATLAS trigger and data acquisition systems.

Chapter 4

Event Selection

This chapter begins with a discussion of the structure of ATLAS data and the data set used in this analysis. Following this is a description of ATLAS Monte Carlo (MC) production and the MC samples used in this analysis. In particle physics, processes of interest are reconstructed and identified by the characteristic signatures they leave in the detector. An outline of how electrons are reconstructed and identified is given. Several definitions used in the identification process of Drell-Yan pairs will be developed. Then a series of electron and pair selection requirements, or cuts, are presented. Each candidate electron-positron pair must pass these requirements before the pair can be considered to have originated from a Drell-Yan event.

4.1 ATLAS Data

Events that pass all levels of the ATLAS trigger system are written to permanent storage. At the event filter stage, a selection process is applied to each event classifying it with respect to the various ATLAS physics streams which include the electron and photon, muon, jet, and missing transverse energy streams. This process reduces the number of events irrelevant to a particular stream thereby reducing the time required to reconstruct and analyze the data.

After classification by physics stream, events are reconstructed. Reconstruction is the recreation of all final state physics objects found in the events using information provided by the detector. The process of reconstruction involves identifying the particles, determining what types of particles were created, and calculating their four-momenta. These reconstructed events along with the detector information used

in their reconstruction are then recorded into a data format known as event summary data (ESD). An analysis object data (AOD), containing the reconstructed events, is derived from the ESD. Each physics stream has its own set of AOD files and these files are made available to the ATLAS collaboration for physics analysis.

ATLAS data taking is divided into periods with each typically lasting for several weeks. Periods are classified by consistent running conditions which include for example the luminosity or bunch grouping of the accelerator. Each period is further divided by runs which are sustained intervals of data collection often lasting on the order of a few hours. Finally, a run is divided into luminosity blocks; a luminosity block is a collection of data nominally lasting for 60 s. A luminosity block is defined to have a single value of luminosity, which is taken to be the average over the 60 s collection time.

To track the quality of data to be used in an analysis, a good run list (GRL) is used. A GRL is a list of runs and luminosity blocks that were collected with stable LHC and ATLAS conditions and are appropriate for the analysis being done. Several quality checks are performed such as the stability of the LHC beams, the inclusion of all subdetectors during data collection, and the absence of any hardware problems. Runs and luminosity blocks that pass these quality checks are listed on the GRL.

4.2 Analysis Data

This analysis uses LHC proton-proton collision data at a centre of mass energy of $\sqrt{s} = 7$ TeV with a 50 ns bunch separation collected using the ATLAS detector. It was collected between March and July 2011 corresponding to data periods D to J belonging to the EGamma (electron and photon) physics stream. A table showing the total number of events in each data period set can be seen in Table 4.1.

These data periods were chosen because the di-electron trigger EF_2e12_medium was not prescaled. For the remaining data periods, this trigger was prescaled. The EF_2e12_medium trigger has an E_T threshold of 7 GeV at L1 and a threshold of 12 GeV at EF for candidate electrons. The runs are selected using the Standard Model group official Good Run List WZjets_allchannels_v4. The integrated luminosity of data sets D to J is 1.68 fb^{-1}, while the instantaneous luminosity was between 2×10^{32} cm^{-2}s^{-1} and 2×10^{33} cm^{-2}s^{-1} with 5.6 interactions per bunch crossing on average.

Period	Events [$\times 10^6$]
D	37.2
E	8.16
F	17.6
G	57.2
H	29.5
I	39.7
J	22.0

Table 4.1: A list of the 2011 data periods used in this analysis with their corresponding number of events.

4.3 ATLAS Monte Carlo

Monte Carlo simulation [27] is used heavily, not only by ATLAS, but by the entire particle physics community. It is used to study detector response, which often does not have an analytic representation, and to compare theoretical predictions with measurements. ATLAS MC is processed the same way and uses the same framework as experimental data so that a direct comparison can be made between the two. In ATLAS, Monte Carlo is produced in three stages: generation, simulation, and reconstruction. The details of which will be briefly covered.

4.3.1 Generation

The first stage of MC production, known as generation, requires a generator, a model that contains collision physics such as PYTHIA [28] or HERWIG [29]. Generators produce lists of initial, intermediate, and final state particles in proton-proton collisions along with their four-momenta. Generators require parton distribution function sets as input. These PDF sets provide the necessary information about the protons prior to any collisions.

The generation stage begins with the collision of two protons in a hard scattering process. Initial or final state partons may radiate photons or gluons at any point along the generation stage. Final state partons will undergo hadronization, forming jets of hadrons which may be unstable and further decay. The partons that do not take part in the collision carry net colour charges and so too will hadronize.

4.3.2 Simulation

The next phase in MC production is known as simulation. In this stage, all generated particles are sent through a simulated version of the ATLAS detector. Every particle is tracked as it travels away from the point of collision and traverses the materials of the detector. The energy deposition of each particle in the detector is recorded. For particles that are created through the interaction of the generated particles with the detector material, the same information is also recorded. A process, called digitization, then converts the energy depositions into simulated signals from the subdetectors that comprise ATLAS. GEANT [30] is the simulation program used by the ATLAS experiment to describe the interactions of the generated particles with the elements of the ATLAS detector.

4.3.3 Reconstruction

The information produced in the simulation stage is fed into reconstruction software that builds files for analysis. This final state in the production of MC is known as reconstruction. These files contain information on objects such as electrons, photons, jets, and missing transverse energy. Particle physics analysis is run on these files. The reconstruction stage is performed the same way for both MC and data such that a direct comparison can be easily made between the two.

4.4 Analysis Monte Carlo

This analysis uses several MC samples to fully simulate the physics described by the data. A table of the samples can be seen in Table 4.2 which shows the Monte Carlo sample identification number, the physical process simulated, the cross section of that process, the filter[1] efficiency, and the number of events.

The Drell-Yan samples, $\gamma^*/Z \to e^+e^-$ and $\tau^+\tau^-$, and the $b\bar{b}(c\bar{c})$ sample are generated using the MC generator PYTHIA; the $t\bar{t}$ and diboson samples are generated with MC@NLO [31]. The $b\bar{b}(c\bar{c})$ and $t\bar{t}$ samples have filter efficiency $\epsilon_{filter} < 1$ as shown in the table. Events in the $b\bar{b}(c\bar{c})$ sample are required to have at least two electrons of $E_T > 10$ GeV and $|\eta| < 2.7$, resulting from leptonic or semi-leptonic decays of these quarks. The $t\bar{t}$ events are filtered such that they contain at least one lepton.

[1]Only MC events containing a final state e^+e^- pair are relevant. Those not containing an e^+e^- pair were filtered out.

MC number	Sample	σ [pb]	ϵ_{filter}	N_{event}
108320	$\gamma^*/Z \to e^+e^-, \sqrt{\hat{s}} \in [15, 60]$ GeV	1241	1.0	2.00×10^6
106046	$\gamma^*/Z \to e^+e^-, \sqrt{\hat{s}} \in [60, \infty)$ GeV	835	1.0	1.00×10^7
105759	$b\bar{b}(c\bar{c}) \to e^+e^-X$	5.9×10^5	0.0021	2.92×10^6
105200	$t\bar{t} \to e^+e^-X$	161	0.556	1.16×10^7
106052	$\gamma^*/Z \to \tau^+\tau^-$	833	1.0	2.99×10^6
105921	$W^+W^- \to e^+\nu_e e^-\bar{\nu}_e$	0.524	1.0	1.42×10^5
105931	$ZZ \to l^+l^-l^+l^-$	0.024	1.0	6.94×10^4
105941	$W^+Z \to l^+\nu_l l^+l^-$	0.159	1.0	1.87×10^4

Table 4.2: Monte Carlo samples. From left to right, the columns represent the MC sample identification number, the physical process, the associated cross section, the filter efficiency, and the number of events. The first two rows correspond to signal MC and the remaining rows correspond to background MC.

The pileup conditions of the MC listed above were set to mimic the pileup conditions of the full 2011 data set. The pileup conditions of the full 2011 data set are different from those of the data set used in this analysis; therefore, the MC samples must be reweighted. Pileup reweighting is applied to Monte Carlo samples by weighting each of the events by a pileup factor. For a given number of primary vertices, the pileup factor is the number of proton-proton collision events found in data divided by the number of events found in MC. Shown in Figure 4.1 is the distribution of primary vertices for the analysis data set and the MC, before and after pileup reweighting. The data points represent the number of events as a function of the number of primary vertices for the data set while the solid lines correspond to MC. The distributions seen in this figure are normalized to 100 so that a comparison can be made between their shapes.

4.5 Electron Reconstruction

Electrons are detected and measured using the inner detector and the electromagnetic calorimeter. An electron travelling out from a primary vertex first traverses through the inner detector. The first two components an electron interacts with are the pixel detector and the semiconductor tracker. The electron will produce electron-hole pairs in the silicon found in these two components. With the use of an electric field, the liberated electrons in the silicon induce a current collected by read-out channels. A

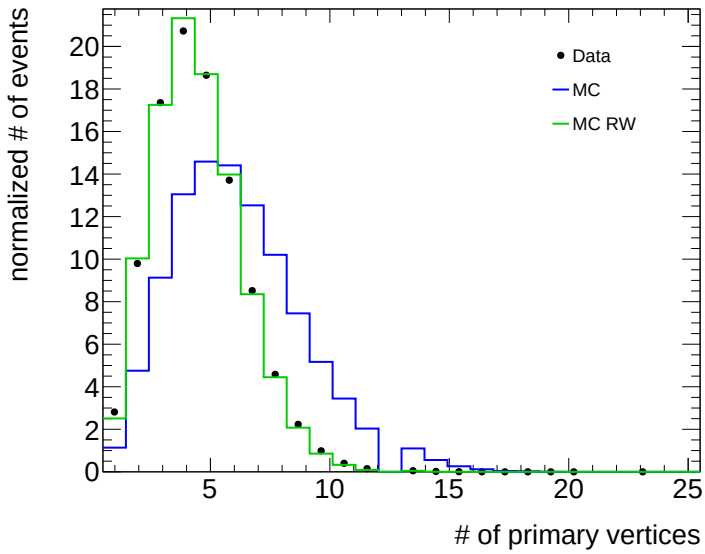

Figure 4.1: The effect of pileup reweighting on the MC samples. Shown is a distribution of the number of primary vertices for data and MC, before and after (MC RW) the reweighting procedure.

similar process occurs in the transition radiation tracker. The electron along with its transition radiation interacts with the gas mixture found there. The interactions induce a pulse on the gold-plated tungsten anode and this pulse is subsequently read-out. Each of the pixels containing a signal form the track of the electron. The track is curved due to the magnetic field created by the ATLAS magnet system. The direction of the track reveals the charge of the electron and its radius of curvature provides momentum measurements.

After the inner detector, the electron then reaches the electromagnetic calorimeter. As the electron traverses the calorimeter, it triggers a series of interactions which include bremsstrahlung, ionization, and pair production, collectively producing an electromagnetic shower that is contained within the electromagnetic calorimeter. The calorimeter samples and collects the ionization current produced by the particles making up the shower. The amount of ionization current collected is directly proportional to the energy of the original electron. The smallest read-out unit in the electromagnetic calorimeter is known as a cell. By summing all the energy deposited in each cell by the shower, the energy of the original electron can be determined. The collection of cells used in the determination of the electron energy is called an electromagnetic cluster.

Both photons and electrons can initiate showers in the electromagnetic calorimeter. The shower shapes produced by the two are similar and difficult to differentiate. Information from the inner detector is used to determine whether the shower was produced by a photon or an electron. Photons are of course neutral in electric charge and thus they do not leave tracks in the inner detector. In order then for an electron to be reconstructed, there must be a track corresponding to a singly charged particle measured in the inner detector and a matching electromagnetic cluster found in the calorimeter. This is shown in Figure 4.2 which illustrates the types of tracks left in the detector by several different types of particles.

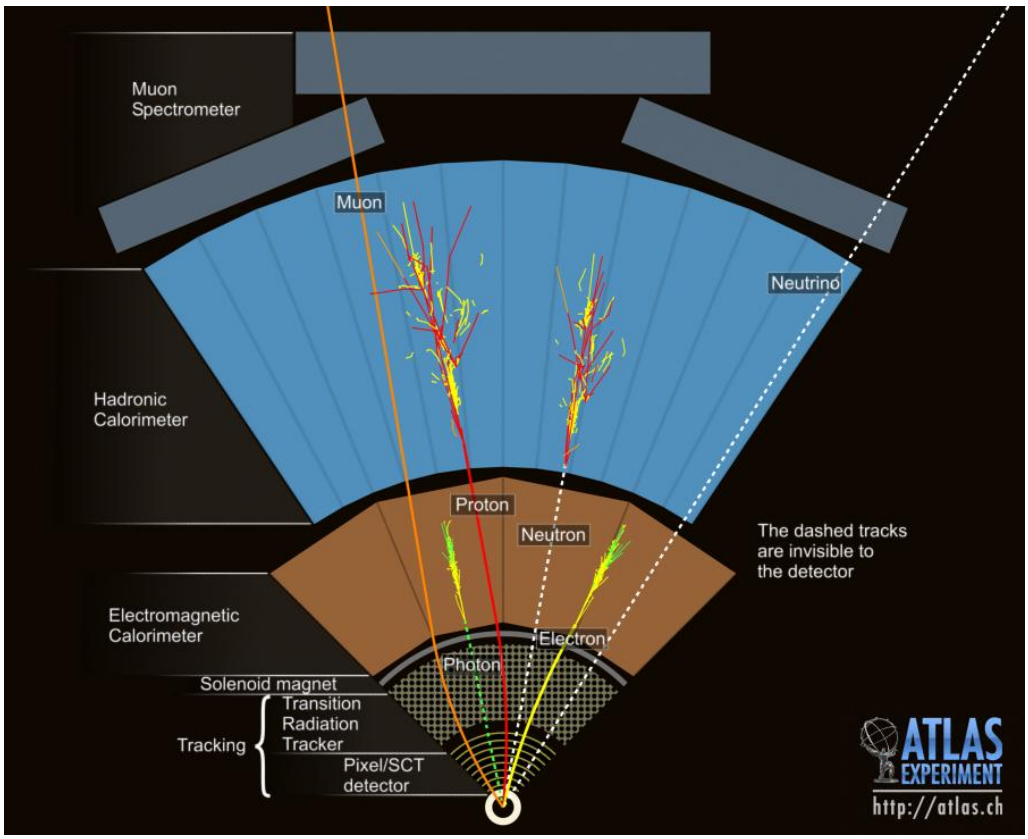

Figure 4.2: A diagram of various particle signatures left in the ATLAS detector. Notice that only the electron and photon shower and fully terminate in the electromagnetic calorimeter. The electron, however, leaves hits in the inner detector whereas the photon (a neutral particle) does not. Hence a particle that leaves hits in the inner detector and showers in the electromagnetic calorimeter is a candidate for electron reconstruction.

4.6 Electron Identification

A reconstructed electron with a track in the inner detector and a cluster of energy in the electromagnetic calorimeter may not in fact be a real electron. There are several particles, such as hadrons and muons, that can leave tracks and clusters. Conversely, the reconstructed electron may indeed be real, but be the decay product of a heavy flavour hadron. Such a decay leads to a real electron whose energy is measured in the electromagnetic calorimeter along with a significant amount of energy deposited nearby by a jet. A real electron that results from the decay of a hadron is known as a non-isolated electron. Non-isolated electrons are not of interest in this analysis. An electron that leaves a cluster in the calorimeter with no other nearby clusters is called an isolated electron. Drell-Yan electrons are isolated as they are produced from the decay of a γ^* or Z, not hadrons. To distinguish isolated electrons from non-isolated electrons, the characteristics of the electron candidates must be further investigated. This process is called electron identification.

Electron identification in ATLAS considers three things: the properties of the track, the properties of the electromagnetic shower, and the quality of match between the two. ATLAS has defined more than 20 quality-check variables that are used in the identification process; a few of the most important are listed below:

- ClusterIsolation is the ratio of energy deposited around an electromagnetic cluster in a cone with half opening angle $\Delta R \equiv \sqrt{\Delta\eta^2 + \Delta\phi^2}$ to the total energy of the cluster. For real electrons, this ratio is approximately zero.

- ClusterHadronicLeakage is the ratio of the transverse energy[2] deposited in the first layer of the hadronic calorimeter to the total transverse energy of the cluster measured in the electromagnetic calorimeter. A real, isolated electron will deposit all of its energy in the electromagnetic calorimeter without any leakage into the hadronic calorimeter, so this quantity should be zero for real, isolated electrons.

- TrackMatchEta is the difference between the cluster η determined using the first layer of cells in the electromagnetic calorimeter and the track η extrapolated to the first layer.

[2]The cluster transverse energy is defined as $E_{T,c} = E_c sin\theta_c$, where E_c is the energy and θ_c is the θ coordinate of the cluster measured by the EM calorimeter.

- TrackMatchPhi is the difference between the cluster ϕ determined using the first layer of cells in the electromagnetic calorimeter and the track ϕ extrapolated to the first layer.

- TrackMatchEoverP is the ratio of the cluster energy of the electron measured in the electromagnetic calorimeter to the track momentum measured in the inner detector. This ratio should be close to unity for a real electron as its mass is negligibly small compared to its energy.

ATLAS uses three standard definitions when identifying electrons: loose, medium, and tight. These definitions were written and are maintained by the ATLAS EGamma group [32]. A loose electron combines a fourth of the 20 quality-check variables. A medium electron includes all those used in loose identification plus 7 additional variables. Finally, a tight electron uses all 20 quality-check variables. Each of the three identification definitions is optimized to achieve a target efficiency for identifying real electrons or jet rejection. Loose identification selects real electrons at high efficiency, but at the expense of low jet rejection. Tight identification is highly efficient at jet rejection, but has poor efficiency when it comes to selecting real, isolated electrons. Medium identification falls in between the two.

4.7 Event Selection

Drell-Yan events in data from the EGamma stream, meaning events selected from electron or photon triggers, are searched for in this analysis. To reduce the amount of non-collision events found in data, events are required to have at least one primary vertex with three or more tracks of $p_T > 2$ GeV. The number of Drell-Yan events in the data set is determined first by performing electron selection. The following selection requirements are designed to keep electrons that fit the criteria of being a Drell-Yan electron. These cuts are applied in the following order to all electron candidates that remain after the event filter EF_2e12_medium:

1. When two electron candidates share the same track or cluster, the candidate with higher E_T is kept while the one with lower E_T is removed. If the separation between the two clusters has $\Delta\eta_c < 0.05$ and $\Delta\phi_c < 0.1$ or if the separation between the two tracks has $\Delta\eta_t < 0.001$ and $\Delta\phi_t < 0.001$, the electron candidate with higher E_T is kept while the other is discarded. This process is called duplicate removal.

2. Electron candidates are reconstructed using the sliding window algorithm. This technique starts with a window of fixed size in η and ϕ centred at some electromagnetic cluster found in the electromagnetic calorimeter. The window is moved in both η and ϕ directions and the energy inside the window is summed at each step. If the cluster has $E_T > 3$ GeV, then the initial cluster is kept and the algorithm continues on finding other electromagnetic clusters. In order for the object to be recognized as an electron, the cluster must have a matching inner detector track within a window of $\Delta\eta \times \Delta\phi = 0.05 \times 0.1$ and the ratio E/p of the cluster energy to the track momentum must be less than 10. Candidate electrons satisfying these criteria are known as standard electrons.

3. Electron candidates found in or near dead cell regions in the electromagnetic calorimeter are discarded.

4. Each electron candidate is required to have a cluster $E_T > 12$ GeV and a cluster $|\eta| < 2.4$ and each candidate must not be in the crack region $1.37 < |\eta| < 1.52$. The crack is the transition region between the barrel and the endcaps; it is a region that is not well calibrated. Electron candidates that pass these requirements are said to be within the kinematic acceptance or within the acceptance.

5. The candidates are required to pass EGamma's tight identification criteria which reduces background from jets or from secondary electrons originating from hadronic decays. As stated earlier, tight identification depends on several variables including hadronic leakage, track quality, cluster quality, track-cluster matching, and so on. Tight identification defines the electromagnetic cluster to be all cells within $\Delta R < 0.2$ around the electron candidate.

6. Finally, a strict electromagnetic calorimeter requirement is applied to the candidate electrons. This requirement is known as calorimeter isolation and it is designed to further reduce the jet background. Calorimeter isolation is defined to be the transverse energy outside the electron cluster, defined to be $\Delta R < 0.2$, but within $\Delta R < 0.4$ divided by the total electron cluster transverse energy. The calorimeter isolation must have values ranging from 0.13 to 0.18 depending on the cluster η of the candidate electron. These values were chosen to maximize the Drell-Yan signal efficiency times the purity.

Candidates that pass all these cuts are considered candidate Drell-Yan electrons plus some contamination from jets and competing background processes. A cut flow diagram of the requirements listed above can be seen in Figure 4.3. This diagram shows the number of electron candidates that fire the trigger EF_2e12_medium and the number of candidates that remain after each of the requirements listed above.

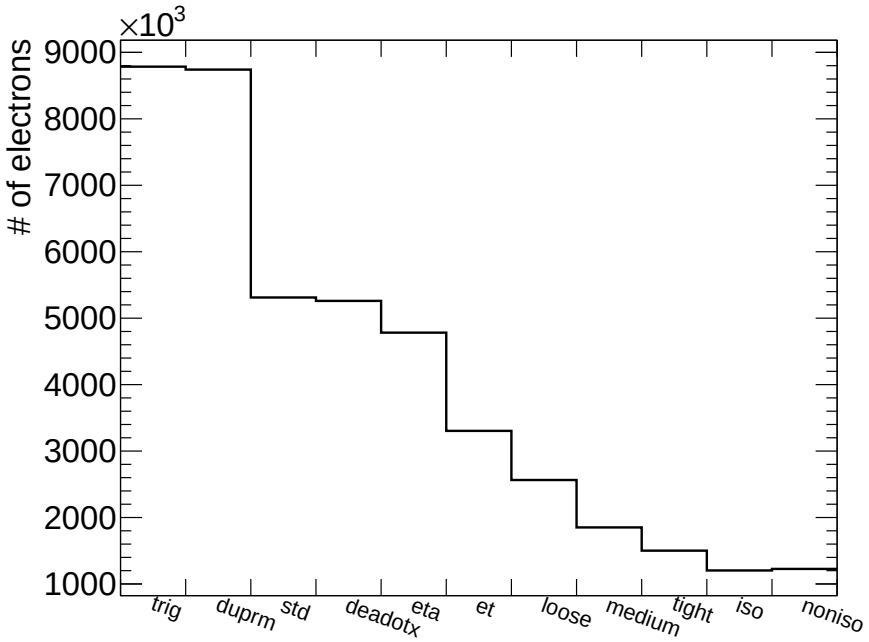

Figure 4.3: Cut flow diagram of the electron selection requirements. The leftmost entry of this histogram represents the number of electrons satisfying the event filter EF_2e12_medium. Following this, from left to right, are the number of electrons remaining after duplicate removal, requiring standard electrons, ensuring they are away from dead cell regions, applying the cluster η and E_T cuts, loose, medium, tight identifications, calorimeter isolation, and finally the number of electrons that do not pass calorimeter isolation.

Following individual electron selection is Drell-Yan pair selection:

1. For each event, exactly two electrons opposite in electric charge are selected, an electron-positron pair.

2. At least one of the two electrons must have (cluster) $E_T > 15$ GeV in addition to the original $E_T > 12$ GeV cut on all electrons.

3. The reconstructed invariant mass of the electron pair must be in the range[3] $26 < m_{ee}^{reco} < 66$ GeV.

Figure 4.4 shows the number of all possible pairs remaining after the E_T cut and loose, medium, and tight identifications and calorimeter isolation. Following the calorimeter isolation cut, events are then required to have exactly two electrons, opposite in electric charge. The last bin is the number (38,439) of pairs of oppositely charged electrons within invariant mass range $26 < m_{ee}^{reco} < 66$ GeV.

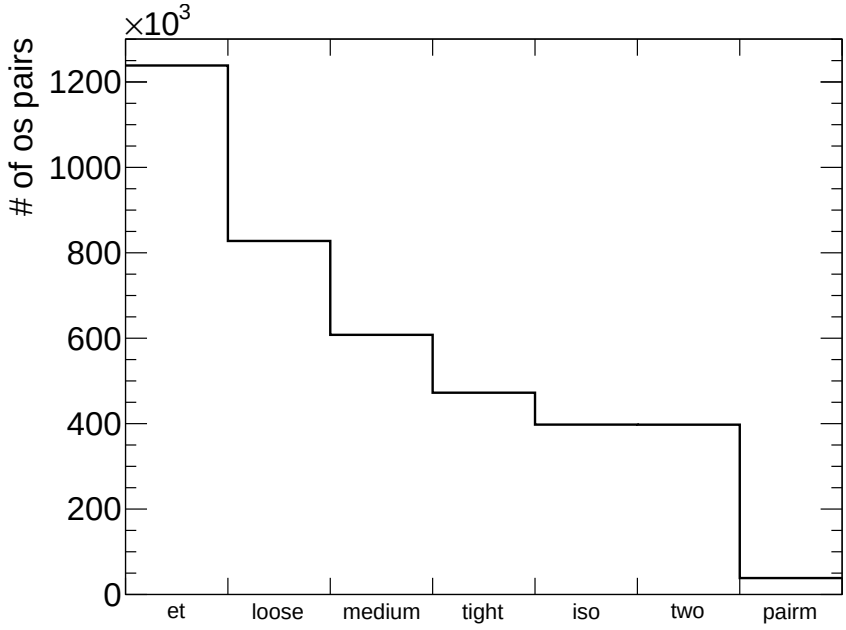

Figure 4.4: Cut flow diagram of the pair selection requirements. The entries of this histogram, from left to right, are the number of all possible pairs within kinematic acceptance, satisfying loose, medium, tight identifications, calorimeter isolation, demanding only two oppositely charged electrons per event, and pairs within the specified invariant mass range.

The electron pairs that satisfy all the requirements listed above, both the electron and pair selection requirements, are the Drell-Yan pairs plus some remaining contamination from jets and background processes.

[3]This invariant mass range is useful for constraining the parton distribution functions of the proton.

Chapter 5

Analysis Method

Several physical quantities need to be measured or calculated in order to determine the Drell-Yan differential cross section. These include the measured number of electron-positron pairs found in the data and an estimate of the number of the background pairs. Additionally, it requires the calculation of the selection efficiency, detector resolution, reconstruction efficiency, and kinematic acceptance needed to correct the measured spectrum. Having these, a differential cross section that is directly comparable to theory can be calculated. This chapter is an outline of the overall analysis [33]. It introduces the quantities required to compute and develops a mathematical equation for the differential cross section.

5.1 The Drell-Yan Differential Cross Section

The goal of this analysis is to measure the Drell-Yan differential cross section $\frac{d\sigma^{DY}}{dm_{ee}}$ corresponding to the process $pp \to Z/\gamma^* \to e^+e^-$. Let N^{DY} be the number of Drell-Yan pairs and σ^{DY} be its associated cross section. The relation between these two quantities, as was presented in Section 2.1, is

$$N^{DY} = \sigma^{DY} \int \mathcal{L}dt, \tag{5.1}$$

where $\int \mathcal{L}dt$ is the integrated luminosity describing the particle beams. Solving for σ^{DY} and differentiating with respect to the invariant mass m_{ee} of the electron-positron pair yields an expression for the Drell-Yan differential cross section with respect to the invariant mass:

$$\frac{d\sigma^{DY}}{dm_{ee}} = \frac{1}{\int \mathcal{L} dt} \frac{dN^{DY}}{dm_{ee}}. \tag{5.2}$$

The measurement of this quantity is the goal of this analysis. Experimentally, determining a differential cross section is non-trivial. The following sections will briefly outline the analysis in a mathematical treatment, and the following chapters of this thesis will present the steps and results in great detail.

5.2 Measurement and Background Estimation

Experimentally, the Drell-Yan process cannot be measured directly; however, all final states consisting of two opposite sign electrons e^+e^- can be measured directly. The first step of this analysis is determining the number of events that have an e^+e^- pair in the final state. Denote this number as

$$N_i^{ee}(m_{ee}^{reco})|_{data} = \alpha, \quad i = 1, 2, 3, ... \tag{5.3}$$

The notation in Equation (5.3) is important as it will be used throughout this thesis. The superscript ee indicates that the number N of e^+e^- pairs is being considered here. Also, N^{ee} is written as a function of m_{ee}^{reco}, the reconstructed e^+e^- invariant mass. The subscript i indexes the m_{ee}^{reco} bin of a histogram. This analysis uses both data and Monte Carlo, so a distinction must be made when a quantity is being calculated with data or MC. The subscript following the vertical bar in Equation (5.3) indicates that $N_i^{ee}(m_{ee}^{reco})$ is the number of pairs found in *data*. Finally, α is the integer number of e^+e^- pairs in m_{ee}^{reco} bin i.

It is important to note that $N_i^{ee}(m_{ee}^{reco})|_{data}$ represents the number of e^+e^- pairs coming from all reactions, not just the Drell-Yan process. In this analysis, all processes other than the Drell-Yan process capable of producing final state e^+e^- pairs are considered background. The possible background processes considered include

- $b\bar{b}(c\bar{c}) \to e^+e^-X$
- $t\bar{t} \to W^+W^-b\bar{b} \to e^+\nu_e e^-\bar{\nu}_e b\bar{b}$
- $\gamma^*/Z \to \tau^+\tau^- \to e^+\nu_e\bar{\nu}_\tau e^-\bar{\nu}_e\nu_\tau$
- $W^+W^- \to e^+\nu_e e^-\bar{\nu}_e$

- $ZZ \to e^+e^-e^+e^-$
- $W^+Z \to e^+\nu_e e^+e^-$.

To keep only electrons within the kinematic region of interest and reduce the contamination from background, a series of requirements which the electron pairs must pass is applied. These requirements, which were presented in detail in Section 4.7, include the following:

1. The event must pass the trigger EF_2e12_medium.
2. Both electrons must have $E_T > 12$ GeV with at least one having $E_T > 15$ GeV and they must both have $|\eta| < 2.4$, excluding the crack region $1.37 < |\eta| < 1.52$.
3. The pair must satisfy EGamma tight identification.
4. Both electrons must pass calorimeter isolation.

Let the number of e^+e^- pairs in m_{ee}^{reco} bin i that pass these requirements (along with those listed in Section 4.7) be written as

$$N_i^{ee}(m_{ee}^{reco}|E_T, \eta, id, iso, trig)|_{data} = \beta, \tag{5.4}$$

where β is some integer less than α. The events represented by this quantity are a subset of those represented by Equation (5.3). The labels E_T, η, id, iso, and $trig$ in Equation (5.4) are the requirements made on the e^+e^- pairs. There will remain some background e^+e^- pairs that also pass these requirements. The number of background pairs can be determined using MC samples simulating the background processes. Similar to Equation (5.4), denote the number of opposite sign background electron pairs as $N_i^{bkg}(m_{ee}^{reco}|E_T, \eta, id, iso, trig)|_{MC}$. The difference between these two quantities is the number of Drell-Yan pairs that pass these requirements:

$$\begin{aligned} &N_i^{DY}(m_{ee}^{reco}|E_T, \eta, id, iso, trig) \\ &= N_i^{ee}(m_{ee}^{reco}|E_T, \eta, id, iso, trig)|_{data} - N_i^{bkg}(m_{ee}^{reco}|E_T, \eta, id, iso, trig)|_{MC}. \end{aligned} \tag{5.5}$$

Note that the superscript in Equation (5.5) reads DY to indicate that the pairs are now Drell-Yan pairs. Substituting this equation into a discrete version of Equation (5.2) gives

$$\left(\frac{d\sigma^{DY}}{dm_{ee}}\right)_i (m_{ee}^{reco}|E_T,\eta,id,iso,trig) = \frac{N_i^{DY}(m_{ee}^{reco}|E_T,\eta,id,iso,trig)}{\Delta m_{ee,i}\int \mathcal{L}dt}, \tag{5.6}$$

where the index $i = 1, 2, 3, ...$ denotes the m_{ee}^{reco} histogram bin number and the quantity $\Delta m_{ee,i}^{reco} \equiv m_{ee,i+1}^{reco} - m_{ee,i}^{reco}$ represents the width of histogram bin i (set to 5 GeV throughout the entire analysis). Equation (5.6) is indeed a differential cross section, but a very specific one. It is not comparable to theory due to the selection requirements like tight identification and calorimeter isolation that were made. The following sections will outline the quantities needed and the techniques used to take this cross section to one that can be compared directly to theoretical predictions.

5.3 Selection Efficiency

Event selection requires both candidate electrons to pass the EF_2e12_medium trigger, tight identification, and calorimeter isolation before they are deemed a possible Drell-Yan pair. Associated with each of these three requirements is an efficiency, as only a certain portion of candidate pairs will pass these requirements. The Drell-Yan selection efficiency ϵ^{sel} is the product of the three individual efficiencies:

$$\epsilon_i^{sel}(m_{ee}^{reco}) = \epsilon_i^{id}(m_{ee}^{reco})\epsilon_i^{iso}(m_{ee}^{reco})\epsilon_i^{trig}(m_{ee}^{reco}), \quad i = 1, 2, 3, ..., \tag{5.7}$$

where ϵ_i^{id} is the tight identification efficiency for reconstructed invariant mass m_{ee}^{reco} bin i; ϵ_i^{iso} and ϵ_i^{trig} are the calorimeter isolation and EF_2e12_medium trigger efficiencies, respectively. These efficiencies are defined as

$$\epsilon_i^{id}(m_{ee}^{reco}) = \frac{N_i^{ee}(m_{ee}^{reco}|E_T,\eta,id)}{N_i^{ee}(m_{ee}^{reco}|E_T,\eta)} \tag{5.8}$$

$$\epsilon_i^{iso}(m_{ee}^{reco}) = \frac{N_i^{ee}(m_{ee}^{reco}|E_T,\eta,id,iso)}{N_i^{ee}(m_{ee}^{reco}|E_T,\eta,id)} \tag{5.9}$$

$$\epsilon_i^{trig}(m_{ee}^{reco}) = \frac{N_i^{ee}(m_{ee}^{reco}|E_T,\eta,id,iso,trig)}{N_i^{ee}(m_{ee}^{reco}|E_T,\eta,id,iso)}, \tag{5.10}$$

where

- ϵ_i^{id} is the ratio of the number $N_i^{ee}(m_{ee}^{reco}|E_T,\eta,id)$ of reconstructed opposite sign electron pairs passing E_T and η requirements (also excluding the crack region)

and passing the tight identification, to the number $N_i^{ee}(m_{ee}^{reco}|E_T,\eta)$ of opposite sign electron pairs within acceptance.

- ϵ_i^{iso} is the ratio of the number $N_i^{ee}(m_{ee}^{reco}|E_T,\eta,id,iso)$ of reconstructed opposite sign electron pairs within acceptance and passing the tight identification and calorimeter isolation, to the number $N_i^{ee}(m_{ee}^{reco}|E_T,\eta,id)$ of opposite sign electron pairs within acceptance and passing tight identification.

- ϵ_i^{trig} is the ratio of the number $N_i^{ee}(m_{ee}^{reco}|E_T,\eta,id,iso,trig)$ of reconstructed opposite sign electron pairs within acceptance and passing the tight identification, calorimeter isolation, and EF_2e12_medium trigger requirements, to the number $N_i^{ee}(m_{ee}^{reco}|E_T,\eta,id,iso)$ of opposite sign electron pairs within acceptance and passing tight identification and calorimeter isolation.

Substituting Equations (5.8), (5.9), and (5.10) into Equation (5.7) gives a simple expression for the selection efficiency:

$$\epsilon_i^{sel}(m_{ee}^{reco}) = \frac{N_i^{ee}(m_{ee}^{reco}|E_T,\eta,id,iso,trig)}{N_i^{ee}(m_{ee}^{reco}|E_T,\eta)}. \tag{5.11}$$

The selection efficiency will be calculated in this analysis using a method known as tag and probe. (For a preview of tag and probe, see Appendix A).

Taking Equation (5.5) and dividing it by $\epsilon_i^{sel}(m_{ee}^{reco})$ corrects the Drell-Yan distribution for the effects of tight identification, calorimeter isolation, and the event filter trigger. The selection efficiency corrected Drell-Yan distribution as a function of m_{ee}^{reco} is

$$N_i^{DY}(m_{ee}^{reco}|E_T,\eta) \equiv \frac{N_i^{DY}(m_{ee}^{reco}|E_T,\eta,id,iso,trig)}{\epsilon_i^{sel}(m_{ee}^{reco})}. \tag{5.12}$$

5.4 Bayesian Unfolding

The distribution expressed by Equation 5.12 contains detector effects which are studied in this analysis using Monte Carlo. One such detector effect, known as detector resolution, leads to a mismeasurement of the electron energy and position, ultimately leading to migrations of e^+e^- pairs between invariant mass bins. Another effect is the mis-reconstruction of electrons which is quantified by the reconstruction efficiency. Due to technical limitations, the detector fails to correctly reconstruct all true electrons. The reconstruction efficiency can be calculated using the following equation:

$$\epsilon_i^{reco}(m_{ee}^{reco}) = \frac{N_i^{ee}(m_{ee}^{reco}|E_T,\eta,\Delta R)|_{MC}}{N_i^{DY}(m_{ee}^{true}|E_T,\eta)|_{MC}}, \tag{5.13}$$

where $N_i^{DY}(m_{ee}^{true}|E_T,\eta)|_{MC}$ is the number of true Drell-Yan pairs within acceptance and $N_i^{ee}(m_{ee}^{reco}|E_T,\eta,\Delta R)|_{MC}$ is the number of reconstructed pairs within acceptance that match to the aforementioned true pairs with $\Delta R < 0.15$. The main cause of electrons not properly being reconstructed is due to dead material in front of the electromagnetic calorimeter. Electrons will radiate photons as they travel through this material and if a significant portion of their energy is radiated away, they may not be reconstructed.

This analysis uses the technique of iterative Bayesian unfolding [34] to correct for both detector resolution and mis-reconstruction effects. (For more information on Bayesian unfolding, see Appendix B). As stated, the selection efficiency corrected distribution $N_i^{DY}(m_{ee}^{reco}|E_T,\eta)$ is affected by detector resolution and mis-reconstruction effects. Given a matrix $M_{ij} \equiv M_{ij}(m_{ee}^{true}, m_{ee}^{reco})|_{MC}$ (constructed using MC) that maps the entries of the reconstructed invariant mass distribution $N_i^{DY}(m_{ee}^{reco}|E_T,\eta)$ to those of the true invariant mass distribution $N_i^{DY}(m_{ee}^{true}|E_T,\eta)$, the effects of both detector resolution and mis-reconstruction can be corrected for:

$$N_i^{DY}(m_{ee}^{true}|E_T,\eta) = \sum_j M_{ij} N_j^{DY}(m_{ee}^{reco}|E_T,\eta), \quad i,j = 1,2,3,... \tag{5.14}$$

where matrix M_{ij} is known as the response matrix. Note that the Bayesian unfolding method is symbolically represented in Equation (5.14) as a matrix multiplication involving M_{ij} and vector $N_j^{DY}(m_{ee}^{reco}|E_T,\eta)$. The Bayesian method is, however, not a simple matrix multiplication. It is represented in this way so that it may be symbolically incorporated into the equation for the differential Drell-Yan cross section.

5.5 Acceptance

Depending on the energy and direction of the incoming particles, the ATLAS detector may or may not be capable of detecting them. For example, it is difficult to distinguish an electron signature from a photon signature in the electromagnetic calorimeter as they are similar. To make this distinction, both the information from the calorimeter and the inner detector must be used. However, the inner detector covers a region of

$|\eta| < 2.5$ and so the electron is reconstructed only if it travels through a certain part of the detector, in this case the inner detector. This detector limitation is represented by a quantity known as the kinematic acceptance or acceptance. The acceptance for true invariant mass m_{ee}^{true} bin i is defined as

$$A_i(m_{ee}^{true}) = \frac{N_i^{DY}(m_{ee}^{true}|E_T,\eta)|_{MC}}{N_i^{DY}(m_{ee}^{true})|_{MC}}, \quad i = 1,2,3,... \tag{5.15}$$

where $N_i^{DY}(m_{ee}^{true}|E_T,\eta)|_{MC}$ is the number of MC Drell-Yan pairs in m_{ee}^{true} bin i that pass the kinematic selection requirements and $N_i^{DY}(m_{ee}^{true})|_{MC}$ is the total number of MC Drell-Yan pairs in that same bin. The acceptance correction removes the effects the kinematic (E_T and η) cuts have on the measurement. Applying the acceptance correction to Equation (5.14) yields

$$N_i^{DY}(m_{ee}^{true}) = \frac{N_i^{DY}(m_{ee}^{true}|E_T,\eta)}{A_i(m_{ee}^{true})}. \tag{5.16}$$

This is the number of Drell-Yan e^+e^- pairs as a function of true invariant mass. Using the selection efficiency, Bayesian unfolding, and kinematic acceptance, the measured distribution $N^{ee}(m_{ee}^{reco}|E_T,\eta,id,iso,trig)$ has been transformed into $N^{DY}(m_{ee}^{true})$, a quantity comparable to theory.

5.6 Differential Cross Section

Correcting the cross section represented by Equation (5.6) using the selection efficiency, Bayesian unfolding, and the acceptance yields an equation for the Drell-Yan differential cross section in true invariant mass m_{ee}^{true} bin i:

$$\left(\frac{d\sigma^{DY}}{dm_{ee}}\right)_i (m_{ee}^{true}) = \frac{M_{ij}\left[N_j^{DY}(m_{ee}^{reco}|E_T,eta,id,iso,trig)/\epsilon_j^{sel}(m_{ee}^{reco})\right]}{A_i(m_{ee}^{true})\Delta m_{ee,i}^{true}\int \mathcal{L}dt}, \tag{5.17}$$

where $i,j = 1,2,3,....$ Each of the quantities in this equation has been defined. The mathematical formulation developed here is the framework in which this analysis will follow. The following chapters will cover in detail the steps taken to compute these quantities and ultimately the Drell-Yan differential cross section represented by Equation (5.17).

Chapter 6

Measurement and Background Estimation

The measured number of e^+e^- pairs found in the data set is presented in this chapter. Following this is an estimate of the number of background pairs contaminating the measurement. The estimation is made using Monte Carlo samples simulating the background processes. The difference between the measurement and the background estimate is the number of Drell-Yan pairs found in data. Determining this quantity is the first step in computing the Drell-Yan differential cross section.

6.1 Measurement

The measured number of real, isolated electron pairs found in the data set is obtained by applying selection requirements to each of the events. The data set and event selection requirements were stated in Chapter 4. Seen in Figure 6.1 is the measured distribution of electron pairs passing selection requirements as a function of reconstructed invariant mass. The error bars seen in this plot represent the statistical uncertainty. Table 6.1 shows the number of pairs found in each of the invariant mass bins along with the statistical uncertainty. This spectrum is not yet the distribution of Drell-Yan electron pairs because of background contamination. To obtain the Drell-Yan distribution, an estimate of the number of background pairs found in the measured spectra must be quantified and subtracted off.

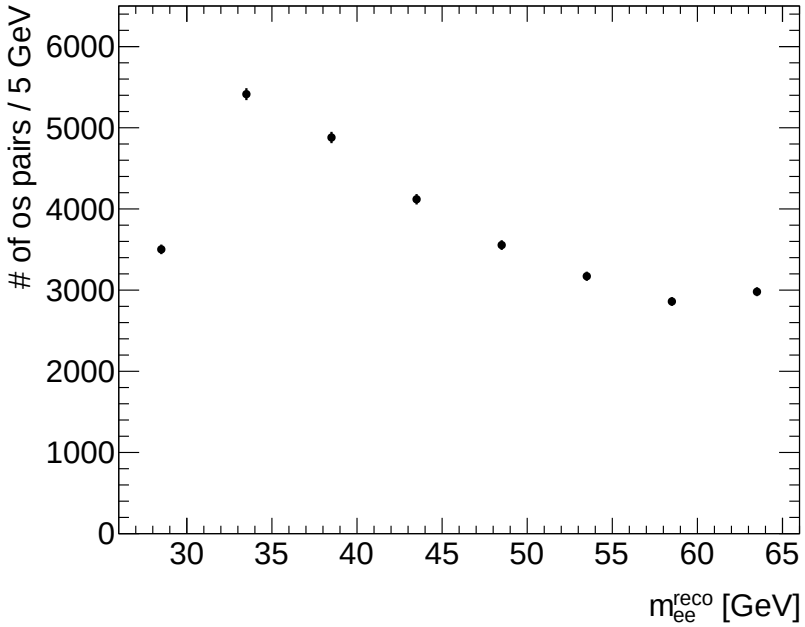

Figure 6.1: The measured distribution as a function of the reconstructed invariant mass. This is the distribution of all opposite sign electron pairs, Drell-Yan and background, passing selection requirements found in the data set.

m_{ee} [GeV]	Measured
26-31	3502 ± 59.2
31-36	5414 ± 73.6
36-41	4880 ± 69.9
41-46	4119 ± 64.2
46-51	3555 ± 59.6
51-56	3171 ± 56.3
56-61	2860 ± 53.5
61-66	2980 ± 54.6

Table 6.1: The number of electron pairs, both Drell-Yan and background, passing event selection and the statistical error.

6.2 Background Estimation

An estimate of the number of background pairs contaminating the measured distribution is obtained using Monte Carlo samples simulating the known background processes to the Drell-Yan process. These background processes, listed in Section 5.2, each have a corresponding Monte Carlo sample listed in Section 4.4. In order to

obtain a simulation of the Drell-Yan process consistent with data, signal MC samples are also used along with background samples. The signal Monte Carlo samples simulate the Drell-Yan process $\gamma^*/Z \to e^+e^-$. By performing event selection on the signal and background samples and summing the number of passed e^+e^- pairs, the results obtained from data are replicated. To illustrate this, distributions of the number of single electrons as functions of reconstructed E_T, η, and ϕ can be seen in Figure 6.2. The black markers represent the number of electrons that remain after applying selection requirements to data while the coloured histograms are the number of electrons in the signal and background MC samples that pass those same cuts. These figures show that there is good agreement between the results obtained using data and Monte Carlo.

Distributions of the number of Drell-Yan electron pairs can be seen in Figure 6.3. They are plotted as functions of reconstructed invariant mass, transverse momentum, and rapidity. Again, the black markers represent data and the coloured histograms are signal and background MC. As was observed for the single electron histograms, these histograms show good agreement between data and Monte Carlo. A table summarizing the invariant mass distributions of the MC samples can be seen in Table 6.2 which shows for each MC sample the number of pairs and the statistical uncertainty.

m_{ee} [GeV]	Signal	$b\bar{b}(c\bar{c})$	$\tau^+\tau^-$	$t\bar{t}$	Diboson
26-31	2867 ± 81.8	330.3 ± 22.5	43.92 ± 6.6	27.8 ± 1.2	5.3 ± 0.4
31-36	4277 ± 100.3	336.8 ± 23.2	134.3 ± 11.7	34.2 ± 1.3	6.6 ± 0.4
36-41	4063 ± 99.7	222.6 ± 19.0	182.4 ± 14.0	38.1 ± 1.3	7.4 ± 0.4
41-46	3450 ± 92.4	115.4 ± 13.5	239.6 ± 16.4	40.6 ± 1.4	7.9 ± 0.4
46-51	2890 ± 83.4	69.6 ± 10.4	259.5 ± 17.1	46.1 ± 1.4	8.9 ± 0.5
51-56	2675 ± 79.4	40.0 ± 8.2	233.3 ± 16.6	45.8 ± 1.5	9.0 ± 0.5
56-61	2643 ± 59.5	25.5 ± 6.4	161.4 ± 13.8	47.2 ± 1.5	9.6 ± 0.5
61-66	2694 ± 32.2	18.6 ± 6.1	121.4 ± 12.4	48.1 ± 1.5	9.8 ± 0.5

Table 6.2: The number of MC e^+e^- pairs passing event selection with the statistical uncertainty as a function of reconstructed invariant mass. These figures were obtained by performing event selection on the analysis MC samples: the signal, $b\bar{b}(c\bar{c})$, $\tau^+\tau^-$, $t\bar{t}$, and diboson.

The agreement between data and Monte Carlo displayed in Figures 6.2 and 6.3 supports the use of MC to estimate the background. Summing the pairs from the $b\bar{b}(c\bar{c})$, $\tau^+\tau^-$, $t\bar{t}$, and diboson samples that pass event selection yields an estimate of the Drell-Yan background. A histogram showing the background spectrum can

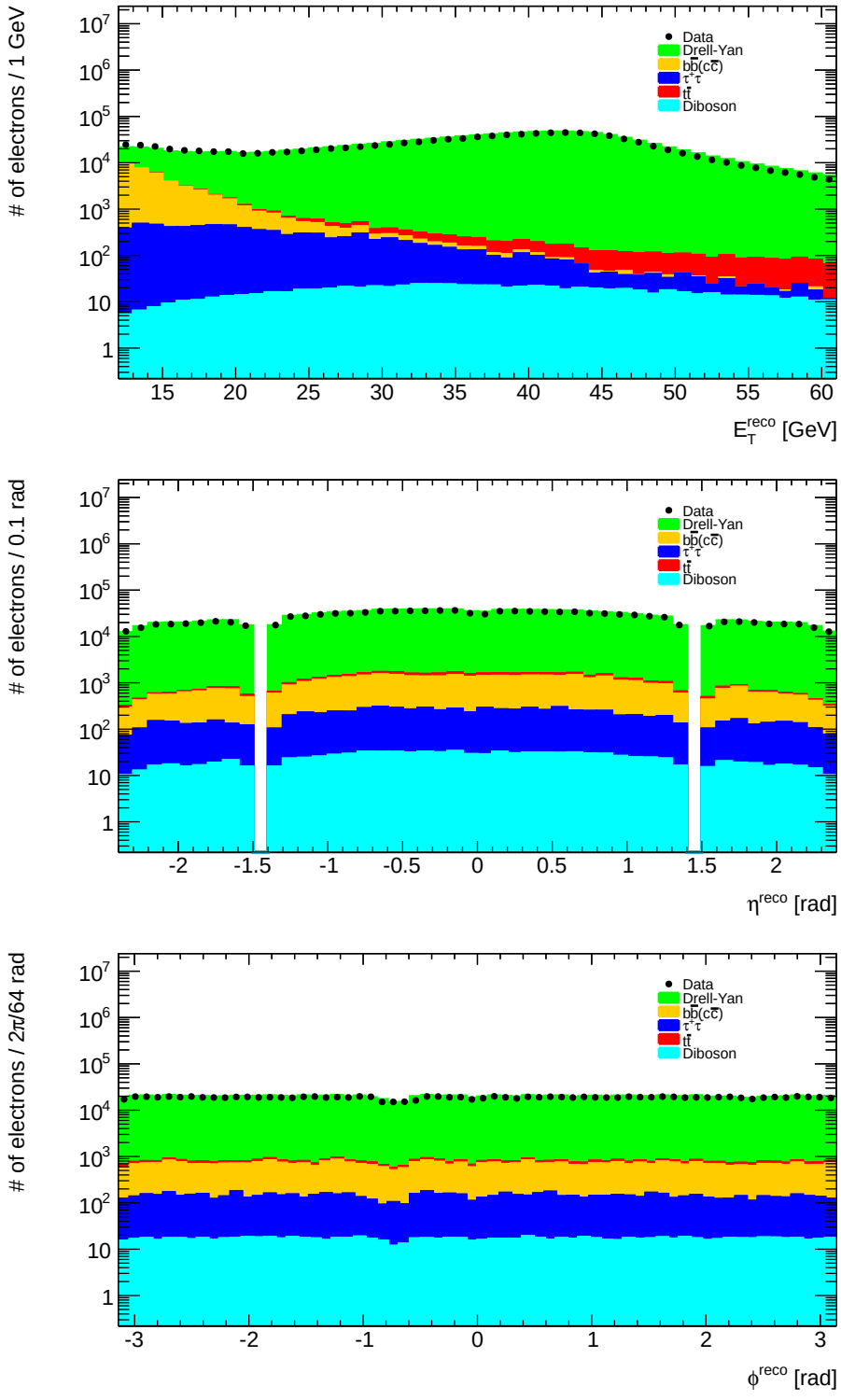

Figure 6.2: Single electron distributions plotted as a function of reconstructed E_T (top), η (middle), and ϕ (bottom). The markers represent data while the histograms represent Drell-Yan or background MC.

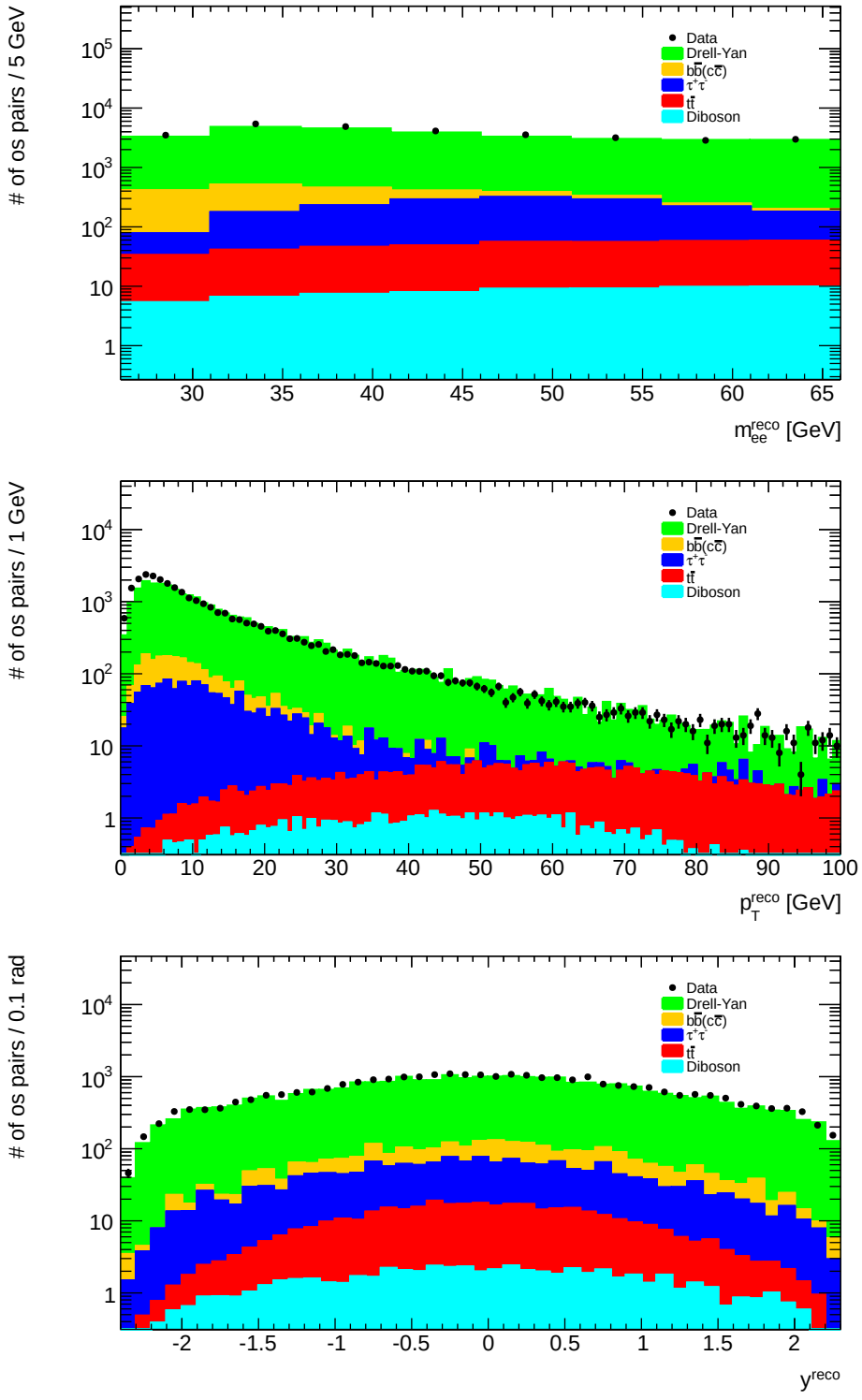

Figure 6.3: Drell-Yan pair distributions plotted as a function of reconstructed m_{ee} (top), p_T (middle), and y (bottom). The markers represent data while the histograms represent Drell-Yan or background MC.

be seen in Figure 6.4 and a table showing the number of background pairs with the statistical uncertainty as a function of reconstructed invariant mass can be seen in Table 6.3.

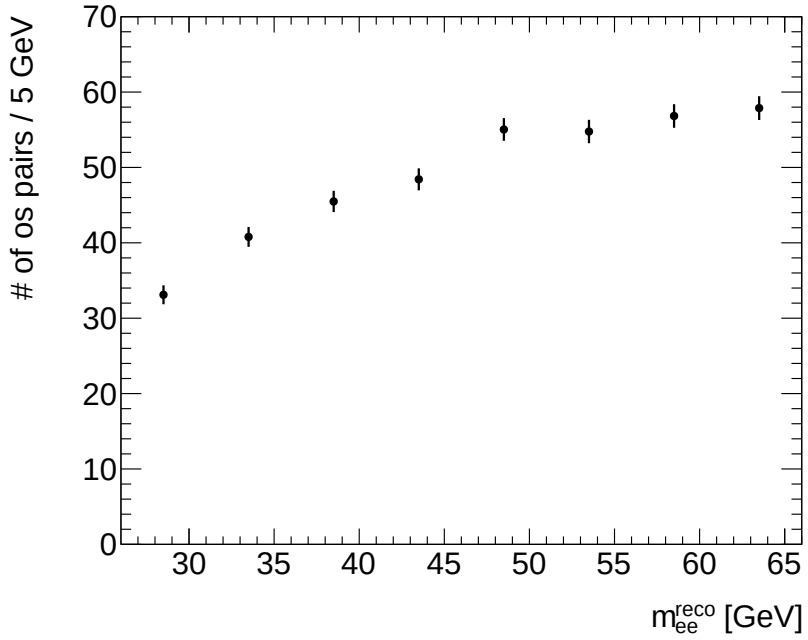

Figure 6.4: Background distribution as a function of reconstructed invariant mass. These are the opposite sign electrons in the background MC samples that pass the analysis selection requirements.

m_{ee} [GeV]	Background
26-31	407.4 ± 23.5
31-36	511.8 ± 26.0
36-41	450.5 ± 23.6
41-46	403.4 ± 21.3
46-51	384.1 ± 20.1
51-56	328.1 ± 18.6
56-61	243.7 ± 15.3
61-66	197.9 ± 13.9

Table 6.3: The number of background electron pairs passing event selection and the statistical uncertainty.

6.3 Background Subtraction

Having determined the quantities shown in Figures 6.1 and 6.4, it is now possible to compute the Drell-Yan distribution $N_i^{DY}(m_{ee}^{reco}|E_T, \eta, id, iso, trig)$. The distribution shown in Figure 6.1 represents the number $N_i^{ee}(m_{ee}^{reco}|E_T, \eta, id, iso, trig)|_{data}$ of final state e^+e^- pairs found in the data set as a function of m_{ee}^{reco}. Subtracting from this quantity the expected number $N_i^{bkg}(m_{ee}^{reco}|E_T, \eta, id, iso, trig)|_{MC}$ of reconstructed background pairs determined using MC yields the number of Drell-Yan pairs in data (Equation (5.5)):

$$N_i^{DY}(m_{ee}^{reco}|E_T, \eta, id, iso, trig)$$
$$= N_i^{ee}(m_{ee}^{reco}|E_T, \eta, id, iso, trig)|_{data} - N_i^{bkg}(m_{ee}^{reco}|E_T, \eta, id, iso, trig)|_{MC}.$$

This distribution is shown in Figure 6.5; the histogram is a graphical representation of the quantity $N_i^{DY}(m_{ee}^{reco}|E_T, \eta, id, iso, trig)$. Table 6.4 summarizes the number of selected opposite sign electron pairs in the data set, background estimation, and resulting Drell-Yan distribution as functions of reconstructed invariant mass.

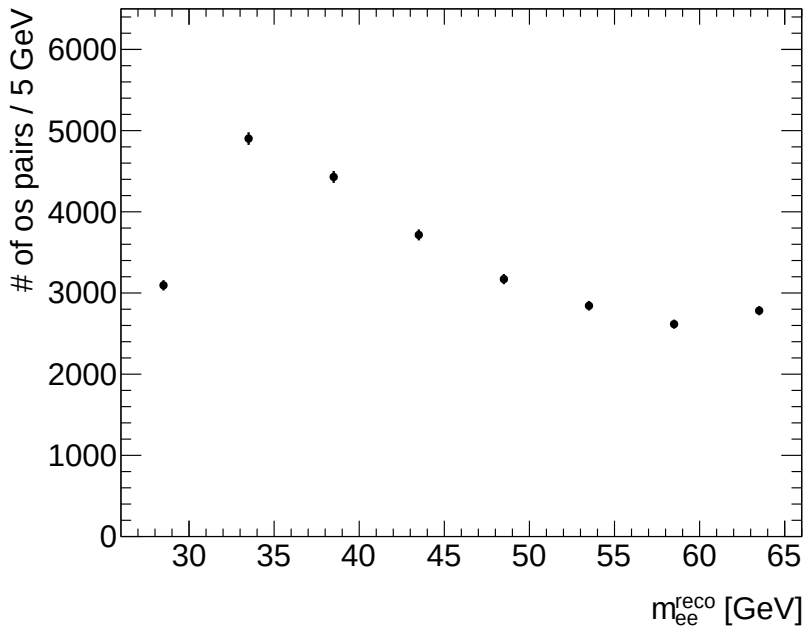

Figure 6.5: Drell-Yan distribution as a function of the reconstructed invariant mass. This distribution is the measured number of e^+e^- pairs passing selection found in data with the expected number of background pairs estimated using MC subtracted.

m_{ee} [GeV]	Measured	Background	Drell-Yan
26-31	3502 ± 59.2	407.4 ± 23.5	3094.6 ± 63.7
31-36	5414 ± 73.6	511.8 ± 26.0	4902.2 ± 78.0
36-41	4880 ± 69.9	450.5 ± 23.6	4429.5 ± 73.7
41-46	4119 ± 64.2	403.4 ± 21.3	3715.6 ± 67.6
46-51	3555 ± 59.6	384.1 ± 20.1	3170.9 ± 62.9
51-56	3171 ± 56.3	328.1 ± 18.6	2842.9 ± 59.3
56-61	2860 ± 53.5	243.7 ± 15.3	2616.3 ± 55.6
61-66	2980 ± 54.6	197.9 ± 13.9	2782.1 ± 56.3

Table 6.4: The number of measured e^+e^-, background, and Drell-Yan pairs passing selection requirements as a function of reconstructed invariant mass. The measured number of e^+e^- pairs was found using data while the background was obtained using Monte Carlo.

In order to obtain a distribution that can be compared to theoretical predictions, $N_i^{DY}(m_{ee}^{reco}|E_T, \eta, id, iso, trig)$ must be corrected using the selection efficiency, iterative Bayesian unfolding, and the acceptance. These quantities are calculated in the following chapter.

Chapter 7

Efficiency, Unfolding, and Acceptance

The measurement of the Drell-Yan distribution is affected by the selection efficiency, detector resolution, reconstruction efficiency, and acceptance. Various techniques including tag and probe, scale factors, iterative Bayesian unfolding are used to quantify these effects thus allowing the measured distribution to be corrected for them. In this chapter, these techniques are introduced and implemented.

7.1 Selection Efficiency

The selection efficiency (Equation (5.11)) as a function of reconstructed invariant mass m_{ee}^{reco} is

$$\epsilon_i^{sel}(m_{ee}^{reco}) = \frac{N_i^{ee}(m_{ee}^{reco}|E_T, \eta, id, iso, trig)}{N_i^{ee}(m_{ee}^{reco}|E_T, \eta)}, \quad i = 1, 2, 3, ...,$$

which can be calculated using either data or MC. This analysis opts to use data to tune the MC such that it shows better agreement with the data. The selection efficiency is then calculated using the corrected Monte Carlo:

$$\epsilon_i^{sel}(m_{ee}^{reco}) = \frac{N_i^{ee}(m_{ee}^{reco}|E_T, \eta, id, iso, trig)|_{MC}}{N_i^{ee}(m_{ee}^{reco}|E_T, \eta)|_{MC}}. \tag{7.1}$$

The following discussion will introduce a data driven technique known as tag and probe [35] which will be used to compute tag and probe efficiencies. (For more information on the tag and probe method, see Appendix A). The tag and probe

efficiencies are then used to determine quantities known as scale factors. These scale factors tune the MC to better reflect the data.

For each of the tight identification, calorimeter isolation, and the trigger requirements made during event selection, there is an associated tag and probe efficiency: ϵ_{tp}^{id}, ϵ_{tp}^{iso}, and ϵ_{tp}^{trig}. The EGamma group [36] provides the tag and probe tight identification efficiency ϵ_{tp}^{id} binned in E_T^{reco} and η^{reco}. The tag and probe isolation and trigger efficiencies are independently computed in this analysis.

The following description is an overview of the tag and probe method. Tag and probe for the process $\gamma^*/Z \to e^+e^-$ requires a data set containing events with exactly one pair of opposite sign electrons. These events are searched for in invariant mass regions around the J/Ψ and Z boson resonances where the production cross section is large. For each event, one electron is required to pass a strict series of requirements to reduce background contamination. Any electron that passes these cuts is known as a tag. The other electron, the probe, is then tested with lenient requirements. The probes are then used to calculate the tag and probe efficiency of interest.

To determine ϵ_{tp}^{iso} and ϵ_{tp}^{trig}, only pairs near the Z boson resonance, from 80 to 100 GeV in invariant mass, are used ensuring a high purity of e^+e^- pairs. Pairs with at least one of the electrons passing the single electron trigger EF_e20_medium are selected and of these, only those with exactly two opposite sign electrons are kept. One of these electrons is tested using the tag selection. The tag must be the electron that triggers EF_e20_medium determined using the TrigMatchTool with a value of $\Delta R < 0.15$ between the tag and the trigger object. It must also satisfy the following requirements:

- $E_T > 12$ GeV
- $|\eta| < 2.4$ (excluding the crack region)
- Tight identification
- Calorimeter isolation.

Electrons that satisfy all these requirements are deemed tags. Having the tag, the probe selection is implemented on the second electron. It must be sufficiently far away from the tag; the tag electron and the probe electron are required to have $\Delta R > 0.8$. It is then required to pass the following:

- $E_T > 12$ GeV

- $|\eta| < 2.4$ (excluding the crack region)
- Tight identification.

The probes are then tested for calorimeter isolation and those that pass are used to compute the tag and probe isolation efficiency, binned in E_T^{reco} and η^{reco}:

$$\epsilon_{tp,i}^{iso}(E_T^{reco}) = \frac{N_i^e(E_T^{reco}|E_T,\eta,id,iso)}{N_i^e(E_T^{reco}|E_T,\eta,id)}, \quad i = 1,2,3,... \tag{7.2}$$

$$\epsilon_{tp,i}^{iso}(\eta^{reco}) = \frac{N_i^e(\eta^{reco}|E_T,\eta,id,iso)}{N_i^e(\eta^{reco}|E_T,\eta,id)}, \quad i = 1,2,3,..., \tag{7.3}$$

where $N_i^e(E_T^{reco}|E_T,\eta,id)$ is the number of probes that pass E_T, η, and tight requirements found in E_T^{reco} bin i and $N_i^e(E_T^{reco}|E_T,\eta,id,iso)$ is the number of probes that pass E_T, η, tight, and isolation requirements found in E_T^{reco} bin i. The tag and probe isolation efficiency binned in η^{reco} is similar. The tag and probe isolation efficiency as a function of E_T^{reco} and η^{reco} can be seen in Figure 7.1. The black markers represent data and the red markers represent MC. As expected, there are differences between results obtained using data and MC. The discrepancies are due to mis-modelling of the MC.

Having tested the probes for calorimeter isolation, they are then tested for the single electron trigger EF_e12_medium[1] and those that pass are used to compute ϵ_{tp}^{trig}. Binned in E_T^{reco} and η^{reco}, the tag and probe trigger efficiency is

$$\epsilon_{tp,i}^{trig}(E_T^{reco}) = \frac{N_i^e(E_T^{reco}|E_T,\eta,id,iso,trig)}{N_i^e(E_T^{reco}|E_T,\eta,id,iso)}, \quad i = 1,2,3,... \tag{7.4}$$

$$\epsilon_{tp,i}^{trig}(\eta^{reco}) = \frac{N_i^e(\eta^{reco}|E_T,\eta,id,iso,trig)}{N_i^e(\eta^{reco}|E_T,\eta,id,iso)}, \quad i = 1,2,3,... \tag{7.5}$$

This efficiency can be seen in Figure 7.2, again as a function of E_T^{reco} and η^{reco} for both data and MC.

Having all the necessary tag and probe efficiencies, the scale factors can now be computed. The tight identification scale factors are supplied by the EGamma group while the isolation and trigger scale factors are calculated as a part of this analysis.

[1]Note the difference between this single electron trigger and the di-electron trigger EF_2e12_medium.

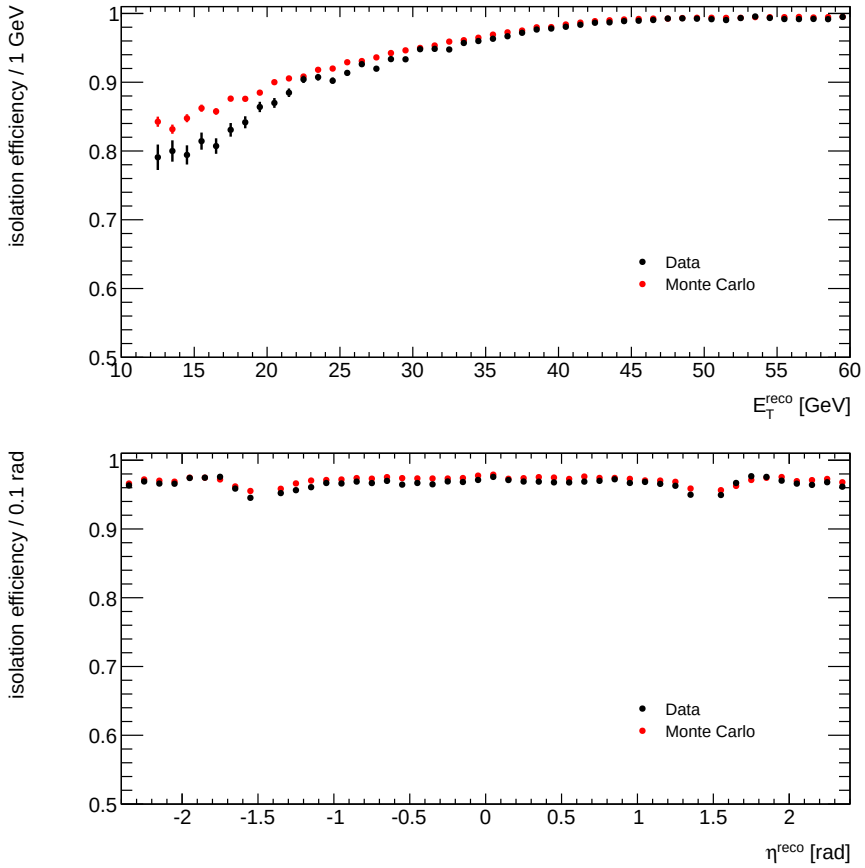

Figure 7.1: Tag and probe isolation efficiency as a function of E_T^{reco} (top) and η^{reco} (bottom) for both data and Monte Carlo. The differences in the data results and the MC results are due to mis-modelling of the MC.

They are defined as the ratios of the tag and probe efficiencies found in data to the tag and probe efficiencies found in Monte Carlo:

$$s_{jk}^{iso}(\eta^{reco}, E_T^{reco}) = \frac{\epsilon_{tp,jk}^{iso}(\eta^{reco}, E_T^{reco})|_{data}}{\epsilon_{tp,jk}^{iso}(\eta^{reco}, E_T^{reco})|_{MC}}, \quad j,k = 1,2,3,... \tag{7.6}$$

$$s_{jk}^{trig}(\eta^{reco}, E_T^{reco}) = \frac{\epsilon_{tp,jk}^{trig}(\eta^{reco}, E_T^{reco})|_{data}}{\epsilon_{tp,jk}^{trig}(\eta^{reco}, E_T^{reco})|_{MC}}, \quad j,k = 1,2,3,..., \tag{7.7}$$

where s_{jk} is the scale factor for η^{reco} bin j and E_T^{reco} bin k. Here $\epsilon_{tp,jk}(\eta^{reco}, E_T^{reco})|_{data}$ is the tag and probe efficiency in two-dimensional bin j,k determined using data and $\epsilon_{tp,jk}(\eta^{reco}, E_T^{reco})|_{MC}$ is the tag and probe efficiency in the two-dimensional bin j,k determined using MC. Performing these calculations produces the scale factors seen

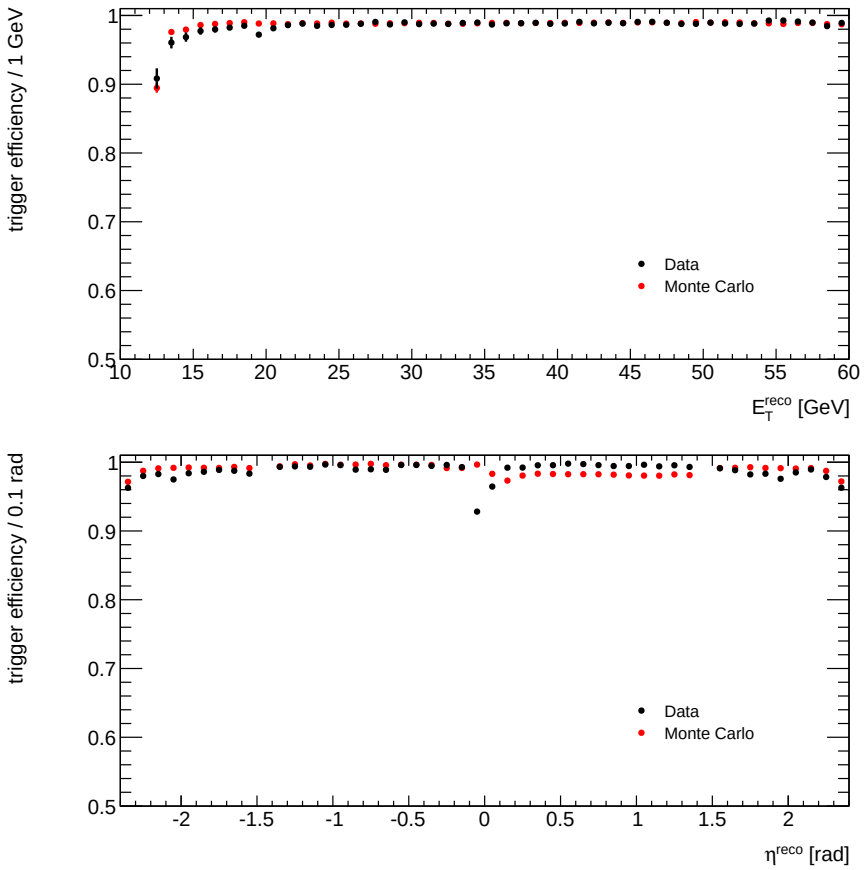

Figure 7.2: Tag and probe trigger efficiency as a function of E_T^{reco} (top) and η^{reco} (bottom) for both data and Monte Carlo. The differences in the data results and the MC results are due to mis-modelling of the MC.

in Figure 7.3 [33].

To illustrate how the scale factors are used to correct Monte Carlo events to better reflect data, consider an MC event that consists of a virtual photon or Z boson decaying into an opposite sign electron pair. Suppose that the electron has reconstructed transverse energy $E_{T,1}^{reco}$ and reconstructed pseudorapidity η_1^{reco} and thus has associated scale factors $s^{id}(E_{T,1}^{reco}, \eta_1^{reco})$, $s^{iso}(E_{T,1}^{reco}, \eta_1^{reco})$, and $s^{trig}(E_{T,1}^{reco}, \eta_1^{reco})$. Suppose also that the positron has $E_{T,2}^{reco}$ and η_2^{reco} and therefore has associated scale factors $s^{id}(E_{T,2}^{reco}, \eta_2^{reco})$, $s^{iso}(E_{T,2}^{reco}, \eta_2^{reco})$, and $s^{trig}(E_{T,2}^{reco}, \eta_2^{reco})$. The MC event has an overall scale factor defined to be

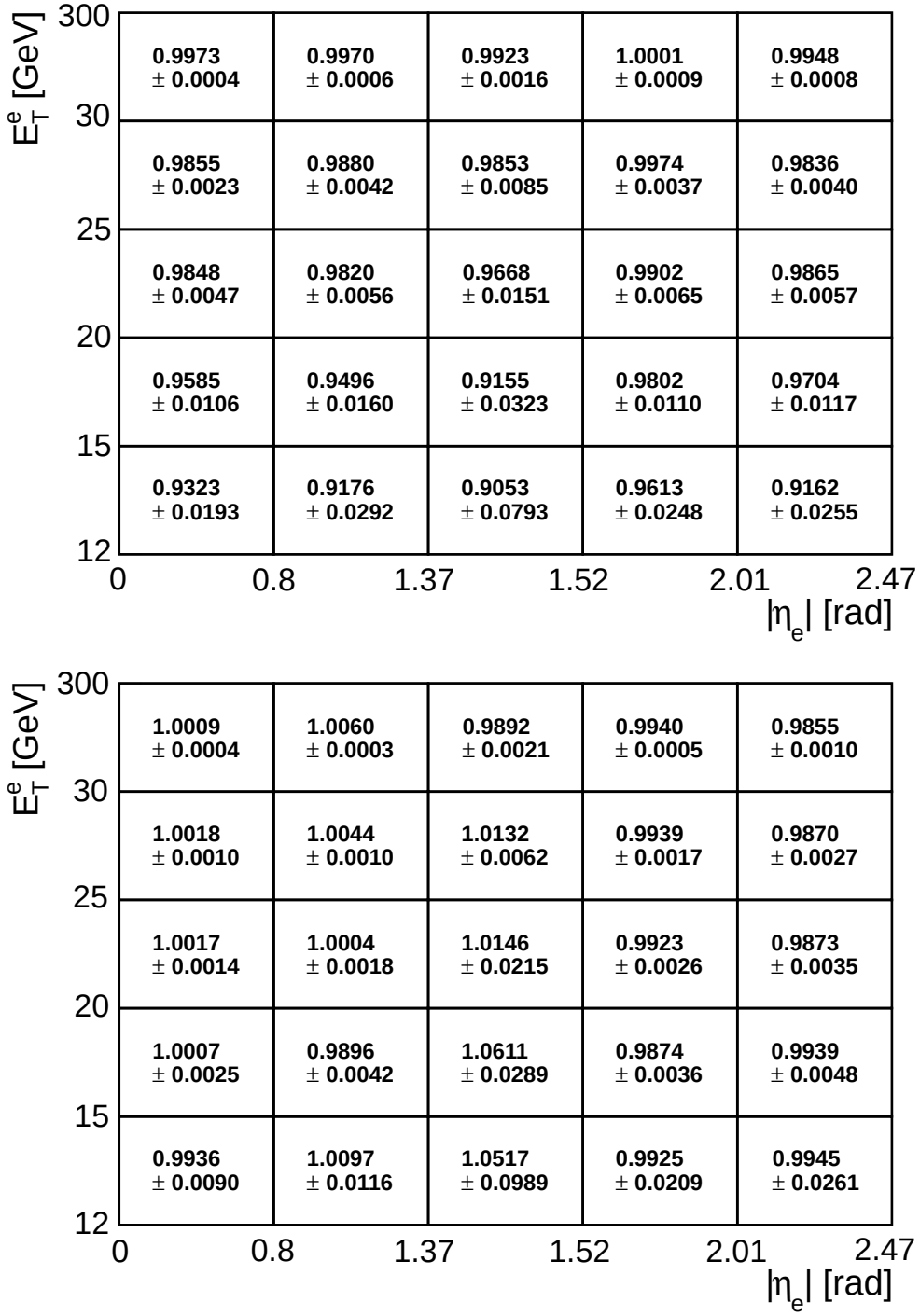

Figure 7.3: Scale factors binned in η from $[0, 0.8, 1.37, 1.52, 2.01, 2.47]$ rad and E_T from $[12, 15, 20, 25, 30, 300]$ GeV. Above are the calorimeter isolation scale factors and below are the EF_e12_medium trigger scale factors.

$$s(E_{T,1}^{reco}, \eta_1^{reco}, E_{T,2}^{reco}, \eta_2^{reco}) = s^{id}(E_{T,1}^{reco}, \eta_1^{reco}) s^{iso}(E_{T,1}^{reco}, \eta_1^{reco}) s^{trig}(E_{T,1}^{reco}, \eta_1^{reco}) \times s^{id}(E_{T,2}^{reco}, \eta_2^{reco}) s^{iso}(E_{T,2}^{reco}, \eta_2^{reco}) s^{trig}(E_{T,2}^{reco}, \eta_2^{reco}). \quad (7.8)$$

This event is then weighted by the overall scale factor $s(E_{T,1}^{reco}, \eta_1^{reco}, E_{T,2}^{reco}, \eta_2^{reco})$ which effectively corrects the MC selection efficiency to correspond to the selection efficiency in data for this event. Doing this for all events corrects the entire MC sample. Take, for example, the number of e^+e^- pairs passing the analysis selection requirements found in MC:

$$N_i^{ee}(m_{ee}^{reco} | E_T, \eta, id, iso, trig)|_{MC} = \beta, \quad (7.9)$$

where β is the integer number of e^+e^- pairs found in m_{ee}^{reco} bin i. The act of weighting MC events by scale factors corresponds to the following change in Equation (7.9):

$$N_i^{ee}(m_{ee}^{reco} | E_T, \eta, id, iso, trig)|_{MC} = \sum_{pairs}^{\beta} s(E_{T,1}^{reco}, \eta_1^{reco}, E_{T,2}^{reco}, \eta_2^{reco}). \quad (7.10)$$

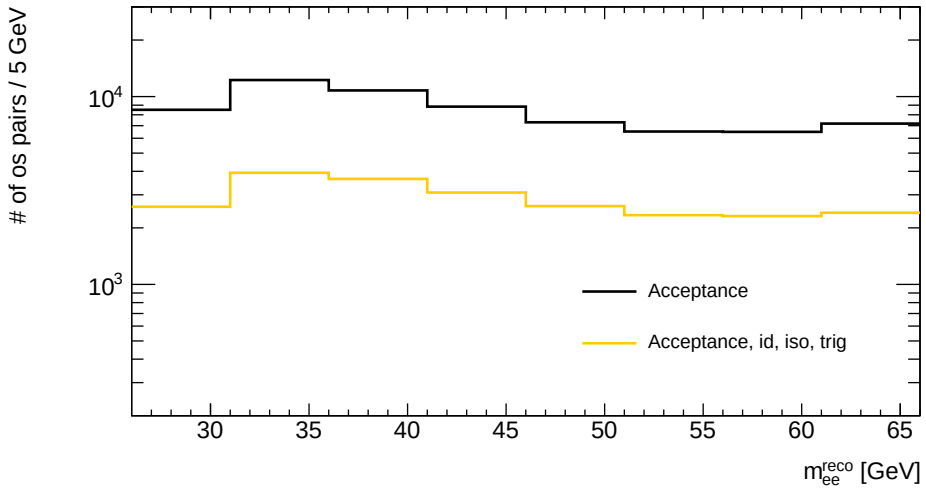

Figure 7.4: Invariant mass distributions used in the calculation of the selection efficiency. The black curve represents the number of opposite sign electron pairs within the acceptance while the orange curve represents the opposite sign pairs that pass all analysis requirements. Their ratio yields the selection efficiency. These distributions were computed using Monte Carlo.

With the scale factors, the selection efficiency on data can be accurately estimated using Monte Carlo. The samples used are the Drell-Yan ones listed in Table 4.2. As shown in Equation (7.1), calculating the selection efficiency requires two quantities, the distribution $N^{ee}(m_{ee}^{reco}|E_T, \eta, id, iso, trig)|_{MC}$ of opposite sign electron pairs passing analysis requirements and the distribution $N^{ee}(m_{ee}^{reco}|E_T, \eta)|_{MC}$ of opposite sign pairs that are within the acceptance. These two histograms can be seen in Figure 7.4. Taking their ratio yields the selection efficiency. Shown in Figure 7.5 are the selection efficiencies computed using the unscaled Monte Carlo (represented by the red markers) and using the Monte Carlo scaled by the factors derived above (represented by the black markers) with their respective binomial errors. The efficiency curve represented by the black markers is the desired selection efficiency which will be referred to as the selection efficiency hereafter. A table showing its values with its statistical uncertainty σ_{ϵ}^{stat} can be seen in Table 7.1.

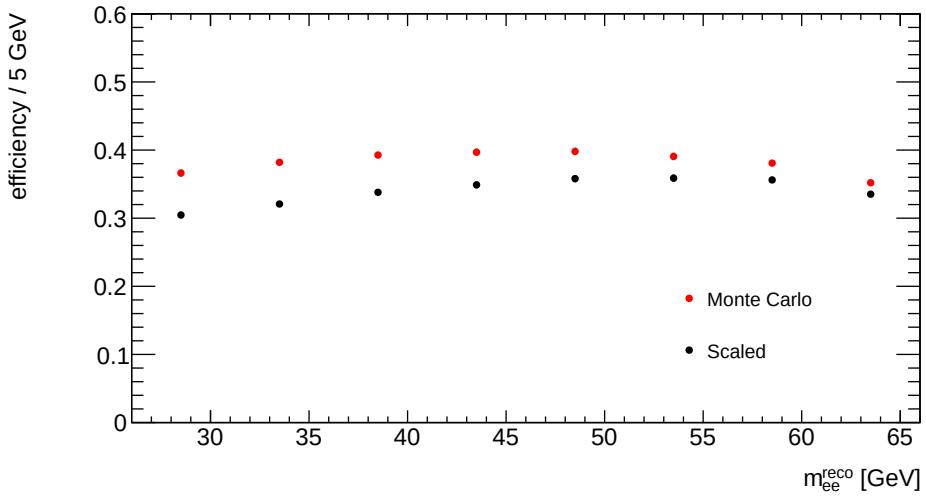

Figure 7.5: The selection efficiency. The red markers represent the MC selection efficiency while the black markers represent the selection efficiency obtained by scaling MC events using the scale factors.

Note that the MC selection efficiency is higher than the selection efficiency. This is because the scale factors in most of the two-dimensional bins are less than unity. The selection efficiency starts low in the first few invariant mass bins and steadily increases. This is because most of the low E_T electrons, which have lower efficiency, are found in the lower m_{ee} regions. Near the highest invariant mass bins, the selection efficiency slightly drops and this is due to resolution effects which cause electron pairs from the Z peak to migrate to the [61,66] GeV invariant mass bin. These e^+e^- pairs

m_{ee} [GeV]	ϵ	σ_{ϵ}^{stat} [%]
26-31	0.305	1.56
31-36	0.321	1.25
36-41	0.338	1.29
41-46	0.349	1.39
46-51	0.358	1.47
51-56	0.359	1.47
56-61	0.356	1.10
61-66	0.335	0.61

Table 7.1: Efficiency results. The selection efficiency figures are given along with their statistical uncertainties σ_{ϵ}^{stat}.

are energetic and hence will likely emit a large amount of radiation. This radiation causes many of the electron pairs to fail tight identification or calorimeter isolation, ultimately lowering the selection efficiency in this bin.

7.2 Resolution and Reconstruction

Detector resolution and mis-reconstruction of electrons cause the true Drell-Yan invariant mass distribution to be different from the reconstructed distribution with the selection efficiency correction:

$$N_i^{DY}(m_{ee}^{true}|E_T,\eta) \neq N_l^{DY}(m_{ee}^{reco}|E_T,\eta) \equiv \frac{N_i^{DY}(m_{ee}^{reco}|E_T,\eta,id,iso,trig)}{\epsilon_i^{sel}(m_{ee}^{reco})}. \quad (7.11)$$

The difference between these two quantities is due to detector resolution and mis-reconstruction effects, both of which can be reversed, or unfolded, using a technique known as iterative Bayesian unfolding. The RooUnfold package [37] is used in this analysis to implement iterative Bayesian unfolding.

To illustrate the effects of detector resolution, Figure 7.6 shows three m_{ee}^{reco} distributions of Drell-Yan pairs. The blue curve represents the distribution of pairs that have a true invariant mass m_{ee}^{true} of 20 GeV, and similarly the red and orange curves represent the pairs that have m_{ee}^{true} equal to 40 and 60 GeV, respectively. All three distributions are normalized to unity and centred about the origin. This figure shows the general trend detector resolution has on the Drell-Yan electron pairs. Pairs with

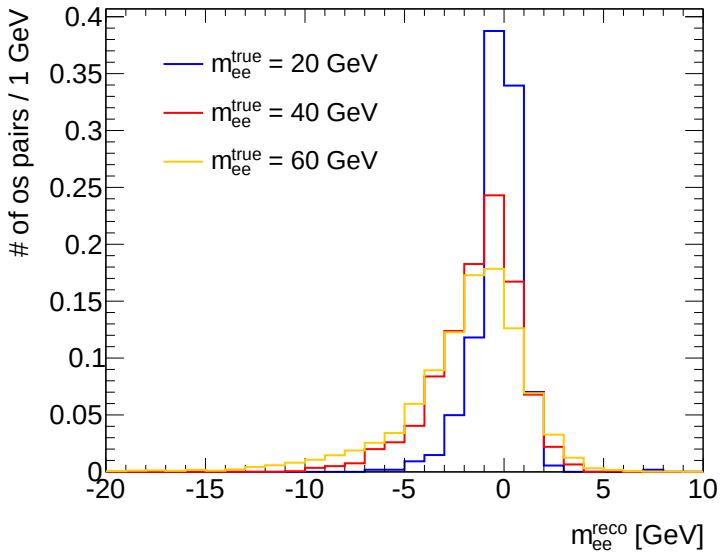

Figure 7.6: Normalized distributions of true 20, 40, and 60 GeV Drell-Yan pairs reconstructed and centred about the origin. These histograms illustrate the effect detector resolution has on the true electron pairs.

smaller true invariant mass are smeared less, while those with larger true invariant masses undergo a larger degree of smearing. In all cases, the smearing creates an asymmetric tail extending towards the lower invariant mass range. This asymmetry is due to bremsstrahlung from electrons because of dead material in front of the calorimeters.

The use of RooUnfold's iterative Bayesian method requires three input parameters, all of which are computed using the Drell-Yan Monte Carlo samples. Prior to calculating these input parameters, the signal MC samples are weighted using reconstruction efficiency scale factors (provided by the EGamma group). The implementation of these scale factors is the same as the tight, isolation, and trigger scale factors. The reconstruction efficiency scale factors weight Monte Carlo electrons such that the reconstruction efficiency in MC matches that found in data.

The first of the three parameters required to use RooUnfold is a response matrix $M_{ij}(m_{ee}^{true}, m_{ee}^{reco})$. The response matrix is a mapping of the reconstructed Drell-Yan pairs, which are affected by resolution effects, to their true counterparts. In Figure 7.7, the response matrix is shown. The rows correspond to true invariant mass m_{ee}^{true} bins and the columns correspond to reconstructed invariant mass m_{ee}^{reco} bins. The matrix is constructed by taking the true Drell-Yan pairs in an m_{ee}^{true} bin and reconstructing

them, thereby applying resolution and reconstruction effects to them. This smears the true pairs found in a single m_{ee}^{true} bin over several m_{ee}^{reco} bins. This process is done for all m_{ee}^{true} bins within the invariant mass range, $25 < m_{ee} < 66$. In general, due to reconstruction effects, the number of true Drell-Yan pairs found in m_{ee}^{true} bin i does not equal the number of pairs reconstructed from these true pairs:

$$N_i^{DY}(m_{ee}^{true}|E_T,\eta) \neq \sum_j M_{ij}(m_{ee}^{true}, m_{ee}^{reco}). \tag{7.12}$$

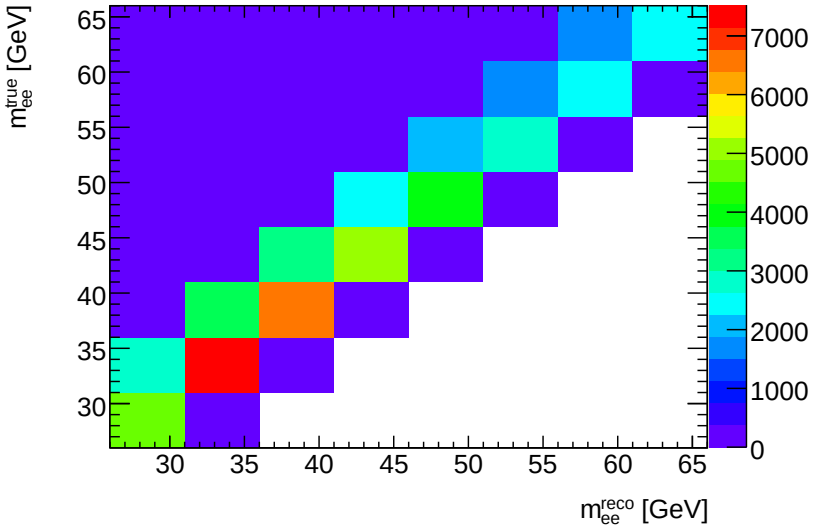

Figure 7.7: The response matrix used in the Bayesian unfolding method. The rows of this matrix corresponds to the true invariant mass and the columns correspond to the reconstructed invariant mass. The asymmetry of this matrix is due to detector resolution.

In addition to a smearing matrix, RooUnfold requires two training histograms both of which are produced using Monte Carlo. One of these training histograms must resemble the measured distribution found in data. This histogram can be seen in Figure 7.8, represented by the orange histogram. The measured distribution is unfolded to resemble whatever form the second training histogram takes. The desired distribution after unfolding is the distribution of true Drell-Yan pairs within acceptance now including the crack region which can be seen in Figure 7.8 represented by the black histogram.

With these input parameters, RooUnfold's iterative Bayesian unfolding method is used to unfold the distribution $N_i^{DY}(m_{ee}^{reco}|E_T,\eta,id,iso,trig)/\epsilon_i^{sel}(m_{ee}^{reco})$. The re-

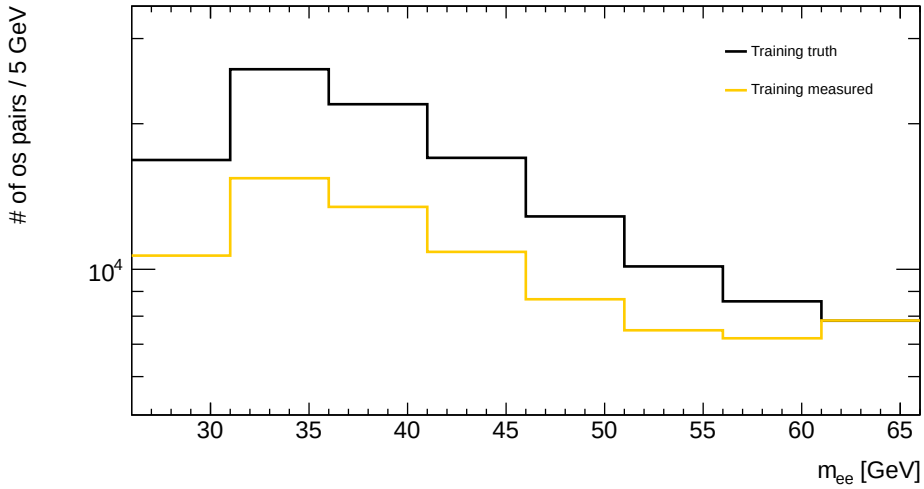

Figure 7.8: The distributions used as training for the Bayesian method. The orange distribution represent the MC distribution simulating the measured data while the black histogram represents the true MC distribution void of detector effects.

sultant distribution is $N^{DY}(m_{ee}^{true}|E_T,\eta)$, the number of true Drell-Yan pairs within the acceptance. This distribution is comparable to theory, but does not represent the most general distribution which is $N^{DY}(m_{ee}^{true})$. In order to obtain this, the acceptance must be determined.

7.3 Acceptance

In this analysis, electron pairs having $E_T > 12$ GeV with at least one electron having $E_T > 15$ GeV and both within $|\eta| < 2.4$ are considered within acceptance. The acceptance A (Equation 5.15) of a Drell-Yan electron pair is

$$A_i(m_{ee}^{true}) = \frac{N_i^{DY}(m_{ee}^{true}|E_T,\eta)|_{MC}}{N_i^{DY}(m_{ee}^{true})|_{MC}}, \quad i = 1,2,3,...,$$

where $N_i^{DY}(m_{ee}^{true}|E_T,\eta)|_{MC}$ is the number of true Drell-Yan electron pairs passing E_T and η requirements in true invariant mass m_{ee}^{true} bin i found in MC and $N_i^{DY}(m_{ee}^{true})|_{MC}$ is the total number of MC Drell-Yan pairs in that bin. The acceptance is a measure of the fraction of Drell-Yan electron pairs that remain after applying kinematic cuts.

The acceptance is calculated using events generated with the central PDF set of MSTW08nlo68cl [8]. Using PYTHIA, four million Drell-Yan events at 7 TeV centre of mass energy and within invariant mass range $20 < m_{ee} < 75$ GeV are generated.

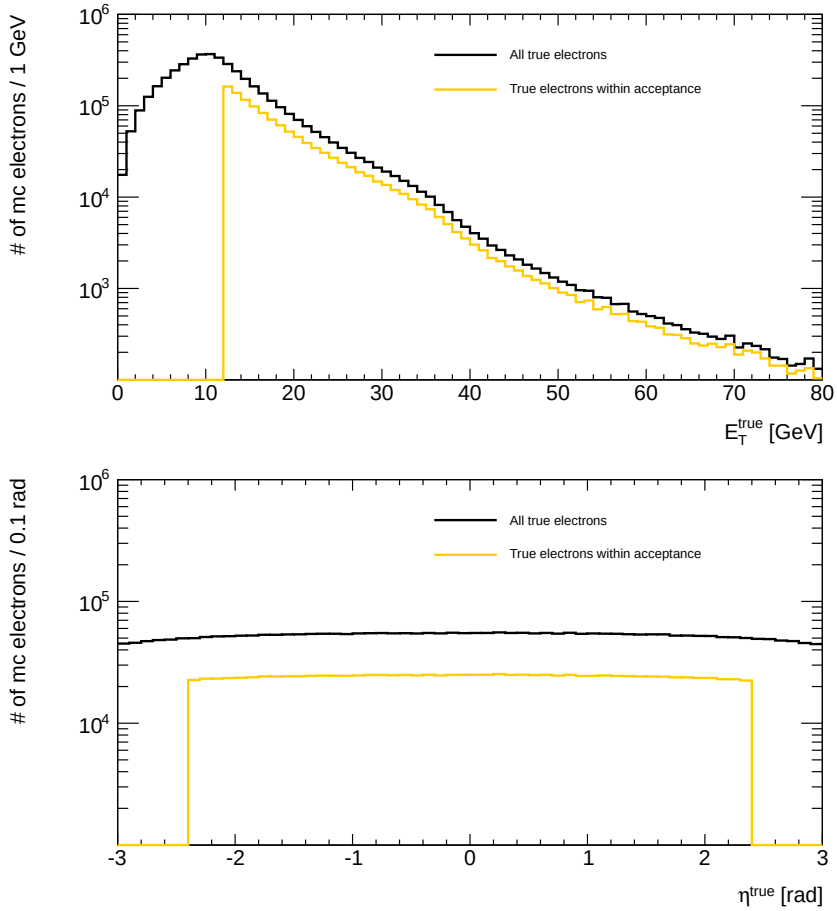

Figure 7.9: Electrons distributions before (black) and after (orange) kinematic cuts. The top figure is a plot of the electron E_T while the bottom figure is a plot of the electron η.

m_{ee} [GeV]	A	σ_A^{stat} [%]
26-31	0.067	0.41
31-36	0.204	0.29
36-41	0.281	0.30
41-46	0.332	0.33
46-51	0.368	0.37
51-56	0.395	0.41
56-61	0.421	0.44
61-66	0.440	0.45

Table 7.2: Acceptance results. The acceptance values are given with their statistical uncertainties σ_A^{stat}.

The kinematic (E_T and η) cuts are then applied to these pairs. Distributions of true electrons can be seen in Figure 7.9 as a function of E_T^{true} and η^{true}. The black curve represents all true electrons and the orange, true electrons that are within acceptance.

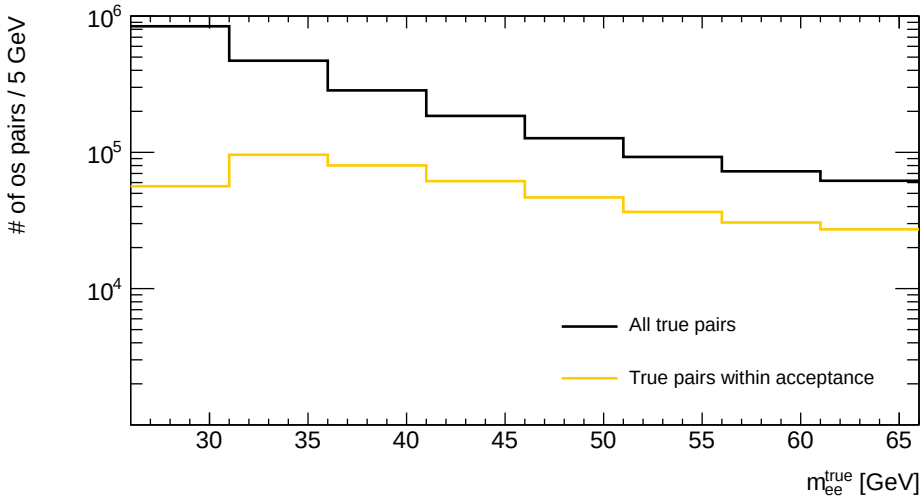

Figure 7.10: Invariant mass distributions used in the calculation of the acceptance. The orange curve represents the number of Drell-Yan pairs within the acceptance while the black curve represents all Drell-Yan pairs. Their ratio yields the acceptance.

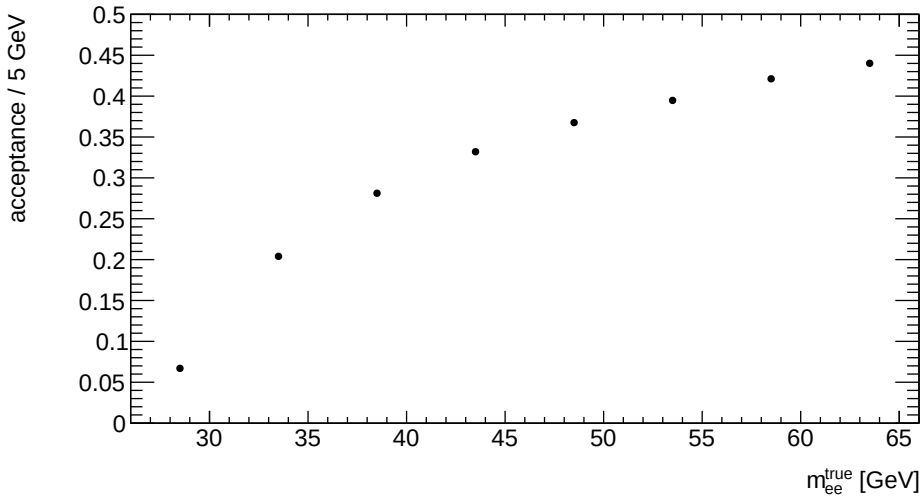

Figure 7.11: The acceptance as a function of true invariant mass.

Computing the invariant mass of all true Drell-Yan pairs within acceptance yields the numerator $N_i^{DY}(m_{ee}^{true}|E_T, \eta)$ in Equation (5.15). Taking this number and dividing by the total number $N_i^{DY}(m_{ee}^{true})$ of true Drell-Yan pairs results in the acceptance.

These histograms can be seen in Figure 7.10 and the resultant acceptance with its binomial statistical uncertainty can be seen in Figure 7.11. A table listing the acceptance values and its statistical uncertainty σ_A^{stat} can be seen in Table 7.2. For the lowest true invariant mass m_{ee}^{true} bin $[26, 31]$ GeV, the acceptance is at its lowest, nearly 6%. It steadily rises, reaching a value of about 45% in the highest invariant mass bin $[61, 66]$ GeV.

Chapter 8

Systematic Uncertainties

Each of the techniques used in this analysis introduces a systematic uncertainty to the measurement. Systematic uncertainties on the Monte Carlo estimate of the heavy quark background, selection efficiency, iterative Bayesian method, and acceptance are computed in this chapter. The uncertainty due to the use of Monte Carlo is estimated by loosening the identification requirement on electrons. The systematic uncertainty on the selection efficiency is computed using the uncertainties on the scale factors. The systematic uncertainty on the Bayesian method is estimated by running pseudo-experiments and using reconstruction efficiency scale factor uncertainties. The systematic error on the acceptance is estimated by using PDF error sets.

8.1 Monte Carlo Uncertainty

In order to determine the systematic uncertainty due to the use of MC for estimating the background from the heavy quarks, the following analysis is performed on the $b\bar{b}(c\bar{c})$ and $t\bar{t}$ MC samples. The electron identification criterion is changed from EGamma tight to medium (introduced in Section 4.6) while all other selection requirements are left unchanged. The use of medium identification leads to a larger number of jets being misidentified as electrons. The invariant mass spectra of the heavy quark MC samples can be seen in Figure 8.1. This figure shows the heavy quark distributions $N^{HQ}(m_{ee}^{reco}|E_T, \eta, tight, iso, trig)|_{MC}$ and $N^{HQ}(m_{ee}^{reco}|E_T, \eta, med, iso, trig)|_{MC}$ calculated using the original tight identification and medium identification, respectively. The subscript HQ indicates either the $b\bar{b}(c\bar{c})$ sample or the $t\bar{t}$ sample.
The systematic uncertainty in each invariant mass bin due to the heavy quark MC

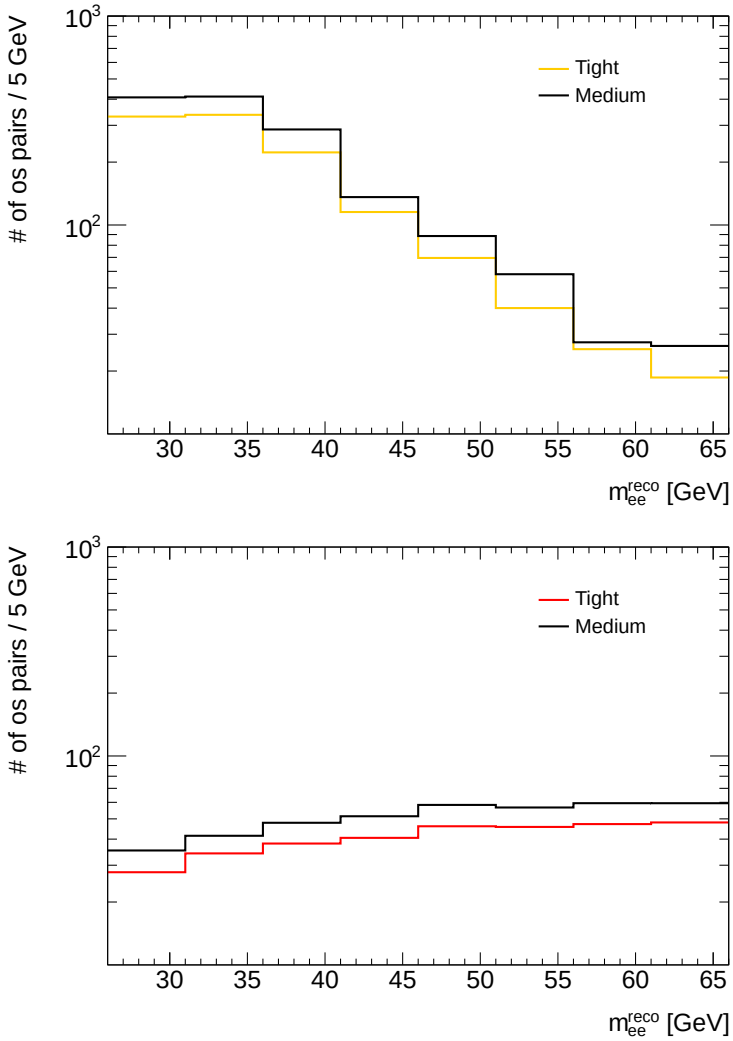

Figure 8.1: Invariant mass distributions of the heavy quark Monte Carlo samples. These spectra were constructed using EGamma tight (represented by the coloured histogram) and medium (represented by the solid black curve) identifications. On top are the $b\bar{b}(c\bar{c})$ spectra and below are the $t\bar{t}$ spectra.

samples is then taken to be

$$\sigma_{HQ}^{sys} = |N^{HQ}(m_{ee}^{reco}|E_T, \eta, tight, iso, trig) - N^{HQ}(m_{ee}^{reco}|E_T, \eta, med, iso, trig)|. \quad (8.1)$$

The results of this background analysis are displayed in Table 8.1. The total uncertainty is the contribution $\sigma_{b\bar{b}(c\bar{c})}^{sys}$ from the $b\bar{b}(c\bar{c})$ sample and the contribution $\sigma_{t\bar{t}}^{sys}$

from the $t\bar{t}$ sample added in quadrature. A table showing the Drell-Yan (background subtracted) distribution along with the systematic uncertainty σ_{HQ}^{sys} can be seen in Table 8.2.

m_{ee} [GeV]	$b\bar{b}(c\bar{c})_{tight}$	$b\bar{b}(c\bar{c})_{med}$	$\sigma_{b\bar{b}(c\bar{c})}^{sys}$	$t\bar{t}_{tight}$	$t\bar{t}_{med}$	$\sigma_{t\bar{t}}^{sys}$
26-31	330.3	408.1	77.8	27.8	35.3	7.5
31-36	336.8	411.8	75.1	34.2	41.5	7.3
36-41	222.6	286.6	64.0	38.1	47.9	9.8
41-46	115.4	136.0	20.6	40.6	51.5	10.9
46-51	69.55	88.6	19.0	46.1	58.3	12.2
51-56	40.03	58.1	18.1	45.8	56.7	10.9
56-61	25.45	27.5	2.0	47.2	59.4	12.2
61-66	18.62	26.4	7.7	48.1	59.4	11.4

Table 8.1: Heavy quark systematics results. For the $b\bar{b}(c\bar{c})$ and $t\bar{t}$ samples, the number of background pairs is given for both tight and medium identifications. The systematic uncertainty σ_{HQ}^{sys} on the Drell-Yan distribution due to use of heavy quark MC is also shown.

m_{ee} [GeV]	Drell-Yan	σ_{HQ}^{sys}
26-31	3095	82.6
31-36	4902	82.5
36-41	4429	74.5
41-46	3716	45.5
46-51	3171	49.8
51-56	2843	49.2
56-61	2616	47.3
61-66	2782	48.7

Table 8.2: Systematic uncertainty on the Drell-Yan distribution due to the heavy quark MC. The individual uncertainties coming from the $b\bar{b}(\ c\bar{c})$ and $t\bar{t}$ samples have been added in quadrature.

8.2 Selection Efficiency Uncertainty

This analysis uses scale factors to weight Monte Carlo events which are then used to compute the selection efficiency. In particular, three independent scale factors are used: tight identification, calorimeter isolation, and EF_e12_medium scale factors

denoted by s^{id}, s^{iso}, and s^{trig}, respectively. Inherent to each of these scale factors is an uncertainty represented by δs^{id}, δs^{iso}, or δs^{trig}. The uncertainties on the scale factors ultimately lead to the systematic uncertainty on the selection efficiency. To estimate the systematic uncertainty on the selection efficiency, consider the total scale factor given by

$$s = s^{id} s^{iso} s^{trig}. \tag{8.2}$$

One of s^{id}, s^{iso}, or s^{trig} is then shifted by adding or subtracting its scale factor uncertainty, while leaving the other two scale factors unchanged. For example, performing this action on the identification scale factor yields two new independent scale factors:

$$s_{\pm 00} = (s^{id} \pm \delta s^{id}) s^{iso} s^{trig}, \tag{8.3}$$

where the subscript ± 00 shown in Equation (8.3) denotes that the tight scale factor was shifted by $\pm$ its uncertainty and the isolation and trigger scale factors were left unchanged. As another example, 0 ± 0 would indicate that the isolation scale factor was shifted by $\pm$ its error, while the tight and trigger scale factors were unchanged.

Performing this shift for each of the three scale factors gives six new ones, seven in total when including the original or nominal scale factor s_{000}. Each of these seven scale factors leads to its own selection efficiency: $\epsilon^{sel}_{\pm 00}$, $\epsilon^{sel}_{0\pm 0}$, $\epsilon^{sel}_{00\pm}$, and ϵ^{sel}_{000}. These seven efficiency curves can be seen in Figure 8.2.

The individual contributions to the systematic error on the selection efficiency are then calculated. The contribution from tight identification is

$$\sigma^{id}_{\epsilon} = \frac{1}{2} |\epsilon^{sel}_{+00} - \epsilon^{sel}_{-00}|, \tag{8.4}$$

where $\epsilon^{sel}_{\pm 00}$ is the selection efficiency computed using $s_{\pm 00} = (s_{id} \pm \delta s_{id}) s_{iso} s_{trig}$. A similar prescription is followed for the isolation and trigger contributions to the selection efficiency uncertainty:

$$\sigma^{iso}_{\epsilon} = \frac{1}{2} |\epsilon^{sel}_{0+0} - \epsilon^{sel}_{0-0}|, \tag{8.5}$$

$$\sigma^{trig}_{\epsilon} = \frac{1}{2} |\epsilon^{sel}_{00+} - \epsilon^{sel}_{00-}|. \tag{8.6}$$

The total systematic uncertainty on the selection efficiency is the addition of the three

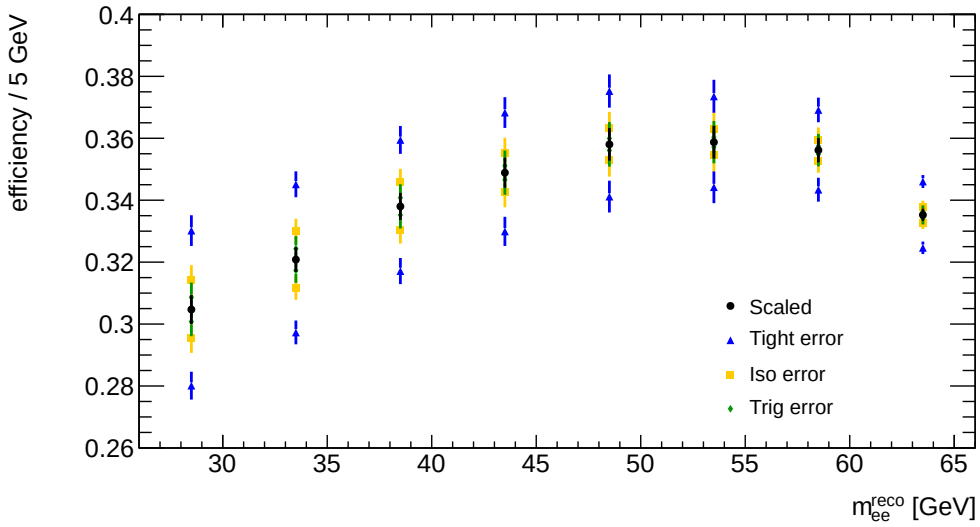

Figure 8.2: Shown are the selection efficiency computed using the nominal scale factor and the six selection efficiency curves obtained by shifting the scale factors by their individual errors.

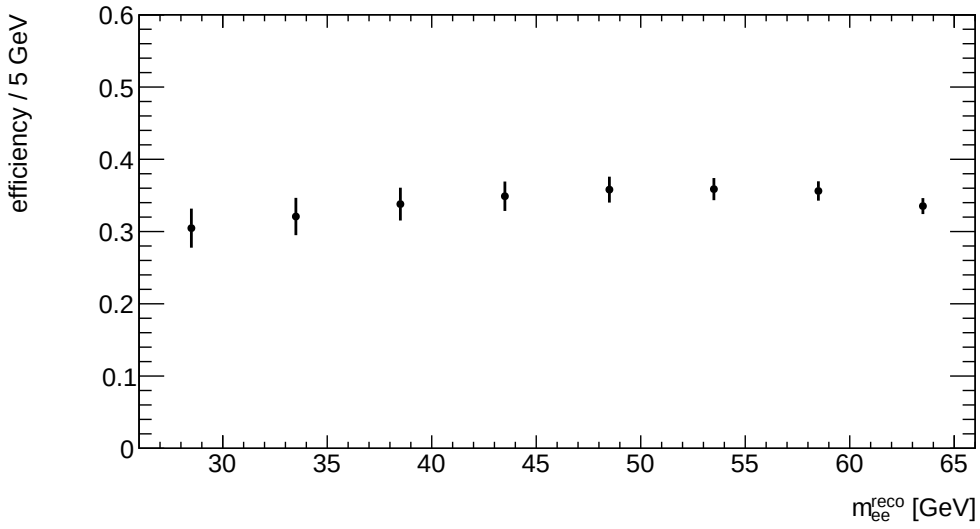

Figure 8.3: The selection efficiency with systematic uncertainty due to the identification, isolation, and trigger scale factors. The error bars represent the total systematic uncertainty coming from these three sources, added in quadrature.

in quadrature:

$$\sigma_\epsilon^{sys} = \sqrt{(\sigma_\epsilon^{id})^2 + (\sigma_\epsilon^{iso})^2 + (\sigma_\epsilon^{trig})^2}. \tag{8.7}$$

The selection efficiency with error bars representing the systematic uncertainty can be seen in Figure 8.3. The full results of the efficiency studies can be seen in Table 8.3.

m_{ee} [GeV]	ϵ^{sel}	σ_ϵ^{stat} [%]	σ_ϵ^{id} [%]	σ_ϵ^{iso} [%]	σ_ϵ^{trig} [%]	σ_ϵ^{sys} [%]
26-31	0.305	1.56	8.22	3.09	1.29	8.87
31-36	0.321	1.25	7.46	2.83	1.09	8.05
36-41	0.338	1.29	6.27	2.28	0.83	6.72
41-46	0.349	1.39	5.50	1.83	0.66	5.83
46-51	0.358	1.47	4.76	1.45	0.54	5.01
51-56	0.359	1.47	4.09	1.17	0.44	4.27
56-61	0.356	1.10	3.62	0.95	0.37	3.76
61-66	0.335	0.61	3.19	0.75	0.31	3.30

Table 8.3: Efficiency systematic studies results. Shown in this table are the selection efficiency values along with the individual systematic errors due to the use of tight identification, calorimeter isolation, and the trigger scale factor errors. The final column, σ_ϵ^{sys}, shows the total systematic uncertainty on ϵ^{sel}.

8.3 Resolution and Reconstruction Uncertainty

The systematic uncertainties on the unfolded Drell-Yan invariant mass distribution due to the iterative Bayesian technique must be estimated. Three independent sources will be assessed here: the additional statistical uncertainty on the distribution after unfolding, the uncertainty due to the limited statistics of the Monte Carlo, and the uncertainty due to reconstruction scale factors.

The statistical uncertainty on the Drell-Yan distribution is changed after unfolding. Recall that Bayesian unfolding is symbolized by Equation (5.14):

$$N_i^{DY}(m_{ee}^{true}|E_T,\eta) = \sum_j M_{ij} N_j^{DY}(m_{ee}^{reco}|E_T,\eta), \quad i,j = 1,2,3,...$$

where M_{ij} is the response matrix; $N^{DY}(m_{ee}^{reco}|E_T,\eta)$ and $N^{DY}(m_{ee}^{true}|E_T,\eta)$ are the folded and unfolded Drell-Yan distributions which are illustrated in Figure 8.4. The

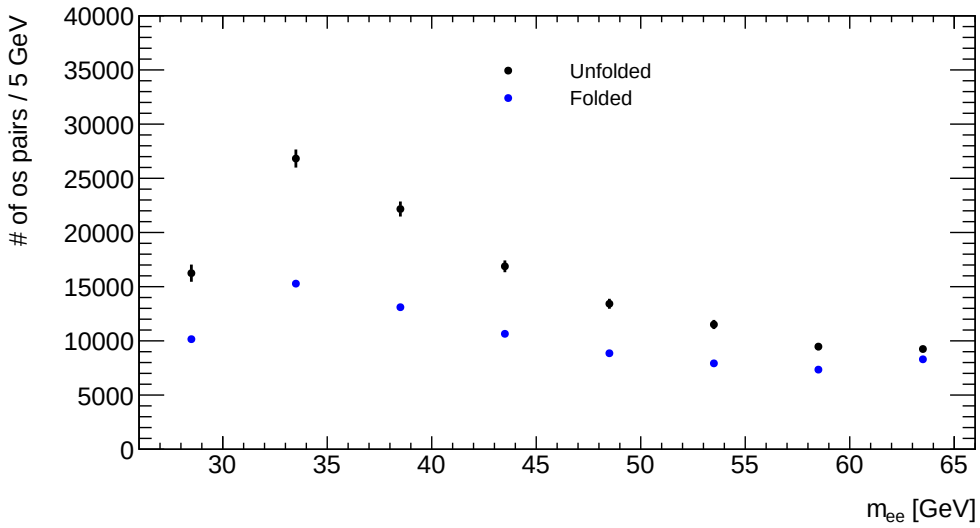

Figure 8.4: The unfolded Drell-Yan distribution (black) and the folded Drell-Yan distribution (blue) which is affected by detector resolution and reconstruction effects. The error bars are statistical.

statistical error on the unfolded distribution is computed by RooUnfold. RooUnfold performs 1000 pseudo-experiments in which the original distribution is fluctuated by its statistical error. Let σ^{stat}_{fold} be the statistical uncertainty on $N^{DY}(m^{reco}_{ee}|E_T,\eta)$ and σ^{stat}_{unfold} be the statistical error on $N^{DY}(m^{true}_{ee}|E_T,\eta)$. The additional statistical error on the Drell-Yan distribution coming from Bayesian unfolding is

$$\sigma^{stat}_{Bayes} = \sigma^{stat}_{unfold} \ominus \sigma^{stat}_{fold}, \tag{8.8}$$

where the two statistical errors have been subtracted in quadrature. This is the first of the three uncertainties that arise due to the use of Bayesian unfolding.

The next source is due to the statistical uncertainty on the Monte Carlo. The response matrix is constructed using MC and is thus affected by limited Monte Carlo statistics. To quantify how much this affects the unfolded Drell-Yan distribution, each entry in the response matrix is fluctuated by its statistical uncertainty. Using this modified response matrix, the unfolding process is performed again on the data yielding an unfolded spectrum, $N'^{DY}(m^{true}_{ee}|E_T,\eta)$, different from the original $N^{DY}(m^{true}_{ee}|E_T,\eta)$ obtained using the nominal response matrix.
These distributions can be seen in Figure 8.5. The difference between these two,

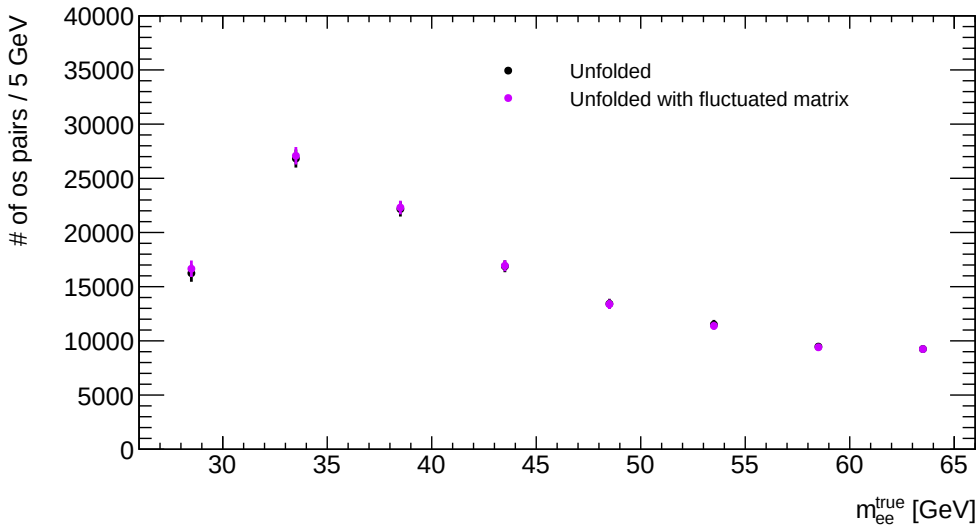

Figure 8.5: The unfolded Drell-Yan distribution using the nominal response matrix (black) and the same, however, using the fluctuated response matrix (purple). The error bars are statistical.

$$\sigma_{Bayes}^{MC} = |N^{DY}(m_{ee}^{true}|E_T,\eta) - N'^{DY}(m_{ee}^{true}|E_T,\eta)|, \tag{8.9}$$

is taken to be the error due to limited MC statistics.

The final source of systematic uncertainty comes from the use of reconstruction scale factors. Reconstruction scale factors, provided by the EGamma group, were used to weight reconstructed Monte Carlo electrons such that they better reflect reconstructed electrons found in data. These scale factors have uncertainties associated with them, which ultimately contribute to the overall unfolding uncertainty. To quantify the contribution, the reconstruction scale factors were shifted all up and all down by their uncertainties producing new sets of training histograms and response matrices. Using the new sets, Bayesian unfolding was performed giving two new unfolded spectra: $N^{DY,+}(m_{ee}^{true}|E_T,\eta)$, the unfolded distribution corresponding to the scale factors shifted up and $N^{DY,-}(m_{ee}^{true}|E_T,\eta)$, the unfolded distribution corresponding to the scale factors shifted down; these distributions can be seen in Figure 8.6. The uncertainty due to the reconstruction scale factors is then taken to be

$$\sigma_{Bayes}^{reco} = \frac{1}{2}|N^{DY,+}(m_{ee}^{true}|E_T,\eta) - N^{DY,-}(m_{ee}^{true}|E_T,\eta)|. \tag{8.10}$$

A table showing these uncertainties along with the folded, $N^{DY}(m_{ee}^{reco}|E_T,\eta)$, and

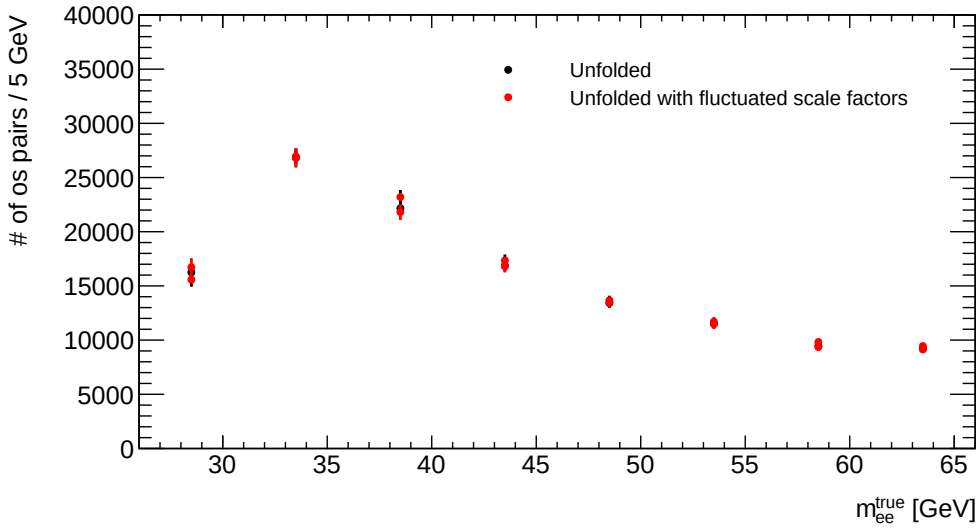

Figure 8.6: The unfolded Drell-Yan distribution using the nominal reconstruction scale factors (black) and the same distributions using reconstruction scale factors fluctuated up and down (red). The error bars are statistical.

m_{ee} [GeV]	Folded	Unfolded	σ_{Bayes}^{stat} [%]	σ_{Bayes}^{MC} [%]	σ_{Bayes}^{reco} [%]
26-31	10157 ± 262	16246 ± 793	4.14	2.52	3.53
31-36	15280 ± 310	26824 ± 834	2.36	0.95	0.27
36-41	13105 ± 276	22166 ± 693	2.31	0.63	3.13
41-46	10650 ± 244	16878 ± 544	2.27	0.34	1.62
46-51	8857 ± 219	13423 ± 459	2.37	0.31	0.67
51-56	7925 ± 202	11511 ± 422	2.63	1.11	0.98
56-61	7346 ± 176	9470 ± 333	2.57	0.69	2.46
61-66	8299 ± 175	9247 ± 310	2.61	0.04	1.70

Table 8.4: Table of the folded and unfolded Drell-Yan distributions with their statistical errors. The following three columns are the additional errors on the unfolded distribution due to the Bayesian unfolding technique. From left to right, they represent the additional statistical uncertainty attributed to unfolding, the error due to the use of Monte Carlo, and the error due to reconstruction scale factor uncertainty.

unfolded, $N^{DY}(m_{ee}^{true}|E_T,\eta)$ Drell-Yan distributions as functions of invariant mass can be seen in Table 8.4.

8.4 Acceptance Uncertainty

The calculation of the acceptance involves only MC generated quantities and so the sources contributing to the systematic uncertainty on the acceptance are the uncertainties present in event generation. The main source of uncertainty in event generation is PDF error. The MSTW group provides a central PDF set and 40 error sets for the use of PDF uncertainty studies. MSTW uses 20 free parameters in their data fitting procedure, and the best fit yields the central set[1]. The error sets are obtained using the Hessian method [38] which yields for each free parameter an eigenvector. These 20 eigenvectors probe directions, positive and negative, in PDF parameter space thus yielding 40 independent PDF error sets.

This analysis uses the MSTW2008nlo68cl central set and the corresponding 40 error sets for the study of the acceptance systematics. The following procedure is done for all 41 sets. Using PYTHIA, four million $\gamma^*/Z \to e^+e^-$ events are generated at a centre of mass energy of 7 TeV, in the range $20 < m_{ee} < 75$ GeV. These selection requirements are applied to each event:

- Exactly two electrons, opposite in charge, are required for each event. These electrons are selected prior to any final state radiation
- Both electrons must have $E_T > 12$ GeV, with at least one of the two having $E_T > 15$ GeV
- Both electrons must have $|\eta| < 2.4$
- The invariant mass spectrum is computed in the range $26 < m_{ee}^{true} < 66$ GeV.

Taking the ratio of the true Drell-Yan pairs that pass the kinematic (E_T and η) requirements to the total number of true Drell-Yan pairs, the acceptance (Equation (5.15)) is obtained:

$$A_i(m_{ee}^{true}) = \frac{N_i^{DY}(m_{ee}^{true}|E_T,\eta)|_{MC}}{N_i^{DY}(m_{ee}^{true})|_{MC}}, \quad i = 1,2,3,... \tag{8.11}$$

[1]Recall that MSTW's central set was used in computing the acceptance shown in Chapter 7.

So for each PDF set, an acceptance correction is produced giving 41 in total. Figure 8.7 shows the resultant 41 acceptance curves.

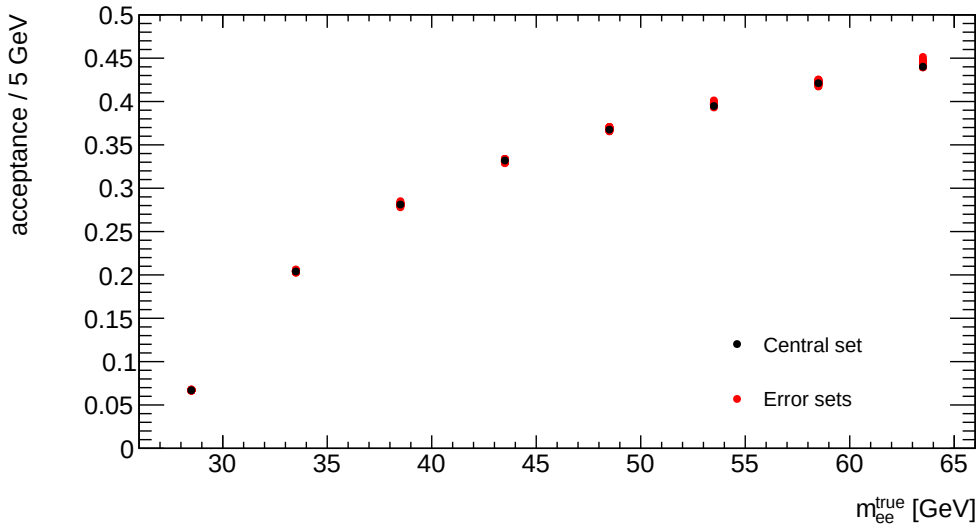

Figure 8.7: The 41 acceptance curves produced using the 41 MSTW PDF sets. The black data points present the acceptance computed using the central set, and the red data points correspond to the 40 error sets.

The MSTW group recommends the use of their asymmetric Master Equations [8],

$$\Delta X^{+}_{max} = \sqrt{\sum_{i=1}^{20} \max(X^{+}_{i} - X_0, X^{-}_{i} - X_0, 0)^2} \tag{8.12}$$

$$\Delta X^{-}_{max} = \sqrt{\sum_{i=1}^{20} \max(X_0 - X^{+}_{i}, X_0 - X^{-}_{i}, 0)^2}, \tag{8.13}$$

to calculate the uncertainty on any physical observable (found using the central set) due to MSTW PDF uncertainty. The quantity ΔX^{+}_{max} represents the systematic error on the observable X_0 resulting from PDF uncertainty in the positive direction in parameter space, while ΔX^{-}_{max} represents that for the negative direction. Following this recommendation, the Master Equations are used to calculate the error on the acceptance.

In addition to PDF fitting uncertainty, there exist discrepancies between competing PDF fitting groups. The MSTW group has published a different PDF fit from

the CTEQ group [39]. These differences need to be quantified and added to the overall acceptance uncertainty. The acceptances calculated using the central sets of MSTW08, CTEQ6.6, HERA10 [40], and NNPDF21 [41] denoted by A, A_C, A_H, and A_N respectively are now compared. The four acceptance curves can be seen in Figure 8.8 and these results are displayed in Table 8.5. Note that the statistical uncertainties on the acceptance values are less than 1%.

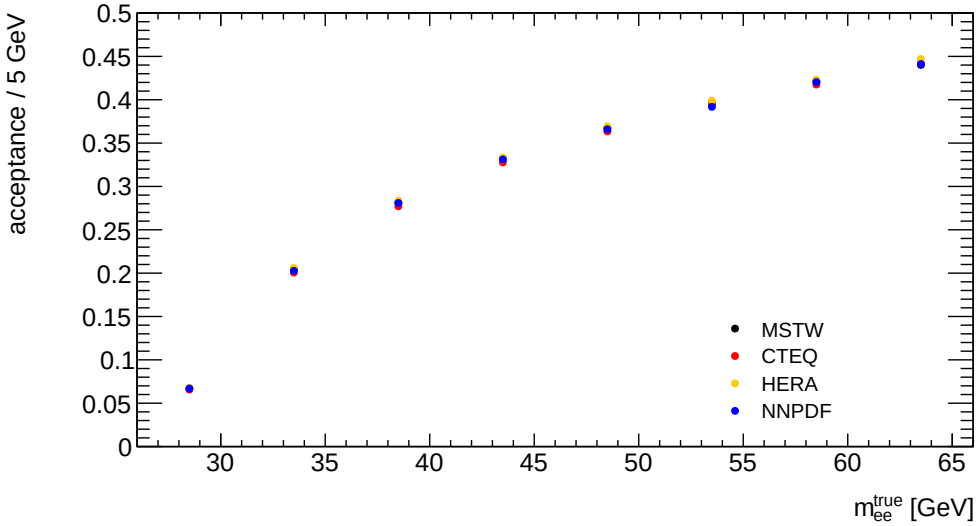

Figure 8.8: A comparison of the acceptance curves calculated using the central sets of MSTW, CTEQ, HERA, and NNPDF.

m_{ee} [GeV]	A	A_C	A_H	A_N
26-31	0.067	0.066	0.068	0.067
31-36	0.204	0.201	0.206	0.203
36-41	0.281	0.277	0.284	0.281
41-46	0.332	0.328	0.333	0.331
46-51	0.368	0.363	0.369	0.366
51-56	0.395	0.395	0.399	0.392
56-61	0.421	0.417	0.423	0.420
61-66	0.440	0.442	0.447	0.441

Table 8.5: Table of acceptance values computed with events generated with MSTW (A), CTEQ (A_C), HERA (A_H), and NNDPDF (A_N).

With these, the full systematic uncertainty on the acceptance can be computed.

Using the Master Equations, the systematic error on the acceptance due to MSTW PDF fitting error is

$$\Delta A^{+}_{max} = \sqrt{\sum_{i=1}^{20} \max(A^{+}_{i} - A_0, A^{-}_{i} - A_0, 0)^2} \quad (8.14)$$

$$\Delta A^{-}_{max} = \sqrt{\sum_{i=1}^{20} \max(A_0 - A^{+}_{i}, A_0 - A^{-}_{i}, 0)^2}, \quad (8.15)$$

where $A_0 \equiv A$ is the acceptance computed using the central set and $A^{\pm}$ are the acceptances calculated using the 40 error sets. The uncertainty due to the discrepancies between MSTW and CTEQ, HERA, and NNPDF is taken to be

$$\sigma^{model}_{A_C} = |A - A_C| \quad (8.16)$$

$$\sigma^{model}_{A_H} = |A - A_H| \quad (8.17)$$

$$\sigma^{model}_{A_N} = |A - A_N|. \quad (8.18)$$

The systematic uncertainty on A is taken to be the greater of ΔA^{+}_{max} and ΔA^{-}_{max} added in quadrature to the maximum of the errors due to model discrepancies:

$$\sigma^{sys}_{A} = \max(\Delta A^{+}, \Delta A^{-}) \oplus \max(\sigma^{model}_{A_C}, \sigma^{model}_{A_H}, \sigma^{model}_{A_N}). \quad (8.19)$$

m_{ee} [GeV]	A	ΔA^{+} [%]	ΔA^{-} [%]	$\sigma^{model}_{A_C}$ [%]	$\sigma^{model}_{A_H}$ [%]	$\sigma^{model}_{A_N}$ [%]
26-31	0.067	2.76	1.56	2.00	0.96	0.08
31-36	0.204	1.95	1.29	1.66	1.06	0.63
36-41	0.281	2.19	1.79	1.46	0.87	0.09
41-46	0.332	1.30	2.12	1.28	0.40	0.24
46-51	0.368	2.35	0.78	1.11	0.46	0.43
51-56	0.395	4.09	0.51	0.06	1.10	0.75
56-61	0.421	2.49	1.61	0.86	0.45	0.17
61-66	0.440	5.61	0.26	0.32	1.55	0.24

Table 8.6: Quantities required to compute the systematic uncertainty on the acceptance. Shown is the nominal acceptance value, along with the results of the Master Equations, and the model discrepancies.

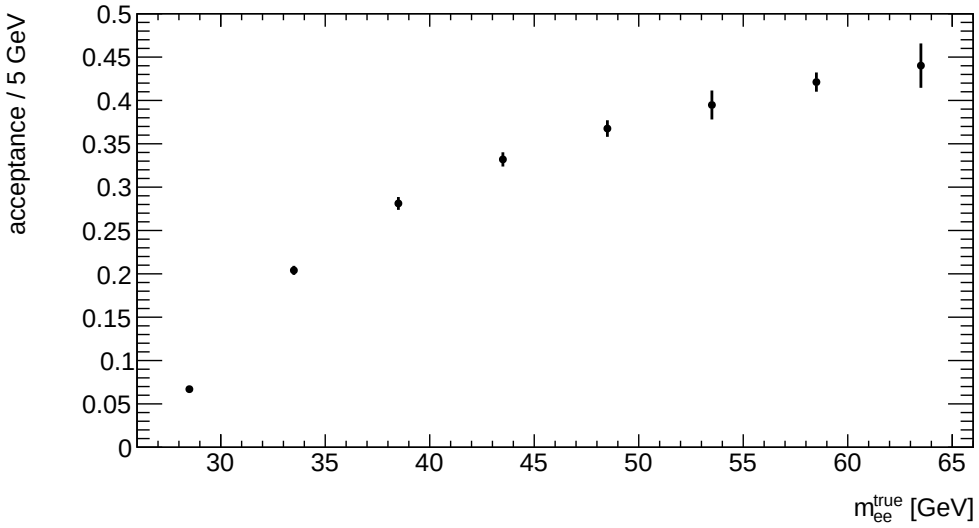

Figure 8.9: Acceptance with error bars representing systematic errors.

m_{ee} [GeV]	A	σ_A^{stat} [%]	σ_A^{sys} [%]
26-31	0.067	0.41	3.41
31-36	0.204	0.29	2.56
36-41	0.281	0.30	2.63
41-46	0.332	0.33	2.47
46-51	0.368	0.37	2.60
51-56	0.395	0.41	4.23
56-61	0.421	0.44	2.63
61-66	0.440	0.45	5.82

Table 8.7: Acceptance with statistical and systematic uncertainties.

The numbers that Equation 8.19 uses are given in Table 8.6. A plot of the acceptance with error bars representing the systematic uncertainty is shown in Figure 8.9 and a table of the acceptance and both its statistical and systematic uncertainties is given in Table 8.7. The statistical errors are calculated using binomial statistics.

8.5 Total Uncertainty

A table summarizing the systematic uncertainty studies can be seen in Table 8.8. In addition to the uncertainties from heavy quark MC, scale factors, Bayesian unfolding, and the acceptance, a constant 3.7 % luminosity systematic uncertainty $\sigma_{\mathcal{L}}^{sys}$ is given

[42]. The total systematic uncertainty σ^{sys} is the sum of each of the columns added in quadrature.

m_{ee} [GeV]	σ^{sys}_{HQ} [%]	σ^{sys}_{ϵ} [%]	σ^{sys}_{Bayes} [%]	σ^{sys}_{A} [%]	$\sigma^{sys}_{\mathcal{L}}$ [%]	σ^{sys} [%]
26-31	2.67	8.87	4.33	3.41	3.7	11.4
31-36	1.68	8.05	0.99	2.56	3.7	9.42
36-41	1.68	6.72	3.19	2.63	3.7	8.87
41-46	1.23	5.83	1.65	2.47	3.7	7.62
46-51	1.57	5.01	0.74	2.60	3.7	6.97
51-56	1.73	4.27	1.48	4.23	3.7	7.42
56-61	1.81	3.76	2.56	2.63	3.7	6.67
61-66	1.75	3.30	1.70	5.82	3.7	8.02

Table 8.8: The systematic uncertainties from heavy quark MC, scale factors, Bayesian unfolding, and acceptance. A constant luminosity systematic uncertainty is also given. The total systematic uncertainty is the individual errors added in quadrature.

The total systematic uncertainty quoted is the systematic uncertainty on the Drell-Yan differential cross section which is calculated in the next chapter.

Chapter 9

The Drell-Yan Differential Cross Section

Having measured the number of opposite sign electron pairs in data and an estimate of the background using Monte Carlo, the number of Drell-Yan pairs in data was determined. The selection efficiency, detector resolution, reconstruction efficiency, and kinematic acceptance were quantified and used to correct the measurement. Having done this, the quantity central to this thesis can now be calculated – the Drell-Yan differential cross section. In this chapter, the differential cross section calculation is performed and concludes with a discussion of the analysis.

9.1 Results

The Drell-Yan differential cross section (Equation (5.17)) was derived in Chapter 5 to be

$$\left(\frac{d\sigma^{DY}}{dm_{ee}}\right)_i (m_{ee}^{true}) = \frac{M_{ij}\left[N_j^{DY}(m_{ee}^{reco}|E_T,\eta,id,iso,trig)/\epsilon_j(m_{ee}^{reco})\right]}{A_i(m_{ee}^{true})\Delta m_{ee,i}^{true}\int \mathcal{L}dt},$$

where $i,j = 1,2,3,...$ index true invariant mass bins. All these quantities have been computed. The number $N_j^{DY}(m_{ee}^{reco}|E_T,eta,id,iso,trig)$ of Drell-Yan pairs passing selection requirements is obtained by taking the measured number of e^+e^- pairs and subtracting the Monte Carlo background estimate:

$$N_j^{DY}(m_{ee}^{reco}|E_T,\eta,id,iso,trig) \\ = N_j^{ee}(m_{ee}^{reco}|E_T,\eta,id,iso,trig)|_{data} - N_j^{bkg}(m_{ee}^{reco}|E_T,\eta,id,iso,trig)|_{MC}. \quad (9.1)$$

This subtraction is illustrated in Figure 9.1. In this figure, the black markers represent all opposite sign electron pairs while the red markers represent only the Drell-Yan pairs.

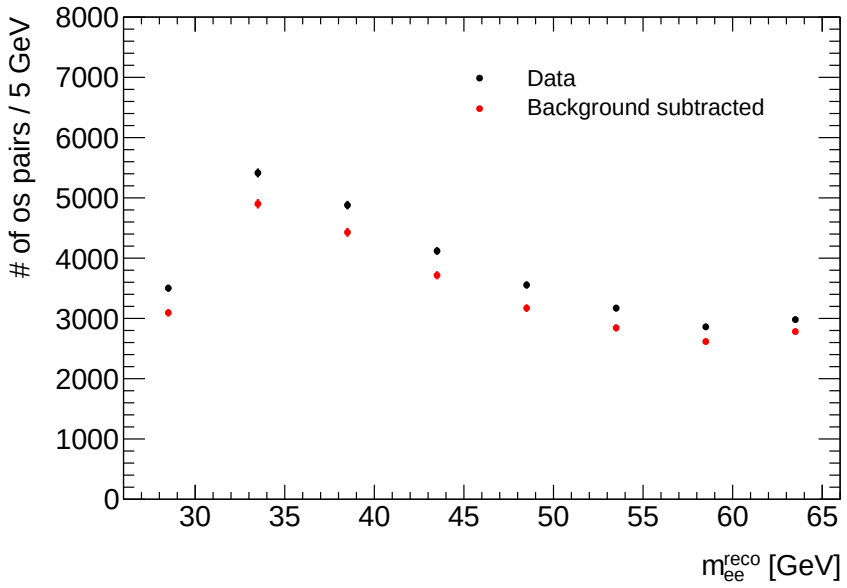

Figure 9.1: Background subtraction.

Having the background subtracted distribution, the next step is to apply the selection efficiency correction. The selection efficiency corrected distribution is

$$N_j^{DY}(m_{ee}^{reco}|E_T,\eta) = \frac{N_j^{DY}(m_{ee}^{reco}|E_T,\eta,id,iso,trig)}{\epsilon_j(m_{ee}^{reco})}, \quad (9.2)$$

where ϵ_j^{sel} is the selection efficiency. The corrected and uncorrected distributions can be seen in Figure 9.2. Here the blue markers represent the corrected Drell-Yan distribution. Dividing by ϵ_j^{sel} effectively reverses the inefficiencies associated with tight identification, calorimeter isolation, and the EF_2e12_medium trigger requirements that were placed on the electron pairs.

The next step in the analysis is to undo the effects of detector resolution and

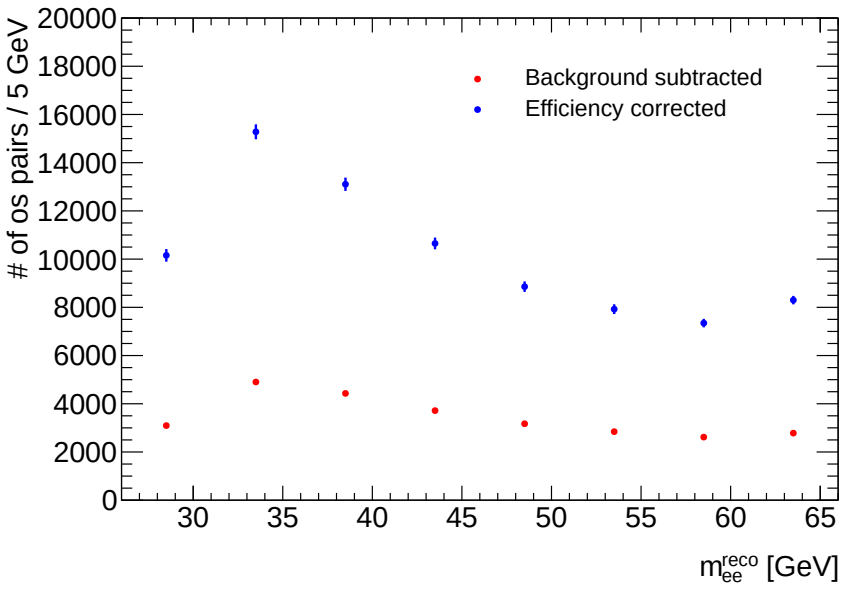

Figure 9.2: Efficiency correction.

mis-reconstruction of electrons. This is done using the iterative Bayesian unfolding technique. Bayesian unfolding can be symbolically represented by the equation

$$N_i^{DY}(m_{ee}^{true}|E_T,\eta) = \sum_j M_{ij} N_j^{DY}(m_{ee}^{reco}|E_T,\eta), \tag{9.3}$$

where M_{ij} is the response matrix and $N_i^{DY}(m_{ee}^{true}|E_T,\eta)$ is the number of true Drell-Yan pairs within acceptance. The unfolded distribution obtained using the Bayesian technique can be seen in Figure 9.3; the green markers represent the unfolded distribution.

Finally, to undo the effects of the E_T and η cuts, the acceptance correction is used. As it was for the efficiency correction, application of the acceptance correction is a simple division:

$$N_i^{DY}(m_{ee}^{true}) = \frac{N_i^{DY}(m_{ee}^{true}|E_T,\eta)}{A_i(m_{ee}^{true})}, \tag{9.4}$$

where $A_i(m_{ee}^{true})$ is the acceptance and $N_i^{DY}(m_{ee}^{true})$ is the acceptance corrected, true Drell-Yan invariant mass distribution. This acceptance corrected distribution can be seen in Figure 9.4, represented by the orange markers.

All corrections applied to the initial data measurement can be seen in Figure

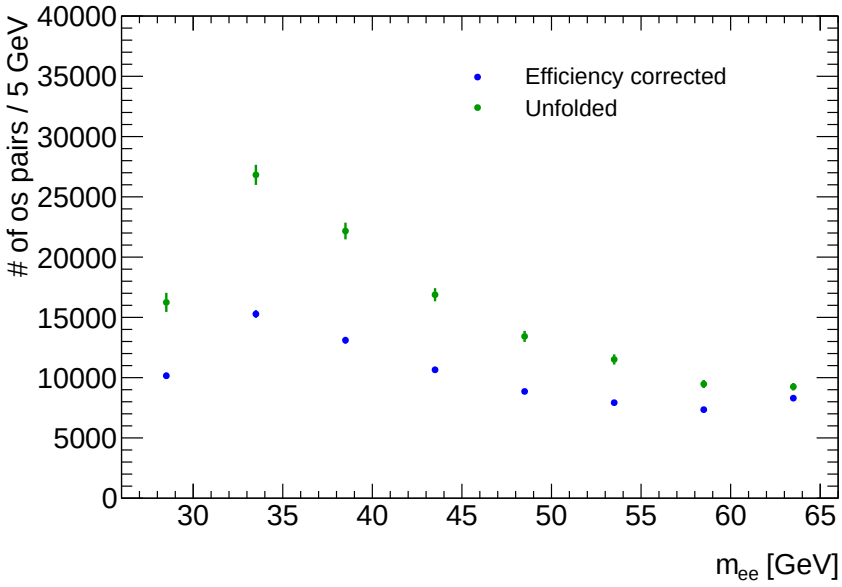

Figure 9.3: Bayesian unfolding.

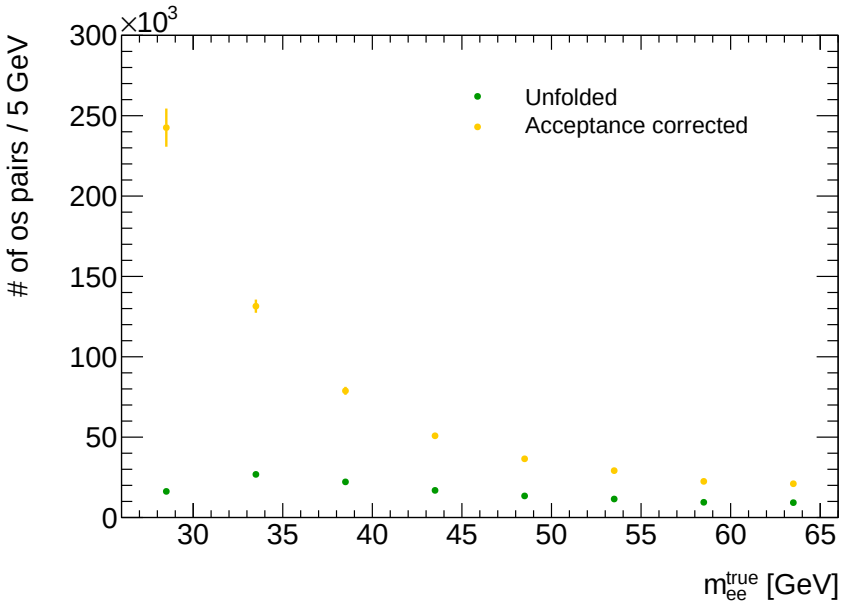

Figure 9.4: Acceptance correction.

9.5. The solid lines correspond to theoretical predictions generated by PYTHIA. This figure shows the changes in the number of Drell-Yan pairs as each subsequent correction is made.

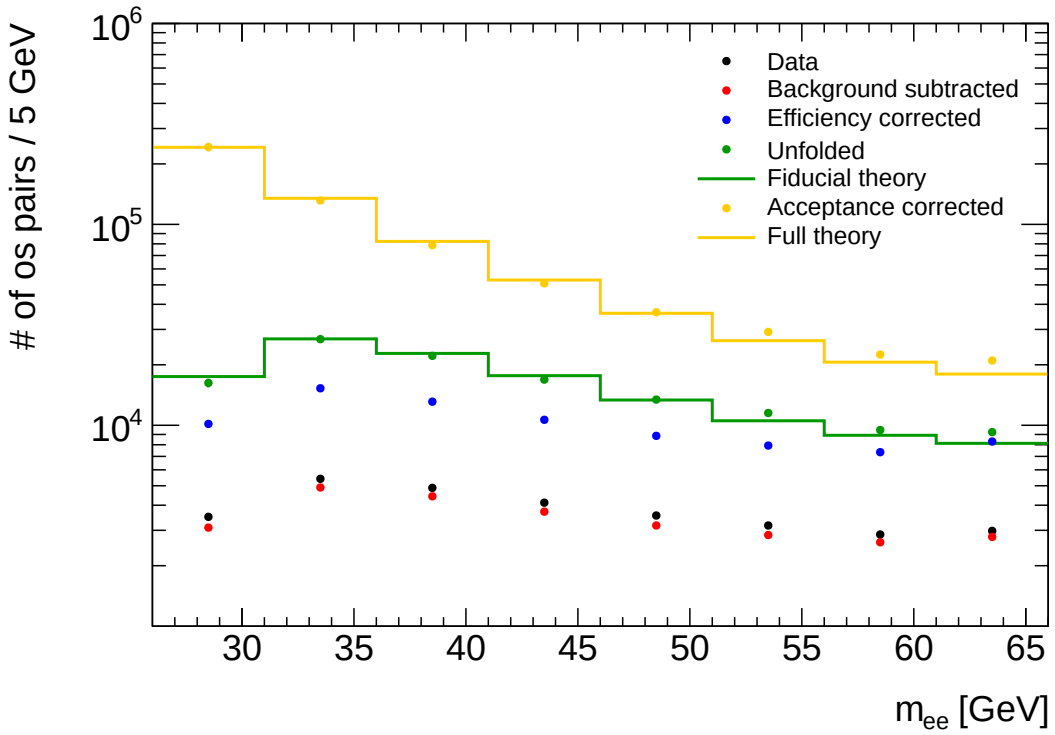

Figure 9.5: All corrections.

Referring to Equation 5.17, by dividing the acceptance corrected distribution by the true invariant mass bin width $\Delta m_{ee,i}^{true} = 5$ and the integrated luminosity of the data set used in this analysis, $\int \mathcal{L} dt = 1680$ pb^{-1}, the desired Drell-Yan differential cross section is obtained. Shown on top in Figure 9.6 is the Drell-Yan differential cross section $\frac{d\sigma^{DY}}{dm_{ee}}$ and the PYTHIA prediction. The measurement closely matches the theory. The error bars represent the total uncertainty obtained by adding the contributions from statistics and systematics in quadrature.

In addition to this differential cross section, another useful one can be readily calculated from the results. Shown on the bottom of Figure 9.6 is the Drell-Yan differential cross section in which the pairs have the following kinematic properties:

- Both electrons must have $E_T > 12$ GeV, with at least one of the two having $E_T > 15$ GeV
- Both electrons must have $|\eta| > 2.4$
- The invariant mass spectrum is computed in the range $26 < m_{ee}^{true} < 66$ GeV.

This differential cross section is called the fiducial differential cross section (and to clearly distinguish it from the cross section on top, the cross section above will be referred to as the full differential cross section). Again, the theoretical curve, which shows agreement with the measurement, is also plotted. The full results are on display in Table 9.1, showing the differential cross section values with statistical and systematic errors and the total uncertainty.

m_{ee} [GeV]	$\frac{d\sigma^{DY}}{dm_{ee}}$	σ^{stat}_{full}	σ^{sys}_{full}	σ_{full}	$\frac{d\sigma^{DY}_{fid}}{dm_{ee}}$	σ^{stat}_{fid}	σ^{sys}_{fid}	σ_{fid}
26-31	28.71	1.43	3.27	3.57	1.92	0.09	0.21	0.23
31-36	15.59	0.49	1.47	1.55	3.18	0.10	0.29	0.31
36-41	9.347	0.29	0.83	0.88	2.63	0.08	0.22	0.24
41-46	6.03	0.20	0.46	0.50	2.00	0.07	0.14	0.16
46-51	4.33	0.15	0.30	0.34	1.59	0.05	0.10	0.12
51-56	3.455	0.12	0.26	0.28	1.36	0.05	0.08	0.10
56-61	2.676	0.10	0.18	0.20	1.13	0.04	0.07	0.08
61-66	2.498	0.08	0.20	0.22	1.10	0.04	0.06	0.07

Table 9.1: The full and fiducial Drell-Yan differential cross sections as functions of true invariant mass along with the statistical, systematic, and total uncertainties. All entries in this table are in units of pb/GeV, unless otherwise indicated.

9.2 Discussion

The computation of the Drell-Yan differential cross section involved several techniques which include the use of Monte Carlo samples to estimate the Drell-Yan background, scale factors to compute the selection efficiency, Bayesian unfolding to remove the effects of detector resolution and mis-reconstruction of electrons, and event generation to compute the acceptance. Some of the limitations that arise from the use of these techniques are now discussed.

The background was estimated using Monte Carlo, which of course does not fully reflect reality. The MC samples that are most problematic are the heavy quark ones, namely the $b\bar{b}(c\bar{c})$ and $t\bar{t}$ samples. The QCD reactions in the ATLAS detector are highly complex and their simulation is difficult. Data-driven techniques such as the matrix method or the ABCD method, though difficult, may be used to estimate the QCD background. Such techniques lead to estimates that better reflect the physics within the ATLAS detector.

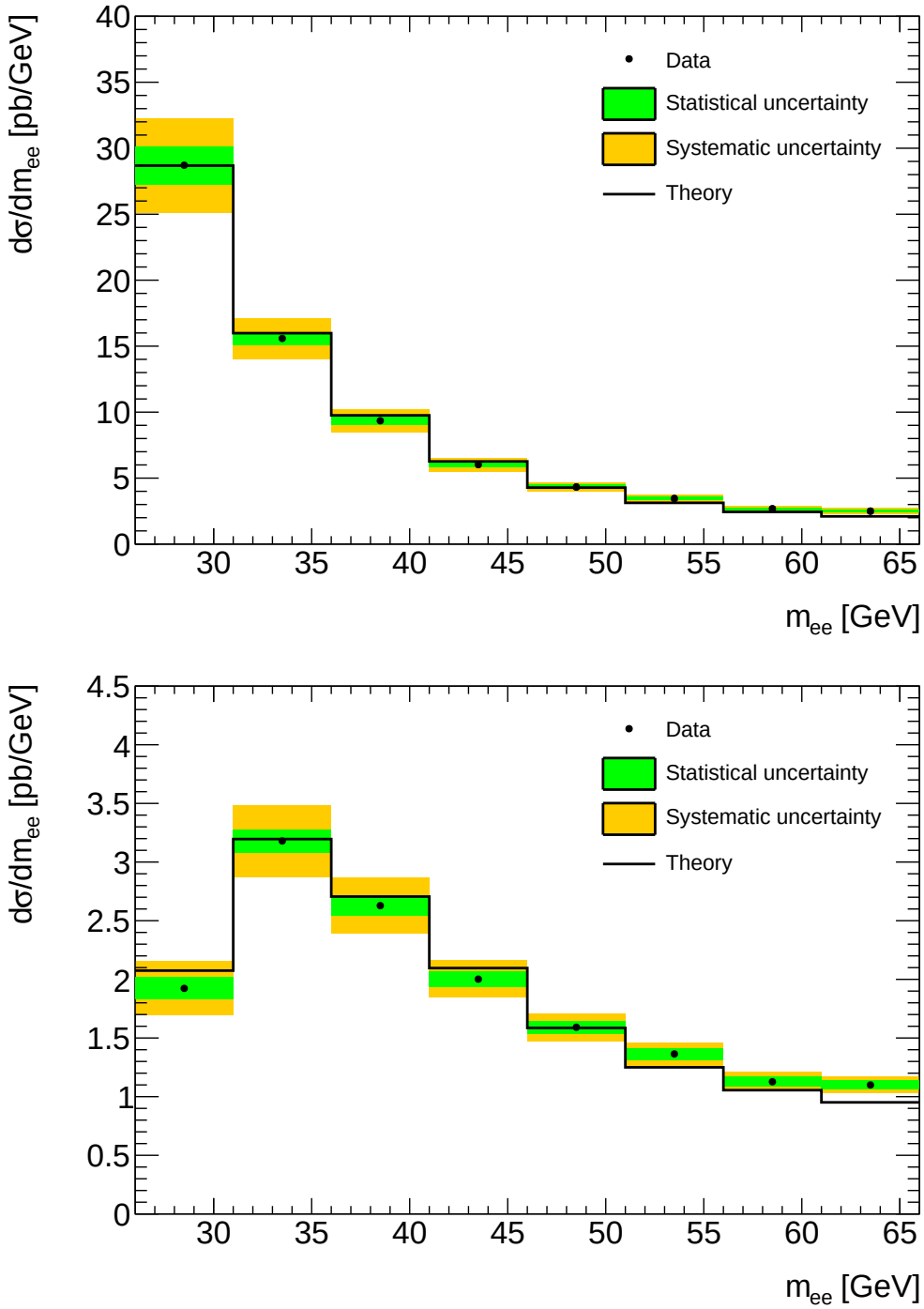

Figure 9.6: Both the full (top) and fiducial (bottom) Drell-Yan differential cross sections. The error bars seen are the statistical and systematic errors added in quadrature.

Efficiency systematic uncertainties were estimated conservatively. They were calculated by fluctuating electron scale factors by their errors, for example the tight identification scale factor, $s_{id} \pm \delta s_{id}$. The overall scale factor then took the form

$$s_{\pm 00} = (s_{id} \pm \delta s_{id}) s_{iso} s_{trig}. \tag{9.5}$$

Of course the actual tight identification scale factor of the electron may fall anywhere between $s_{id} - \delta s_{id}$ and $s_{id} + \delta s_{id}$. By introducing some pre-factor C between $0 < C < 1$ in front of the scale factor uncertainty, $s_{id} \pm C\delta s_{id}$, the systematic error due to the scale factors would be better approximated and subsequently reduced. The use of this pre-factor C reduces the differences between the fluctuated scale factors (for example $s_{\pm 00}$) and the nominal scale factor s_{000}. This ultimately leads to smaller systematic errors due to the efficiency.

The acceptance was calculated by generating large Monte Carlo samples using PYTHIA. PYTHIA, however, is a leading order event generator. A more accurate calculation of the acceptance would involve studies of next-to-leading order events. Calculations with higher order electroweak corrections applied to the Drell-Yan process at colliders are at the forefront of QCD theoretical research.

Chapter 10

Conclusion

The Drell-Yan process in ATLAS involves the annihilation of a quark from one proton and an antiquark from another to produce a virtual photon or Z boson which then decays into a lepton-antilepton pair. The goal of this analysis was to compute the differential cross section of this process as a function of invariant mass in the electron channel, when the lepton-antilepton pair is an electron-positron pair. In particular, this thesis measured the low invariant mass range, $26 < m_{ee} < 66$ GeV, a region that presents difficulties due to the poorer resolution of the ATLAS detector at low electron energies.

The Drell-Yan differential cross section presented was calculated using data from proton-proton collisions at 7 TeV produced by the LHC and collected by the ATLAS detector. The data set used in this analysis was collected in 2011 and has an integrated luminosity of 1.68 fb^{-1}. The differential cross section values along with the statistical, systematic, and total uncertainties are presented in Table 10.1. This table shows the figures for both the full and fiducial differential cross sections.

Various experimental techniques were used in this analysis, starting with a cut based approach to finding all e^+e^- pairs in data. Candidate Drell-Yan pairs were required to pass a series of event selection requirements and following this, Monte Carlo samples were used to estimate the Drell-Yan background. The tag and probe method was used to compute scale factors which allowed the efficiency in selecting Drell-Yan pairs to be calculated using Monte Carlo rather than data. Bayesian unfolding was used to undo the effects of detector resolution and mis-reconstruction of electrons. The acceptance was computed using the Monte Carlo method.

The Drell-Yan differential cross sections include statistical uncertainties and also systematic uncertainties due to Monte Carlo background estimation, scale factors,

m_{ee} [GeV]	$\frac{d\sigma^{DY}}{dm_{ee}}$	σ_{full}	$\frac{d\sigma^{DY}_{fid}}{dm_{ee}}$	σ_{fid}
26-31	28.71	3.41	1.92	0.22
31-36	15.59	1.44	3.18	0.28
36-41	9.35	0.81	2.63	0.22
41-46	6.03	0.45	2.00	0.14
46-51	4.33	0.30	1.59	0.10
51-56	3.46	0.25	1.36	0.08
56-61	2.68	0.18	1.13	0.07
61-66	2.50	0.20	1.10	0.06

Table 10.1: The Drell-Yan differential cross section values as functions of invariant mass. The uncertainties quoted are the total errors, both statistical and systematic. All entries in this table are in units of pb/GeV, unless otherwise indicated. The full and fiducial cross section values are given.

Bayesian unfolding, and parton distribution functions. The measurement has a precision between 12.4% and 8.01% from lower to higher invariant mass bins.

Ultimately, the usefulness of this measurement is its ability to constrain parton distribution functions. The Drell-Yan differential cross section computed in this thesis is mathematically related to proton's parton distribution functions. The LHC has produced Drell-Yan collisions that have been kinematically impossible before, allowing regions of parton distribution function space to be probed for the first time.

Appendix A

Tag And Probe

Data driven techniques should be used whenever possible as Monte Carlo does not perfectly reflect the physics taking place within the ATLAS detector. Particle identification, an important part of any analysis, has an efficiency associated with it. In order to determine this identification efficiency, a data driven method known as tag and probe is used. This appendix will describe the tag and probe method in the context of $Z \rightarrow e^+e^-$ events. The efficiency calculation is introduced and is then generalized, requiring one set of selection requirements on the tag and another set on the probe. This appendix then concludes with the generalization to bin efficiencies.

A.1 Efficiency Calculation

The tag and probe method relies on events in which there are two final state objects [35] such as $Z \rightarrow e^+e^-$. One of the electrons from the Z boson is required to pass a set of strict requirements known as tag selection. These requirements are chosen such that if an electron satisfies them, it is likely to have originated from a Z boson. Therefore, requiring one of the electrons from a $Z \rightarrow e^+e^-$ event to pass tag selection effectively separates these events from background ones. An electron that passes tag selection is known as a *tag* and the second electron is then known as a *probe*.

Assume that the total number of Z events in some data sample is N, an unknown. Electron pairs are required to pass a set of analysis selection cuts. If the efficiency of a single electron passing these cuts is ϵ_{tp}, then the number of pairs with at least one electron passing these cuts is

$$N_1 = \epsilon_{tp}(1-\epsilon_{tp})N + (1-\epsilon_{tp})\epsilon_{tp}N + 2\epsilon_{tp}^2 N. \tag{A.1}$$

The first term in Equation (A.1) is the number of pairs in which the first electron passes the cuts while the second fails. The second term is the contribution from pairs where the first fails and the second passes. Lastly, the third term is the number of pairs in which both pass the selection cuts. When both electrons pass the cuts, the first electron may be designated the tag and the second electron, the probe. Conversely, the second electron may be the tag while the first, the probe. This leads to the factor of 2 seen in the third term. Let N_2 be the number of pairs in which both electrons pass the cuts. This is just the third term in Equation (A.1):

$$N_2 = 2\epsilon_{tp}^2 N. \tag{A.2}$$

Using Equations (A.1) and (A.2), the efficiency ϵ_{tp} may be determined. It is simply the ratio of the number N_2 to N_1:

$$\frac{N_2}{N_1} = \frac{2\epsilon_{tp}^2 N}{\epsilon_{tp}(1-\epsilon_{tp})N + (1-\epsilon_{tp})\epsilon_{tp}N + 2\epsilon_{tp}^2 N} = \epsilon_{tp}. \tag{A.3}$$

Generally, the requirements on the tag and the probe differ. Often, strict requirements are applied to the tag in order to reduce background and the looser analysis selection requirements are applied to the probe. Suppose that in addition to the analysis requirements, the tag must satisfy some strict requirement. The efficiency of selecting a tag is factorized:

$$\epsilon = \epsilon_{tp}\epsilon_{tag}, \tag{A.4}$$

where ϵ_{tp} is the efficiency of the analysis cuts and ϵ_{tag} is the efficiency of the additional requirement on tags. Each electron can satisfy the analysis selection requirements and additionally, the tag requirement. A table listing the probabilities of each outcome can be seen in Table (A.1).

Let N_1' be the number of pairs with at least one tag. Using Table A.1, it is given by the equation

Analysis, ϵ_{tp}	Tag, ϵ_{tag}	Probability
Fail	Fail	$1 - \epsilon_{tp}$
Pass	Fail	$\epsilon_{tp}(1 - \epsilon_{tag})$
Pass	Pass	$\epsilon_{tp}\epsilon_{tag}$

Table A.1: A table listing the probability of an electron passing or failing the analysis selection, and passing both the analysis and tag selection.

$$\begin{aligned} N_1' &= \epsilon_{tp}\epsilon_{tag}[(1-\epsilon_{tp}) + \epsilon_{tp}(1-\epsilon_{tag})] + [(1-\epsilon_{tp}) + \epsilon_{tp}(1-\epsilon_{tag})]\epsilon_{tp}\epsilon_{tag} + 2\epsilon_{tp}^2\epsilon_{tag}^2 \\ &= 2\epsilon_{tp}\epsilon_{tag}. \end{aligned} \tag{A.5}$$

The number N_2' of pairs with one tag and one probe is then

$$\begin{aligned} N_2' &= \epsilon_{tp}\epsilon_{tag}[\epsilon_{tp}(1-\epsilon_{tag})] + [\epsilon_{tp}(1-\epsilon_{tag})]\epsilon_{tp}\epsilon_{tag} + 2\epsilon_{tp}^2\epsilon_{tag}^2 \\ &= 2\epsilon_{tp}^2\epsilon_{tag}. \end{aligned} \tag{A.6}$$

The ratio of N_2' to N_1' gives the desired efficiency ϵ_{tp}:

$$\frac{N_2'}{N_1'} = \epsilon_{tp}. \tag{A.7}$$

Note that any additional event selection cut introduces a factor to both N_1' and N_2', just like ϵ_{tag} in Equations (A.5) and (A.6). Therefore, the final result obtained when taking the ratio remains unchanged.

To generalize the efficiency calculation given by Equation (A.7), consider the efficiency $\epsilon_{tp,i}$ for bin i. By considering the efficiency in i, the probe is constrained to also be in that bin; however, the tag may be in any bin j, which may or may not be the same as i. Equations (A.5) and (A.6) generalize to become

$$\begin{aligned} N_{1,i}' &= 2\sum_{j}^{N_{bin}} \epsilon_{tp,j}\epsilon_{tag,j}[(1-\epsilon_{tp,i}) + \epsilon_{tp,i}(1-\epsilon_{tag,i})] \\ &= 2\sum_{j}^{N_{bin}} \epsilon_{tp,j}\epsilon_{tag,j}, \end{aligned} \tag{A.8}$$

and

$$\begin{aligned} N'_{2,i} &= 2\sum_{j}^{N_{bin}} \epsilon_{tp,j}\epsilon_{tag,j}[\epsilon_{tp,i}(1-\epsilon_{tag,i})] \\ &= 2\epsilon_{tp,i}\sum_{j}^{N_{bin}} \epsilon_{tp,j}\epsilon_{tag,j}, \end{aligned} \tag{A.9}$$

where N_{bin} is the number of bins. The factor of 2 accounts for the possibility that either of the two electrons may be found in bin i or in other words, either electron may be the probe. Dividing Equation (A.9) by (A.8) gives the efficiency $\epsilon_{tp,i}$ for that bin:

$$\frac{N'_{2,i}}{N'_{1,i}} = \epsilon_{tp,i}. \tag{A.10}$$

Appendix B

Iterative Bayesian Unfolding

The following description of the iterative Bayesian unfolding technique summarizes G. D'Agostini's work on the subject [34]. As D'Agostini describes, Bayes' theorem offers a way to unfold experimental distributions to obtain estimates of true distributions, a process called unfolding. The weakness of Bayes' theorem is the need for a prior; however, this apparent weakness is overcome by the use of an iterative procedure. The need for unfolding will be motivated in this appendix chapter and a mathematical treatment of the iterative Bayesian method will be presented.

B.1 Motivation

Consider an experiment in which a particle with four-momentum $p = (E, p_x, p_y, p_z)$ traverses through some detector. Using information from the detector, the particle is reconstructed. The physical particle itself is known as the true particle and all its properties are known as its true properties. In this example, the true four-momentum is $p^{true} = p$, and its true energy is $E^{true} = E$ and so on. The reconstruction of the true particle is known as the reconstructed particle and similarly, its properties are known as reconstructed properties. Due to detector effects, the reconstructed four-momentum is in general different from the true one:

$$p^{true} = (E^{true}, p_x^{true}, p_y^{true}, p_z^{true}) \neq p^{reco} = (E^{reco}, p_x^{reco}, p_y^{reco}, p_z^{reco}). \tag{B.1}$$

The goal of an experimentalist is to remove detector effects from reconstructed particles thus unfolding them into true particles whose physical observables are directly

comparable to theoretical predictions.

When confronted with the problem of unfolding a single variable, for example the reconstructed invariant mass m_{ll}^{reco} of dileptons to the true invariant mass m_{ll}^{true}, the most common method of unfolding is known as *bin-by-bin* correction. This method requires the use of Monte Carlo to generate the physical process of interest or true events. Monte Carlo is then used to simulate the response of the detector to these true events thus yielding reconstructed events. Using these Monte Carlo events, an efficiency

$$\epsilon_{bin} = \frac{N_i^{reco}}{N_i^{true}}, \quad i = 1, 2, 3, ..., \tag{B.2}$$

is calculated. Index i denotes the bin number, and N_i^{reco} and N_i^{true} are the number of reconstructed and true events found in i, respectively. The efficiency is then used to estimate the number of true events observed in the data distribution. The bin-by-bin correction method neglects the possibility of events migrating into adjacent bins after reconstruction which may lead to inaccurate unfolding. A method based on Bayes' theorem on probability has been developed to mitigate this effect. Some of its advantages are

- it is based on Bayes' theorem, a well grounded theory
- it may be applied to multidimensional problems
- the kinematic requirements on reconstructed and true distributions may be different
- it can correct for any type of smearing affecting reconstructed events.

B.2 Bayes' Theorem

To state Bayes' theorem, consider several independent *causes* C_i, where $i = 1, 2, ..., n_C$ which can produce a single *effect* E. Assuming that the initial probability $P(C_i)$ of causes and the conditional probability $P(E|C_i)$ of the cause C_i producing effect E are known, Bayes' theorem may be written as

$$P(C_i|E) = \frac{P(E|C_i)P(C_i)}{\sum_{l=1}^{n_C} P(E|C_l)P(C_l)}, \quad i = 1, 2, 3, ... \tag{B.3}$$

This equation states that if effect E is observed, then the probability $P(C_i|E)$ that the cause was C_i is proportional to the probability $P(C_i)$ of the cause multiplied by the probability $P(E|C_i)$ of the cause to produce that effect. Note that this equation depends on $P(E|C_i)$ which must be estimated or calculated using Monte Carlo methods.

As an example illustrating the use of Equation (B.3), consider an experiment in which virtual photons or Z bosons decaying into lepton-antilepton l^+l^- pairs are observed. Suppose effect E is the measurement of l^+l^- with reconstructed invariant mass m_{ll}^{reco} and the causes C_i are then all possible true invariant mass m_{ll}^{true} values the pair can have.

B.3 Unfolding

Bayes' theorem can be used in the unfolding process. Suppose $n(E)$ events with effect E are observed; then the estimator of the number of events of cause C_i is

$$\hat{n}(C_i) = n(E)P(C_i|E). \tag{B.4}$$

In the general case, there are many possible effects E_j, where $j = 1, 2, ..., n_E$ for a given cause C_i. For each of the n_E effects, Equation (B.3) holds, and so $P(C_i|E_j)$ may be evaluated. Typically, the conditional probabilities $P(C_i|E_j)$ are known as the *response matrix*. Denoting the initial probabilities of the causes by $P_0(C_i)$, Bayes' formula may now be generalized:

$$P(C_i|E_j) = \frac{P(E_j|C_i)P_0(C_i)}{\sum_{l=1}^{n_C} P(E_j|C_l)P_0(C_l)}, \quad i, j = 1, 2, 3, ... \tag{B.5}$$

Note that $0 \leq \sum_{j=1}^{n_E} P(E_j|C_i) \leq 1$. This property reveals that there is no reason for each cause to produce at least one of the possible effects. Let the efficiency of detecting cause C_i in any of the possible effects be denoted by $\epsilon_i \equiv \sum_{j=1}^{n_E} P(E_j|C_i)$.

Having made N_{obs} experimental observations, a distribution of the number of events for each outcome is obtained:

$$n(E) \equiv \{n(E_1), n(E_2), ..., n(E_{n_E})\}. \tag{B.6}$$

The expected number of events assigned to each cause that correspond to the observed

events can be calculated using Equation (B.4):

$$\hat{n}(C_i)|_{obs} = \sum_{j=1}^{n_E} n(E_j)P(C_i|E). \tag{B.7}$$

Correcting $\hat{n}(C_i)|_{obs}$ with the ϵ gives an estimate of the true number of events:

$$\hat{n}(C_i) = \frac{1}{\epsilon}\sum_{j=1}^{n_E} n(E_j)P(C_i|E), \quad \epsilon \neq 0. \tag{B.8}$$

Having the total number of unfolded events, the total number of true events is

$$\hat{N}_{true} = \sum_{i=1}^{n_C} \hat{n}(C_i), \tag{B.9}$$

and an estimate of the probability of the causes is

$$\hat{P}(C_i) \equiv P(C_i|n(E)) = \frac{\hat{n}(C_i)}{\hat{N}_{true}}. \tag{B.10}$$

The accuracy of Bayesian unfolding is dependent on the initial distribution $P_0(C)$. The accuracy of $\hat{P}(C_i)$ is dependent on the agreement between $P_0(C)$ and the true distribution $P^{true}(C)$ of data. By proceeding iteratively, the best possible results may be obtained. The following steps are performed:

1. choose $P_0(C)$ based on knowledge of the process under study
2. calculate the initial expected number of events based on $P_0(C)$: $n_0(C_i) = P_0(C_i)N_{obs}$
3. calculate $\hat{n}(C)$ and $\hat{P}(C)$ using Equations (B.8) and (B.10), respectively
4. make a χ^2 test comparing $n_0(C)$ and $\hat{n}(C)$
5. replace $P_0(C)$ with $\hat{P}(C)$ and $n_0(C_i)$ with $\hat{n}(C)$ and repeat the process
6. if after the second iteration the value of χ^2 is satisfactory, stop the process, otherwise return to step 3.

The final distribution $\hat{n}(C)$ after iterating should be the best estimate of the true distribution.

Bibliography

[1] The LHC Study Group. *Design Study of the Large Hadron Collider.* CERN-91-03, 1991.

[2] The ATLAS Collaboration. *ATLAS Detector and Physics Performance Technical Design Report Volumes I and II.* CERN-LHCC-99-14, 1999.

[3] E. Eichten et al. *Supercollider Physics.* Reviews of Modern Physics 56 No 4, 1984.

[4] T. M. Yang S. D. Drell. *Massive Lepton-Pair Production in Hadron-Hadron Colliders at High Energies.* Physical Review Letters, Volume 25 No 5, 1970.

[5] Tayfun Ince. *Prospects for probing the structure of the proton with low-mass Drell-Yan events in ATLAS.* University of Victoria, 2009.

[6] D. V. Schroeder M. E. Peskin. *An Introduction to Quantum Field Theory.* Westview Press, 1995.

[7] D. J. Griffiths. *Introduction to Elementary Particles.* John Wiley and Sons Inc., 1987.

[8] A. D. Martin et al. *Parton distributions for the LHC.* arXiv:0901.0002, 2009.

[9] F. Close. *The quark parton model.* Rep. Prog. Phys. 42 1285, 1979.

[10] R. J. N. Phillips V. D. Barger. *Collider Physics.* Westview Press, 1996.

[11] B. R. Webber R. K. Ellis, W. J. Stirling. *QCD and Collider Physics.* Cambridge University Press, 2003.

[12] P. Byrant L. Evans. *LHC Machine.* JINST 3 S08001, 2008.

[13] The ATLAS Collaboration. *The ATLAS Experiment at the CERN Large Hadron Collider*. JINST 3 S08003, 2008.

[14] The ATLAS Collaboration. *Improved luminosity determination in pp collisions at $\sqrt{s} = 7$ TeV using the ATLAS Detector at the LHC*. Eur. Phys. J. C. PHYS-2012-821, 2012.

[15] The ATLAS Collaboration. *Measurement of the inelastic proton-proton cross-section at $\sqrt{s} = 7$ TeV with the ATLAS detector*. arXiv:1104.0326, 2011.

[16] The ATLAS Collaboration. *ATLAS Inner Detector Technical Design Report*. CERN-LHCC-97-16, 1997.

[17] The ATLAS Collaboration. *ATLAS pixel detector: technical design report*. CERN-LHCC-98-013, 1998.

[18] The ATLAS Collaboration. *The barrel modules of the ATLAS semiconductor tracker*. Nucl. Instrum. Meth. A 568, 2006.

[19] The ATLAS Collaboration. *The ATLAS semiconductor tracker end-cap module*. Nucl. Instrum. Meth. A 575, 2007.

[20] The ATLAS Collaboration. *The ATLAS Transition Radiation Tracker (TRT) proportional drift tube: design and performance*. JINST 3 P02013, 2008.

[21] The ATLAS Collaboration. *ATLAS Liquid Argon Calorimeter Technical Design Report*. CERN-LHCC-96-41, 1996.

[22] The ATLAS Collaboration. *ATLAS Tile Calorimeter Technical Design Report*. CERN-LHCC-96-42, 1996.

[23] The ATLAS Collaboration. *ATLAS Muon Spectrometer Technical Design Report*. CERN-LHCC-97-22, 1997.

[24] E. Diehl et al. *ATLAS Muon Detector Commissioning*. arXiv:0910.2767, 2009.

[25] The ATLAS Collaboration. *ATLAS Level-1 Trigger Technical Design Report*. CERN-LHCC-98-014, 1998.

[26] The ATLAS Collaboration. *ATLAS High Level Trigger, Data Acquisition and Controls Technical Design Report*. CERN-LHCC-2003-022, 2003.

[27] I. M. Sobol. *A Primer for the Monte Carlo Method*. CRC Press, 1994.

[28] P. Skands T. Sjostrand, S. Mrenna. *PYTHIA 6.4 Physics and Manual*. ph/0603175v2, 2006.

[29] G. Corcella et al. *HERWIG 6.5: an event generator for Hadron Emission Reactions with Interfering Gluons*. ph/0011363v3, 2002.

[30] GEANT4 Collaboration. *GEANT4: a simulation toolkit*. Nuclear Instruments and Methods A, Volume 506, 2003.

[31] B. R. Webber S. Frixione. *Matching NLO QCD computations and parton shower simulations*. JHEP 0206 029, 2002.

[32] The ATLAS Collaboration. *Electron performance in the ATLAS experiment*. ATL-PHYS-INT-2010-126, 2009.

[33] ATLAS Drell-Yan Working Group. *Private communications*. 2012.

[34] G. D'Agostini. *A Multidimensional Unfolding Method Based on Bayes' Theorem*. Nucl. Inst. and Meth. in Phys. Sect. A 362, 1995.

[35] The ATLAS Collaboration. *Tag and Probe Method for Electron ID Efficiencies*. ATLAS Internal, 2009.

[36] The ATLAS Collaboration. *Electron performance measurements with the ATLAS detector using the 2010 LHC proton-proton collision data*. arXiv:1110.3174v1, 2012.

[37] T. Adye. *Unfolding Algorithms and Tests using RooUnfold*. arXiv:1105.1160v1, 2011.

[38] J. Pumplin et al. *Uncertainties of predictions from parton distribution functions II: the Hessian method*. hep-ph/0101032v3, 2001.

[39] J. Pumplin et al. *New generation of parton distributions with uncertainties from global QCD analysis*. arXiv:hep-ph/0201195, 2002.

[40] A. M. Cooper-Sarkar. *PDF fits at HERA*. arXiv:1112.2107, 2011.

[41] R. D. Ball et al. *A first unbiased global NLO determination of parton distributions and their uncertainties*. arXiv:1002.4407, 2010.

[42] The ATLAS Collaboration. *Luminosity determination in pp collisions at* $\sqrt{s} = 7$ *TeV using the ATLAS detector in 2011.* ATLAS-CONF-2011-116, 2011.